A Dissertation

entitled

Computer Aided Design of Microwave Front-End Components and Antennas for Ultrawideband Systems

by

Mohammad J. Almalkawi

Submitted to the Graduate Faculty as partial fulfillment of the requirements for the Doctor of Philosophy Degree in Engineering

Vijay Devabhaktuni, Ph.D., Committee Chair

Junghwan Kim, Ph.D., Committee Member

Roger King, Ph.D., Committee Member

Ashok Kumar, Ph.D., Committee Member

Lingfeng Wang, Ph.D., Committee Member

Lei Zhang, Ph.D., Committee Member

Dr. Patricia R. Komuniecki,
Dean College of Graduate Studies

The University of Toledo

December 2011

An Abstract of

Computer Aided Design of Microwave Front-End Components and Antennas for Ultrawideband Systems

by

Mohammad J. Almalkawi

Submitted to the Graduate Faculty as partial fulfillment of the requirements for the Doctor of Philosophy Degree in Engineering

The University of Toledo
December 2011

This dissertation contributes to the development of novel designs, and implementation techniques for microwave front-end components and packaging employing both transmission line theory and classical circuit theory. For compact realization, all the presented components have been implemented using planar microstrip technology.

Recently, there has been an increase in the demand for compact microwave front-ends which exhibit advanced functions. Under this trend, the development of multiband front-end components such as antennas with multiple band-notches, dual-band microwave filters, and high-Q reconfigurable filters play a pivotal role for more convenient and compact products. Therefore, the content of this dissertation is composed of three parts. The first part focuses on packaging as an essential process in RF/microwave integration that is used to mitigate unwanted radiations or crosstalk due to the connection traces. In printed circuit board (PCB) interconnects, crosstalk reduction has been achieved by adding a guard trace with/without vias or stitching capacitors that control the coupling between the traces. In this research, a new signal trace configuration to reduce crosstalk without adding additional components or guard traces is introduced.

The second part of this dissertation considers the inherent challenges in the design of multiple-band notched ultrawideband antennas that include the integration of multilayer antennas with RF front-ends and the realization of compact size antennas. In this work, a compact UWB antenna with quad band-notched frequency characteristics was designed, fabricated, and tested demonstrating the desired performance. The third part discusses the design of single- and dual-band dual-mode filters exhibiting both symmetric and asymmetric transfer characteristics. In dual-mode filters, the numbers of resonators that determine the order of a filter are reduced by half while maintaining the performance of the actual filter order. Here, in order to maintain high performance of conventional rectangular waveguides in planar form, substrate integrated waveguide (SIW) technology was utilized. A design of single-band dual-mode SIW filters with improved upper stopband performance and a design of dual-band dual mode SIW filters are introduced. Compact evanescent-mode SIW filters are also realized for low frequency applications and for better stopband performance. In addition, a novel tuning solution for planar SIW reconfigurable filters is also presented. Tunablity of the reconfigurable filter is achieved by adjusting dc-magnetic bias applied to the ferrite material. The new tuning technique leads to a dramatic reduction in complexity for the external control system.

For my parents, my brothers, and my wife Reema

Acknowledgments

I would like to express my deepest gratitude to my advisor Dr. Vijay Devabhaktuni for his support and guidance in so many ways throughout the development of this doctoral dissertation. He has been an advisor and a friend. I am thankful for his insightful coaching and his tremendous encouragement.

It has been a great pleasure working with the faculty, staff, and my lab mates at the University of Toledo, during my journey through the Ph.D. program. I gratefully thank Dr. Roger King, Dr. Junghwan Kim, Dr. Lingfeng Wang, Dr. Ashok Kumar, and Dr. Lei Zhang for serving on my Ph.D. committee.

I would also like to thank my friend and former colleague Ahmad Gheethan from the University of South Florida for the valuable discussions about antenna theory.

I appreciate the funding supports offered by the Electrical Engineering and Computer Science (EECS) department in giving me the opportunity to pursue my doctoral research.

Finally, I would like to thank my parents and my brothers for their endless encouragement and support throughout the whole education stages.

Table of Contents

List of Tables

List of Figures

List of Abbreviations

CW……Coplanar Waveguide

DGS……...Defected Ground Structure

EBG……...Electromagnetic Band-Gap
EM……..…Electromagnetic
EMC……..Electromagnetic Compatibility

FCC……...Federal Communications Commission
FDTD……....Finite Difference Time Domain
FEM……..Finite Element Method

GA…….....Genetic Algorithm

HFSS…….....High Frequency Structure Simulator
HTS…….…..High Temperature Superconductive

INSAT……...Indian National Satellite

LPF…….....Low-Pass Filter
LTCC…….....Low Temperature Co-Fired Ceramic

MEMS……...Micro-Electromechanical Systems
MMIC……...Monolithic Microwave Integrated Circuit
MOM……....Method of Moment

NF…….....Noise Figure
Ni……..…Nickel

PCB……..….Printed Circuit Board

RF……..…Radio Frequency

SI……...Signal Integrity
SIW……..….Substrate Integrated Waveguide
SMA……..…SubMiniature Version A

TE……..Transverse Electric
TEM……..…Transverse ElectroMagnetic
TL…….....Transmission Line
TM…….……Transverse Magnetic
TZ…….…….Transmission Zero

UWB…….……Ultrawideband

VLSI…….Very-Large-Scale Integration
VNA……..……Vector Network Analyzer
VSWR……..…….Voltage Standing Wave Ratio

WiMAX……...….Worldwide Interoperability for Microwave Access
WLAN…….....Wireless Local Area Network

Chapter 1

Introduction

The advance functionality of modern communication systems (*e.g.* airborne, satellite, and handheld personal systems) increasingly demands higher performance of compact size, low weight, and high reliability microwave front-ends. In order to address these challenges, RF/microwave components have been realized using planar technologies and diverse implementation techniques of microwave front-ends continue to be a subject of research interest.

In this chapter, Section 1.1 and Section 1.2 discuss the motivation and objectives behind the study of microwave front-end components and antennas with their applications in Ultrawideband (UWB) systems followed with a brief overview of each chapter in this dissertation as described in Section 1.3.

1.1 Motivation

Microwave radio frequencies (RF) are electromagnetic (EM) waves that have a frequency range from around 0.3 GHz to 300 GHz with corresponding wavelength range from 1m to 1mm. Microwave signals travel by line-of-sight and are not bent by the Earth's ionosphere unlike lower frequency signals. As well, microwave signals obey the

laws of optics and can be transmitted, absorbed, or reflected depending on the transferring media types.

In the late 1970s, lumped element components started to find a place in the microwave frequency range [1]. Recently, lumped element components have demonstrated the capability to operate up to 18 GHz [1]; however, the low unloaded quality factor (Q_0) realized by lumped element components results in poor insertion loss performance as the frequency increases.

For this reason, distributed microwave theory was developed as an extension to lumped element theory. Figure 1-1 illustrates the three available theories for solving any electrical problem based on its frequency of operation. Lumped element theory is a simplified circuit model used to solve low frequency problems where the effective size of a device is very small compared to the wavelength; distributed element theory is a simplified circuit model for high frequency problems where the maximum dimension of a device is comparable with the wavelength; while Maxwell's theory is a full-wave solution based on Maxwell's equations and is suitable for all electrical problems. Different numerical techniques based on Maxwell's equation have been developed such as the Finite Difference Time-Domain (FDTD) method, the Finite Element Method (FEM), and the Method of moments (MOM). Depending on the problem under analysis, each of those techniques has its own strength in terms of accuracy, computation time, and boundary definitions when dealing with the radiated emissions.

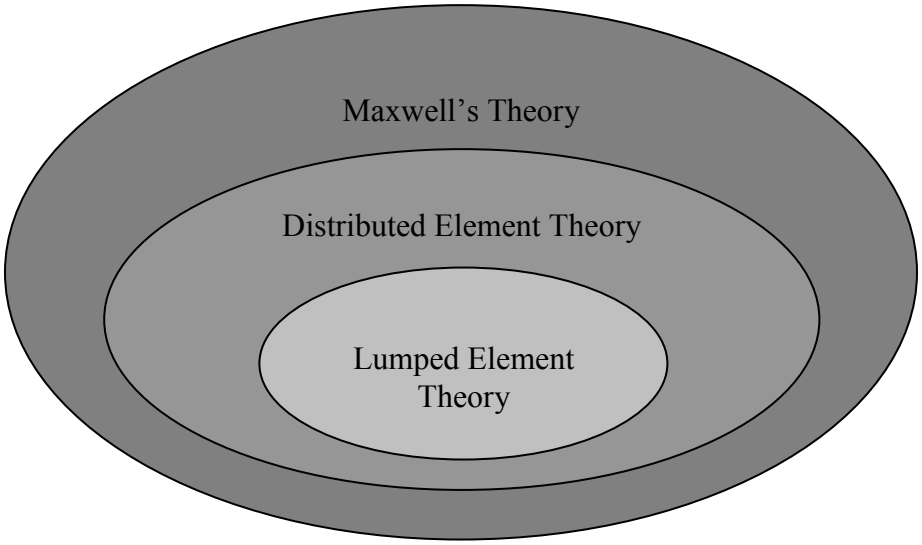

Figure 1-1: Different circuit-theories based on the frequency of operation.

Through this dissertation, distributed element concepts are applied in designing the proposed front-ends and confirmed using full-wave EM simulations.

Distributed elements are a solution to the low Q-factor encountered by the lumped elements; however, planar distributed elements are often built using Microstrip or Stripline technologies (see Figure 1-2 and Figure 1-3, respectively) that make the physical dimensions large in comparison to the lumped elements. Both Microstrip and Stripline are planar technologies which can be fabricated using photolithography techniques. However, Microstrips are preferred because they are lighter, more compact, and easier to fabricate. Stripline supports a pure transverse ElectroMagnetic (TEM) mode which allows better noise immunity. Microstrip supports a quasi-TEM mode or a hybrid mode that is due to the inhomogeneous medium surrounding the transmission line (*i.e.* dielectric material below and air above the transmission line).

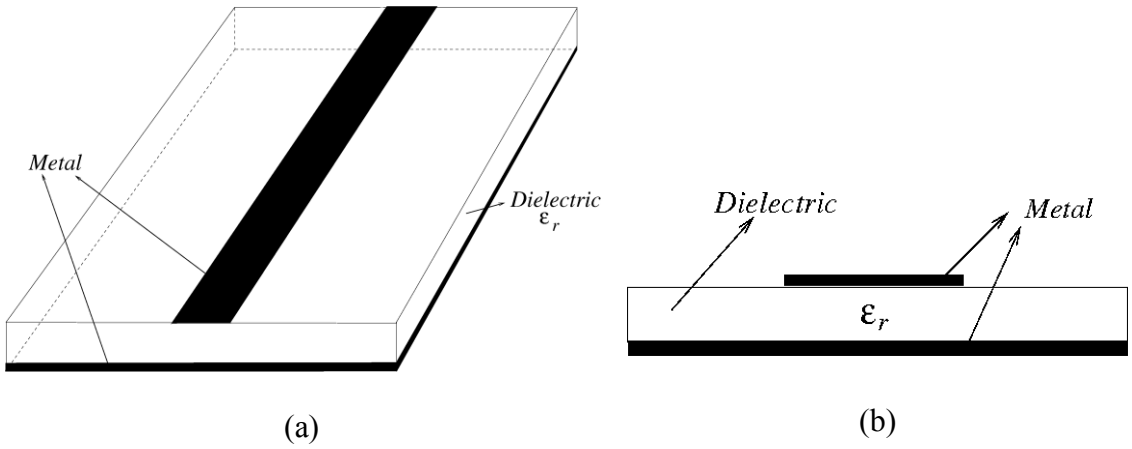

Figure 1-2: Microstrip transmission line: (a) 3D view; (b) 2D side view.

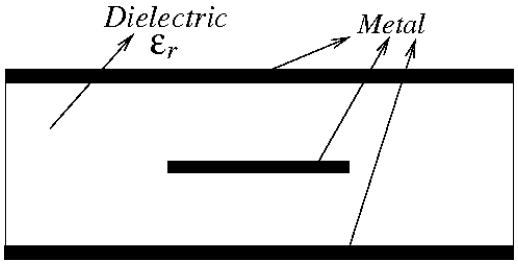

Figure 1-3: Stripline cross-section.

The diversity of applications and operational environments has led to high production volumes of microwave front-ends including but not limited to:

i. Packaging,

ii. Antennas, and

iii. Microwave filters.

Each of these components is capable of degrading the performance of a system and needs individual attention while designing the system. The following three subsections will describe the challenges inherent to each component.

1.1.1 Packaging

Packaging is an essential process in RF/microwave integration that is used to achieve reliable operation in environment with extreme risk of interference. In microwave circuits with complex multilayer and highly dense interconnect layouts, crosstalk is a well-known electromagnetic compatibility (EMC) and Signal integrity (SI) problem. Usually, SI deals with noise levels in micro-Volts (μV) and micro-Amperes (μA), while EMC deals with milli-Volts (mV) and milli-Amperes (mA) noise levels.

The advanced functionality of modern systems has imposed stringent EMC requirements on front-end components, such as allowing minimum quantified levels of radiated emissions. Therefore, it is always required to mitigate crosstalk caused by the connection traces in a circuit. For example, reconfigurable devices require biasing traces which generate undesirable electromagnetic interference or crosstalk. In literature, crosstalk reduction has been achieved by adding guard traces with/without vias that control the coupling between these traces. For compact realization, it is desirable to reduce the crosstalk without adding additional components or guard traces.

1.1.2 Antennas

In recent years, there has been a dramatic increase in demand for compact multiband front-ends which exhibit advanced transfer functions. For example, antennas with multiple band-notches are highly desired.

Over the past decade, UWB radio has been considered as a potential revolution in wireless communications that enables transmitting and receiving over a wide spectrum.

UWB systems enable energy transmission over a wide range of frequencies such that a very low power spectrum can be successfully received in coexistence with narrowband systems. In communications receivers, the antenna is an important component which transforms unguided EM energy to guided signals which can be manipulated at different stages (*e.g.* microwave filters) of the receiver. Microwave filters are used to separate communication channels operating at different frequencies thus eliminating interference between the channels. However, to reduce the number of filters in an UWB system, it is usually preferred to exploit the existing space of the antenna structure by enabling an antenna to operate as an energy receiver and a bandstop filter for specific unwanted bands. For best utilization of an antenna space, a multilayered antenna configuration is a good candidate. Here, challenges inherent with the design of multiple band-notched UWB antennas are comprised of the integration of multilayer antennas with RF front-ends and the realization of compact size antennas. Usually, it is difficult to generate multiple band-notches within the antenna radiator layer using parasitic elements while maintaining a monopole like radiation pattern. A monopole radiation pattern is essential for UWB applications and specifically in portable devices (*e.g.* Laptops, personal computers (PCs), and personal connectivity devices).

1.1.3 Microwave Filters

Other important components are the microwave filters. Microwave filters are the key building block in any modern communication systems. Generally, the success in the design procedure of a filter is based on the similarity between the equivalent circuit model and the physical structure. High-Q bandpass and bandstop applications using

planar technologies dominate the filter field. Here, in order to maintain high-Q and low loss of conventional rectangular waveguides in planar form, substrate integrated waveguide (SIW) filters are utilized. Figure 1-4(a) shows the conventional rectangular waveguide cavity while Figure 1-4(b) shows its transformation into an SIW cavity. This is done by replacing the perfect side walls of a waveguide cavity into metallic vias and by reducing the waveguide cavity height to match the planar substrate height.

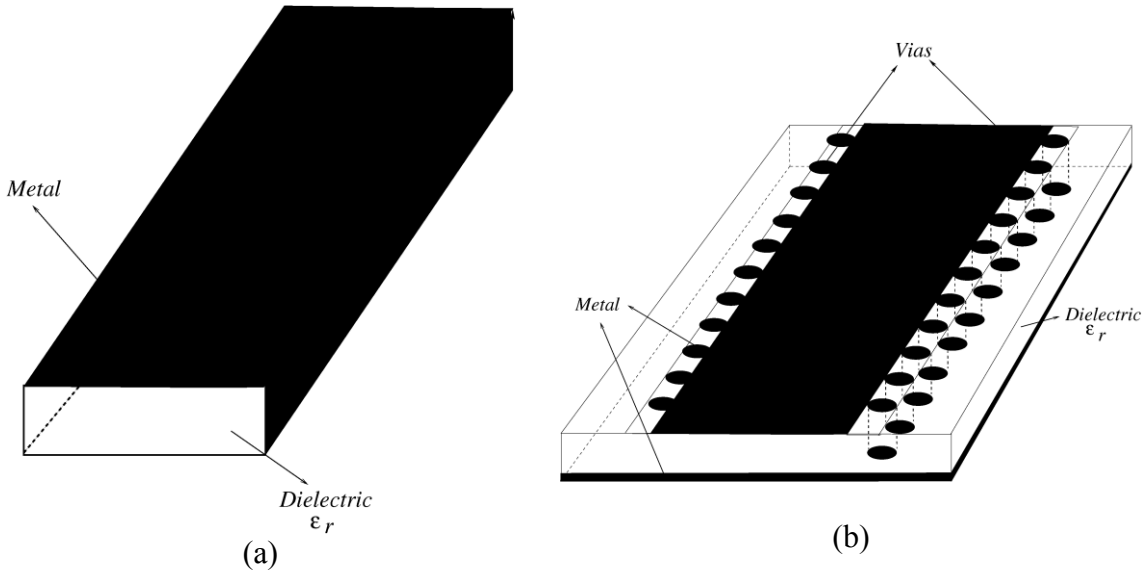

Figure 1-4: (a) 3D rectangular H-plane waveguide cavity; (b) SIW cavity.

However, SIW filters suffer from a limited upper stopband performance. Therefore, an SIW filter needs to be cascaded by a low-pass cleanup filter in order to be successfully integrated within a system. From this perspective and for compact realization, dual-mode and evanescent-mode SIW filters exhibiting both symmetric and asymmetric transfer characteristics are introduced. The design of asymmetrical filters [2, 3] requires the placement of finite-frequency transmission zeros (TZs) either in the lower or the upper

stopband. A finite-frequency TZ is known as the placement of a highly sharp attenuation through the transmission coefficient (S_{21}) of a filter at a specific frequency usually beside its passband edges. Thus, the importance of placing a TZ is that a filter will be more selective on one side of the passband than the other or in both sides if there are two or more TZs placed on the lower and upper stopband sides as in filters with symmetric transfer characteristics.

Moreover, planar reconfigurable filters are required in many multiband wireless communications and wideband radar systems. In response to this need, many tuning technologies have been proposed such as micro-electromechanical systems (MEMS) and mechanical tuning with electrically controlled methods. However, there is always need for new tuning technique which leads to a dramatic reduction in the complexity of the external control system (*e.g.* biasing circuits).

In order to integrate different RF/microwave components within a system, different parameters need to be considered and evaluated. The overall performance of a system can be evaluated by determining two important parameters for each component in the system. Those evaluation parameters are power gain (*GT*) and noise figure (*NF*). Figure 1-5 shows a two-port network system formed by cascading series N components.

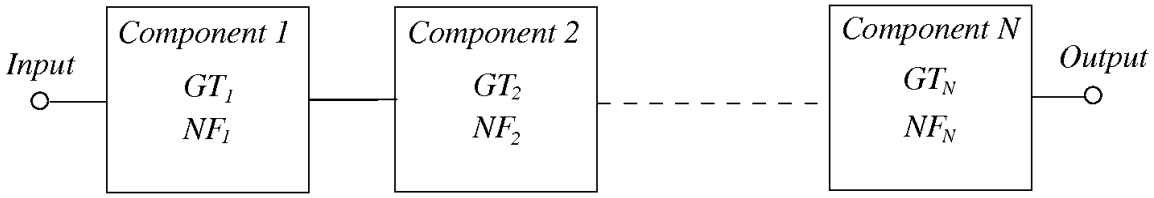

Figure 1-5: System integration by cascading N components.

The power gain is defined as the ratio of power delivered to the load to that available from the source or in other words, power gain is the magnitude of the forward scattering parameter $|S_{21}|^2$. The total power gain (GT_{Total}) of a system is calculated using the following equation

$$GT_{Total} = GT_1(dB) + GT_2(dB) + ... + GT_N(dB) \tag{1.1}$$

where GT_1, GT_2,…, GT_N are the power gain for the individual components in a system in dB.

Precisely, the term power gain is associated with active RF components which need an external power source to operate, while in passive components the term insertion loss is commonly used.

Noise figure is defined as the ratio of the signal to noise ratio (*S/N*) at the input side to the signal to noise ratio at the output side as in (1.2).

$$NF(dB) = \frac{(S/N)_{Input}}{(S/N)_{Output}} \tag{1.2}$$

For a system of N components the total noise figure is given by

$$NF_{Total} = NF_1 + \frac{NF_2 - 1}{GT_1} + \frac{NF_3 - 1}{GT_1 \times GT_2} + ... + \frac{NF_N - 1}{GT_1 \times GT_2 ... GT_N} \tag{1.3}$$

1.2 Dissertation Objectives

As discussed in the previous section, performance of any system can be improved by efficiently designing its individual key components. The goal of this dissertation was to design novel and compact front-end components, namely, packaging, antennas, and

microwave filters, in order to achieve excellent performance of UWB systems. Such components with their advanced frequency characteristics are the key enabling technology for cognitive radios, and portable communications systems. Furthermore, the proposed components greatly increase system performance in terms of improved receiver sensitivity, rejection of high-power interferers, and simplified analog front-end architecture.

1.3 Dissertation Overview

The dissertation is organized as follows: Chapter 2 presents new trace configuration employing stepped impedance elements and open-circuited stubs to reduce far-end crosstalk in printed circuit board (PCB) interconnects. The goal of this research is to reduce crosstalk without using additional PCB components in the design. Specifically, stepped impedance elements and open-circuited stubs of uniform length and width on the victim traces are employed to suppress high-frequency electromagnetic interference and to equalize propagation delays (*i.e.* capacitive and inductive couplings between PCB traces). The overall design is very similar to the usual low-pass filter configurations which are difficult to implement in the prototype testing. The proposed approach shows remarkably better results when compared to conventional intervening guard trace schemes.

Chapter 3 proposes a new and simple design of a multilayered quad band-notched UWB antenna. The antenna is compact in size, suitable for UWB applications, and exhibits quad narrow band frequency notches to suppress the interference of the nearby wireless communication systems within an UWB frequency range. The narrow band

notches are realized by adding closed-loop ring resonators designed to cover the 3.3-3.7 GHz, 4.5-4.8 GHz, 5.15-5.35 GHz, and 5.725-5.825 GHz bands. The antenna is fabricated and tested for demonstrating the desired characteristic.

The following three chapters (Chapter 4, 5, and 6) are dedicated to the design of microwave filters which are essential components in UWB systems in specific and transceiver systems in general. Chapter 4 discusses the design of dual-mode SIW filters with improved upper stopband attenuation. The filter is comprised of a TE_{102} and TE_{201} modes waveguide resonator. A simple solution for improving the upper stopband performance while maintaining compact size realization is provided. The stopband improvement is achieved by using defected ground structure (DGS) which is etched on the ground plane of the SIW cavity. Compared to previous reported SIW filters with improved stopband achieved by lowpass cleanup filters, the proposed approach provides a relatively compact realization while reducing the complexity of the overall structure. In addition, the design of dual-band dual-mode SIW filters with symmetric transmission zeros is discussed.

Chapter 5 introduces a novel tuning solution for planar reconfigurable microwave filters. The design is based on the application of a classical synthesis technique of waveguide ferrite circulators and isolators. Tunablity is achieved by adjusting dc-magnetic bias applied to the ferrite material. Compared to the previously reported reconfigurable filters based on electrical adjustment enabled by mechanical modifications, the designed filters offer a relatively wide tuning range and stable tunability, while dramatically reducing the complexity of the external control system.

Chapter 6 presents a compact realization of an evanescent-mode SIW bandpass filter. A 3rd order filter comprised of three Comblines spread throughout an SIW section is implemented. The filter is capable of realizing N-1 transmission zeros where N is the filter's order and has relatively better upper stopband attenuation.

In this dissertation, planar Microstrip and SIW technologies were used for realizing all the implemented structures. Copper metals were selected since they are inexpensive, easily machinable, and have good conductivity. As well, a commercial EM solver named ANSYS High Frequency Structure Simulator (HFSS) based on the FEM method was used to provide the optimal dimensions of the proposed structures.

Chapter 2

Far-End Crosstalk Reduction in PCB Interconnects

Crosstalk in PCB traces is a well-known EMC and SI problem. A typical scenario involves coupling of a high-frequency signal (*e.g.* a digital clock) onto a low-frequency trace (*e.g.* a power or a ground trace). Since low-frequency traces are typically long traces routed on multiple layers on a PCB, high-frequency interference may easily radiate from multiple and/or unsuspected locations on the PCB. Therefore, it is usually very difficult to determine the actual location of the radiating area on the board.

Normally, the first line of defence is to mitigate the radiation source by reducing the current strength, slewing the rise/fall time of the digital signal (*e.g.* by adding series resistors or ferrites [4]) or shortening/straightening the high-frequency trace. Though such countermeasures may provide a limited improvement, they may not even be an option for a given design (*e.g.* for SI constraints). SI in PCBs refers to ensuring that a signal when sent down through a pair of traces will arrive at the receiver side with the desired level, timing, and wave-shape.

Another way to reduce crosstalk is to exploit the inherent parasitic effects (*i.e.* mutual capacitance and mutual inductance) among PCB traces [5-8]. Usually increasing the capacitive coupling along coupled surface Microstrip traces may be used to reduce

far-end crosstalk [6].

To this end, different configurations of guard traces have been employed in between adjacent interconnects [5, 9-11]. In addition, grounded vias can be added to the guard trace to help further reduce crosstalk. However, large numbers of vias degrade the SI and routing additional traces may not be possible in a crowded layout. Furthermore, crosstalk reduction provided by guard traces is limited and is usually insufficient [5, 12-14]. Therefore, it is highly desirable to explore new trace configurations that may provide better crosstalk reduction and can be routed in a crowded layout.

One way is to employ a low-pass filter (LPF) configuration on the victim traces. A typical LPF employs either stepped impedance elements or open-circuited stubs on the victim trace. This method achieves much better performance than designs using guard traces alone. However, since stepped impedance elements and open-circuited stubs have non-uniform lengths and widths, it is very difficult to implement different LPF configurations on PCB traces in a prototype testing.

This chapter introduces novel victim trace configurations to reduce far-end crosstalk coupling between two adjacent PCB traces. The far-end crosstalk is of particular interest due to the significantly stronger coupling as compared to that at the near-end [15]. The proposed configurations have LPF characteristics [16] as they employ stepped impedance elements and open-circuited stubs. However, these elements have uniform lengths and, therefore, are easier to implement in the prototype testing in EMC pre-compliance/compliance chambers.

The organization of this chapter is as follows. Section 2.1 discusses both conventional and proposed crosstalk reduction configurations. Section 2.2 compares

these PCB configurations in terms of crosstalk reduction in adjacent PCB traces, while conclusions are given in Section 2.3.

2.1 Crosstalk Reduction Schemes

Figure 2-1 illustrates a PCB structure (50 mm x 40 mm) with two adjacent uniform traces that are spaced 8 mm apart. Both traces are 3 mm wide and 50 mm long. As illustrated, the PCB structure is supported by a 1.575 mm thick FR4 substrate with a dielectric constant of 4.4 and a loss tangent of 0.02. It was assumed that one trace (acting as an aggressor) is carrying digital or high-frequency signals. These signals may couple onto the adjacent trace (hereby referred as the victim trace) which is carrying low-frequency or DC currents.

To reduce this coupling, referred to as crosstalk, various configurations can be employed. The following subsections discuss conventional configurations (Section 2.1.1) as well as the proposed configurations (Section 2.1.2.2 and Section 2.1.3.2).

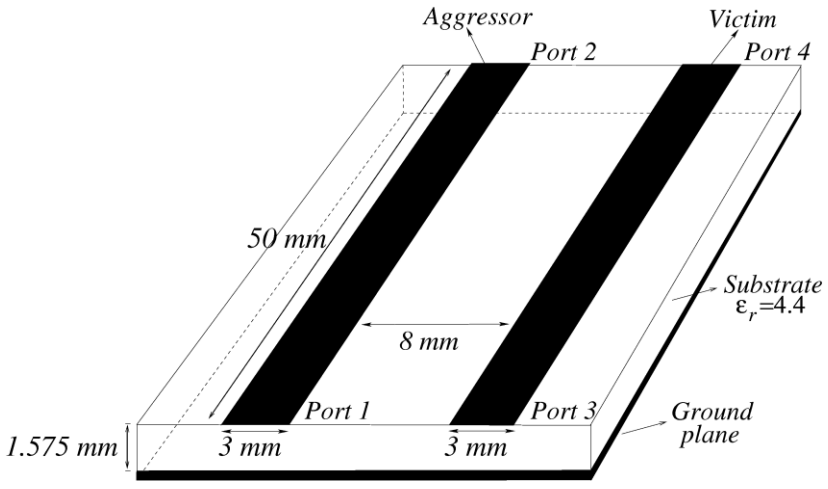

Figure 2-1: PCB structure with two uniform adjacent traces.

2.1.1 Conventional Configurations

As illustrated in Figure 2-2, a guard trace is usually introduced (as a shield) in between the aggressor and the victim trace. For additional shielding, one may also ground the guard trace with via fences (see Figure 2-3).

Here, the guard trace is assumed to be 1 mm wide and is terminated at both ends by the matched impedance (*i.e.* 87 Ω) to prevent any standing waves. Furthermore, the spacing between each via on the guard trace is assumed to be 2 mm.

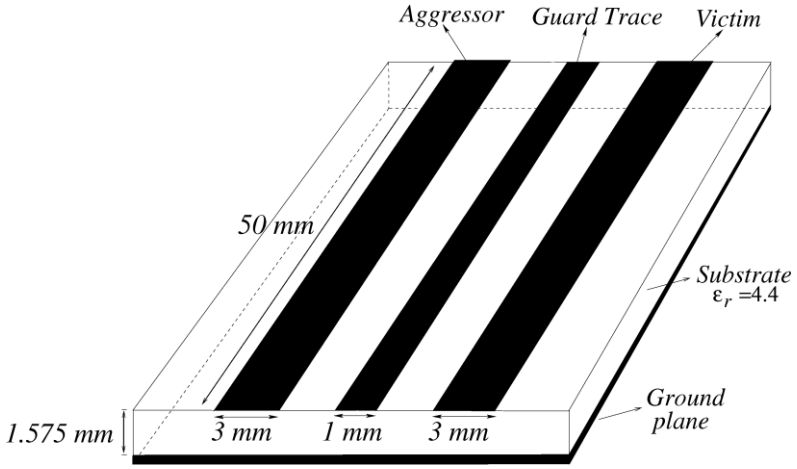

Figure 2-2: PCB structure with a guard trace between two uniform adjacent traces.

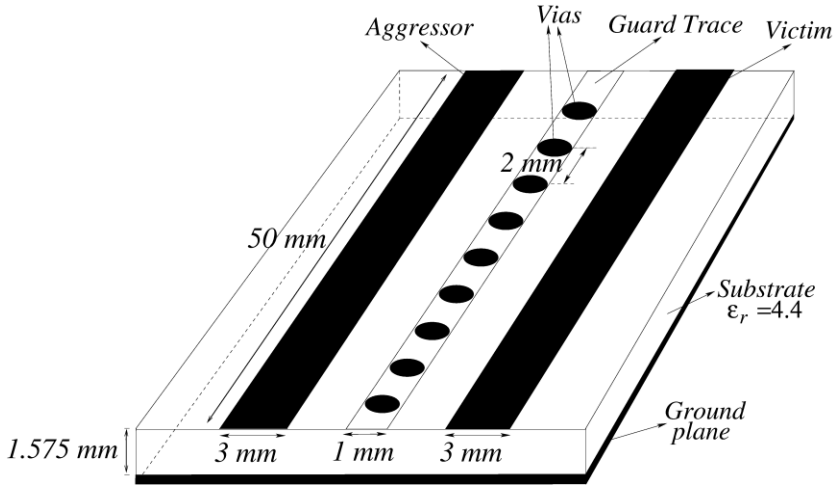

Figure 2-3: PCB structure with a guard trace grounded with vias between two uniform adjacent traces.

2.1.2 Stepped Impedance LPF Configuration

2.1.2.1 Stepped Impedance LPF Design

In [17], the stepped impedance trace for crosstalk reduction was presented. Here, if the victim trace is a low-frequency or DC trace, one may employ a stepped impedance LPF configuration (*i.e.* using elements of alternating high and low impedance on the trace). Length l_{Hi} of the high impedance (Z_H) element can be calculated using the electrical length defined as [16],

$$\beta l_{Hi} = \frac{LR_0}{Z_H}, \tag{2.1}$$

where $\beta = 2\pi/\lambda$, λ corresponds to the cut-off frequency of the LPF, and R_0 represents the feed trace characteristic impedance. Similarly, length l_{Li} of the low impedance element (Z_L) can be calculated as,

$$\beta l_{Li} = \frac{CZ_L}{R_0}, \tag{2.2}$$

where L and C are the normalized lumped element values for the inductors and capacitors respectively [18]. The width of the elements is chosen corresponding to impedances Z_H and Z_L. Here, Z_H and Z_L are usually set to the highest and lowest characteristic impedance values that can be practically fabricated. It is worth mentioning that the difference between the two impedances should be as high as possible for excellent filter performance (*i.e.* sharp cut-off). However, in this case, sharp cutoff is not an essential requirement. Figure 2-4 illustrates an example of a 5 elements LPF design. Here, Z_H = 120 Ω, Z_L = 20 Ω, and R_0 = 50 Ω were chosen. Also, a cut-off frequency of

4 GHz and a 7 dB insertion loss at 4.4 GHz were selected. The calculated values using (2.1) and (2.2) are given in Table 2.1.

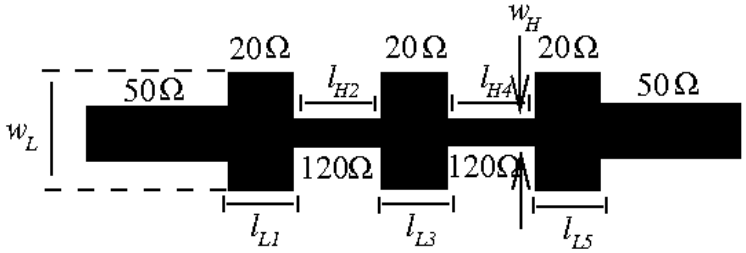

Figure 2-4: 5 elements stepped impedance LPF design.

Table 2.1: 5 Elements Stepped Impedance LPF Design.

Element Value	Impedance (Ω)	Electrical Length	Length (mm)	Width (mm)
C_1=0.618	Z_L=20	14.163^0	l_{L1}=1.492	w_L=11
L_2=1.618	Z_H=120	38.626^0	l_{H2}=4.657	w_H=0.4
C_3=2.000	Z_L=20	45.836^0	l_{L3}=4.828	w_L=11
L_4=1.618	Z_H=120	38.626^0	l_{H4}=4.657	w_H=0.4
C_5=0.618	Z_L=20	14.163^0	l_{L5}=1.492	w_L=11

2.1.2.2 Proposed Stepped Impedance Configuration

The proposed stepped impedance configuration (Figure 2-5) is based on the LPF design. However, unlike the LPF, the proposed structure employs uniform lengths (l_i) for all elements. This length may be selected to lie within the minimum and the maximum values calculated for the LPF design. For example, for the 5 elements design given in Table 2.1, the length for an element in the proposed configuration should be selected to be between 1.492 mm and 4.828 mm. Choosing a particular uniform length for all elements will affect the cut-off frequency and the return loss of the filter. Return loss and insertion loss of a filter are respectively given by

$$RL\ (dB) = -20\log_{10}|\Gamma| = -20\log_{10}|S_{11}| \tag{2.3}$$

and

$$IL\ (dB) = -20\log_{10}|S_{21}| \tag{2.4}$$

where $|\Gamma| = |S_{11}|$ is the S-parameter reflection coefficient, which is the ratio of the reflected wave to the incident wave, and S_{21} is the S-parameter transmission coefficient. However, since a low-frequency or DC signal on the victim trace is assumed, cut-off frequency and return loss are not the primary concerns. Fixing the element lengths simplifies the LPF design procedure and makes it easier to implement the design in EMC prototype testing (*e.g.* using copper tape). Furthermore, selecting a particular number of elements is arbitrary and affects the performance of the proposed configuration in terms of crosstalk. In this investigation, 3 elements and 5 elements configurations have been selected for comparison with the uniform trace configuration (Figure 2-1).

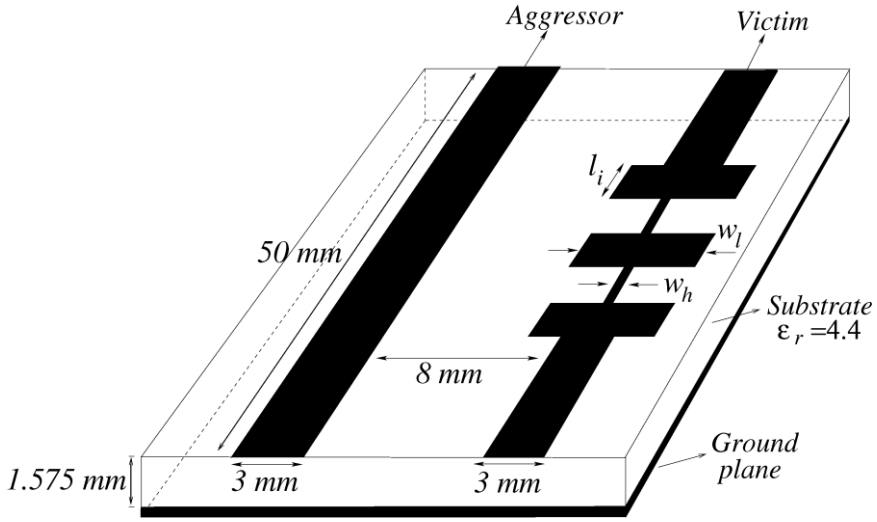

Figure 2-5: PCB structure of the proposed stepped impedance configuration with 5 elements.

2.1.3 Open-Circuited Stub LPF Configuration

2.1.3.1 Open-Circuited Stub LPF Design

One drawback of using the stepped impedance design is the narrow width of the high impedance sections. This could be an issue for the flow of high current densities. Therefore, a new trace configuration is introduced. Here, one may employ an open-circuited stub LPF on the victim trace. In this configuration, unity filter impedance is assumed and the element lengths are essentially equal to $\lambda/8$ at the cut-off frequency. This is by assuming unity cut-off frequency as in equation (2.7).

The widths for both stubs and transmission line (TL) sections correspond to their characteristic impedance values. Figure 2-6 depicts a 5 elements LPF circuit prototype. Here, by using Richard's transformation [16] to convert lumped elements to distributed elements, the reactance of an inductor can be calculated as

$$jX_L = jL\tan(\beta l) \tag{2.5}$$

and the susceptance of a capacitor can be calculated as

$$jB_C = jC\tan(\beta l) \tag{2.6}$$

where L and C are the normalized lumped element values, $\beta = 2\pi/\lambda$, λ corresponds to the cut-off frequency of the LPF, and X_L, B_C are the reactance and the susceptance of the lumped element components.

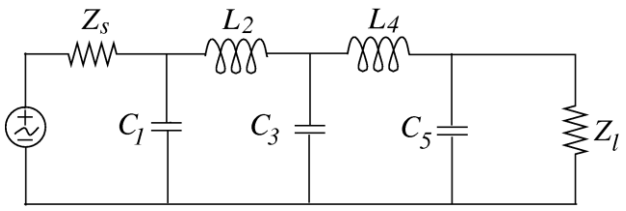

Figure 2-6: Circuit prototype of 5 elements open-circuited stub LPF.

These equations indicate that an inductor can be replaced with a short-circuited stub of length βl and characteristic impedance L, while a capacitor can be replaced with an open-circuited stub of length βl and characteristic impedance $1/C$ (see Figure 2-7).

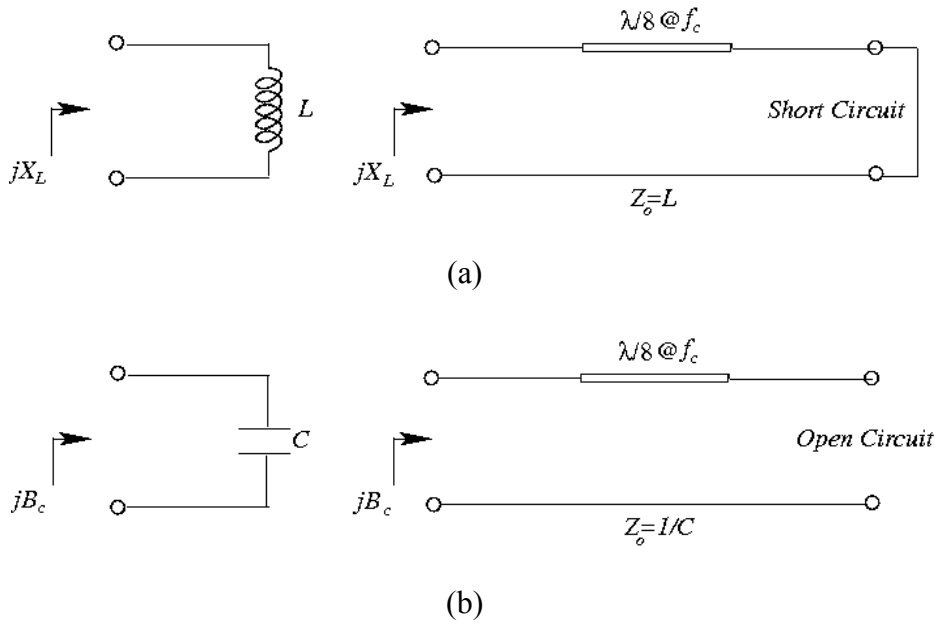

Figure 2-7: Richard's transformation for: (a) an inductor; (b) a capacitor.

Thus, the circuit prototype in Figure 2-6 after using Richard transformation to convert inductors and capacitors to series and shunt stubs is illustrated in Figure 2-8.

Equation (2.7) maps the ω plane to the Ω plane to realize a two-port LC network using open or short circuited stubs.

$$\Omega = \tan(\beta l) = \tan(\frac{\omega l}{v_p}) = 1 \tag{2.7}$$

where $\beta = \omega / v_p$, v_p is the phase velocity and l is the stub length.

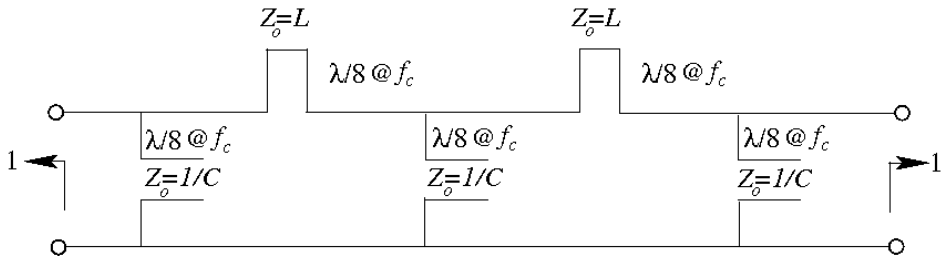

Figure 2-8: A normalized distributed circuit model of a 5 elements LPF design after using Richard's transformation.

Moreover, Kuroda's identities [16] are used to separate filter elements using transmission line sections and also to transform short-circuited stubs into open-circuited stubs. In PCB technology, open-circuited stubs are easier to fabricate than short-circuited stubs because a via hole through the substrate is not needed.

The following Kuroda's identities (see Figure 2-9) are used to convert all series stubs to shunt stubs and to convert the resulting short-circuited stubs into open-circuited stubs. Here, $n^2 = 1 + Z_2 / Z_1$.

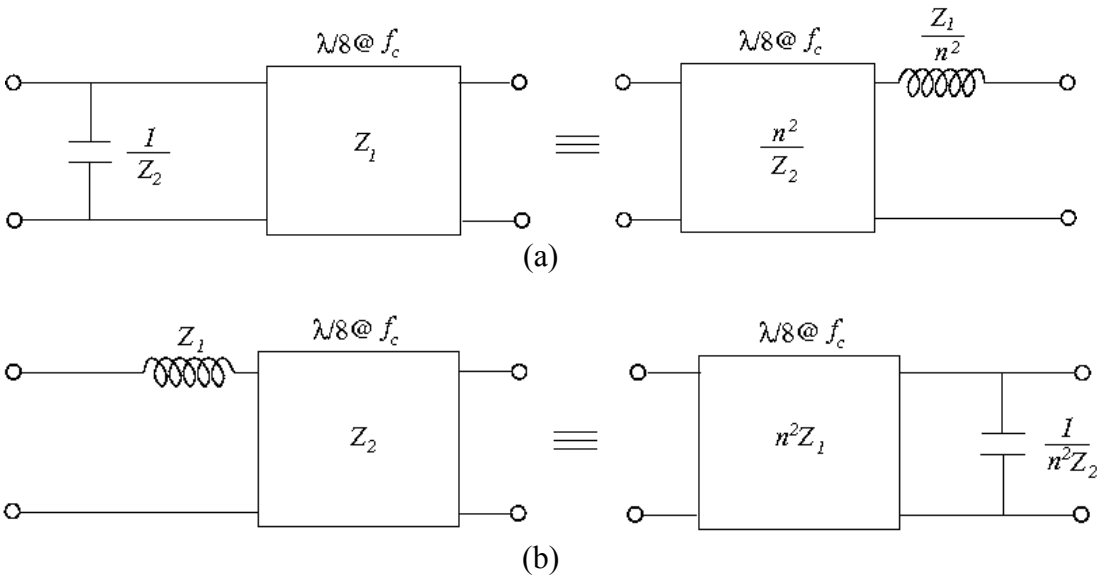

Figure 2-9: (a) Kuroda's 1st identity and (b) Kuroda's 2nd identity.

To make the filter realizable, and to match the source and load sides, additional transmission line sections called unit elements with $\lambda/8$ length at f_c were added as depicted in the following Figure 2-10. The introduction of unit elements does not affect the filter performances since they are matched to source and load impedances.

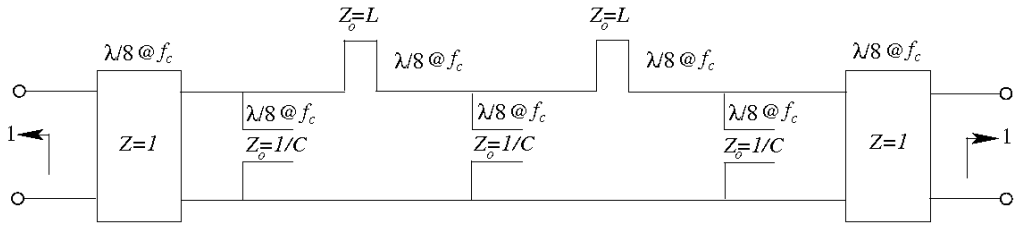

Figure 2-10: A normalized distributed circuit model of a 5 elements LPF design with unit elements at the ports side.

Figure 2-11 shows the circuit prototype after applying Kuroda's 1st identity to the first and last shunt stubs of Figure 2-10.

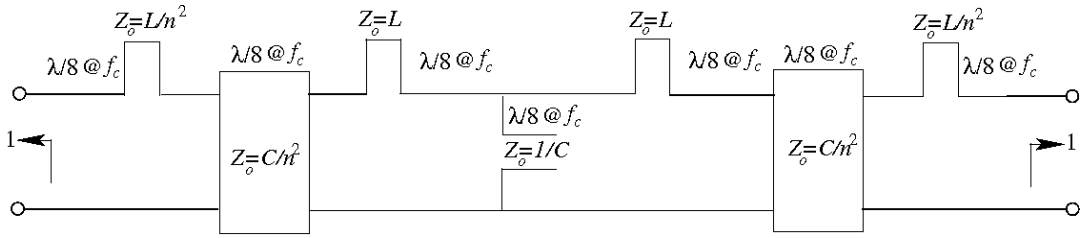

Figure 2-11: A normalized distributed circuit after applying Kuroda's 1st identity.

The circuit prototype in Figure 2-11 is non realizable since four series stubs still exist. Therefore additional unit elements are required as in the Figure 2-12.

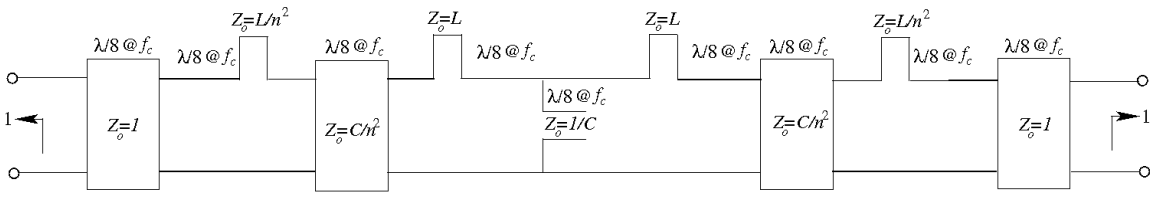

Figure 2-12: A normalized distributed circuit of Figure 2-11 after adding two unit elements.

Figure 2-13 illustrates a distributed model of a 5 elements open-circuited stub LPF with a cut-off frequency of 4 GHz and 0.5 dB equal-ripple characteristics after applying Kuroda's 2nd identity to the prototype in Figure 2-12. The corresponding stub and transmission line section lengths, as well as the widths after impedance and frequency scaling are given in Table 2.2.

Impedance scaling is used to scale the source and load unity impedances into 50 Ω impedances in addition to stub's impedances as in the following equation

$$Z_{Scaled} = Z_o \times 50\Omega \tag{2.8}$$

where Z_{Scaled} is the impedance after scaling and Z_o is the normalized impedance.

Frequency scaling is used to change the frequency from unity to the desired frequency ω_C as described in the following equation

$$\omega_{Scaled} = \frac{\omega}{\omega_C} \tag{2.9}$$

where ω_{Scaled} is the radian frequency after scaling, ω is the unity frequency, and ω_C is the desired frequency.

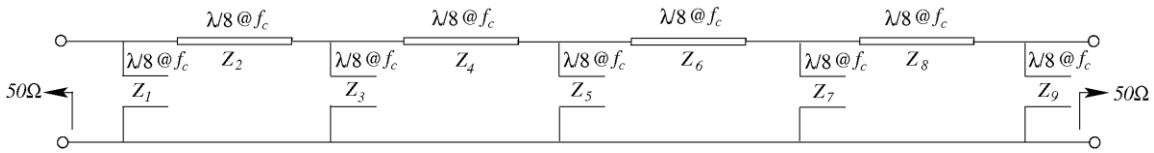

Figure 2-13: A distributed circuit model of a 5 elements open-circuited stub LPF design after using Richard's transformation and Kuroda's identities.

Table 2.2: 5 Elements Open-Circuited Stubs LPF Design at 4 GHz Cut-Off Frequency.

Element Value	Impedances (Ω)	Electrical Length	Length (mm)	Width (mm)
C_1=1.7058	Z_0=50	45^0	4.47	3.0
L_2=1.2296	Z_1=129.3			0.28
C_3=2.5408	Z_2=81.52			1.14
L_4=1.2296	Z_3=24.04			8.74
C_5=1.7058	Z_4=79.96			1.19
	Z_5=19.68			11.27
	Z_6=79.96			1.19
	Z_7=24.04			8.74
	Z_8=81.52			1.14
	Z_9=129.3			0.28

2.1.3.2 Proposed Open-Circuited Stub Configuration

The proposed open-circuited stub configuration (Figure 2-14) is easier to realize, more compact in size, and has fewer concerns for high current densities as compared with the stepped impedance configuration.

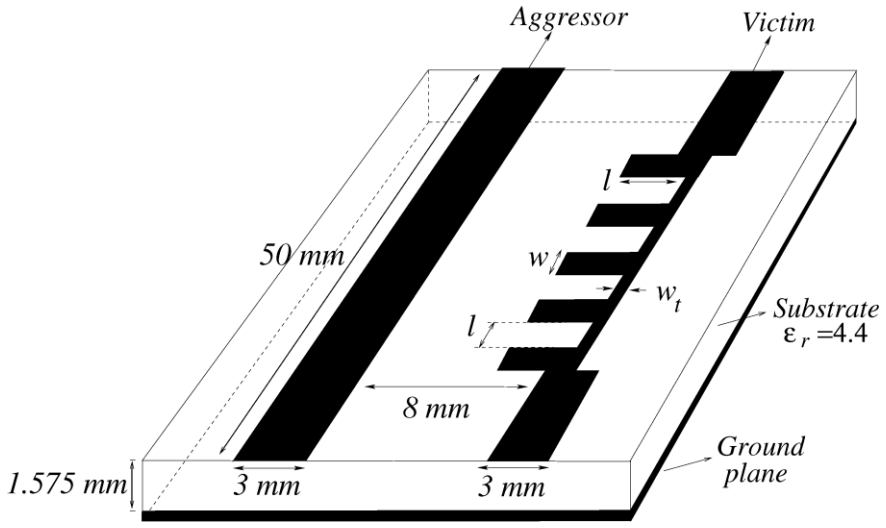

Figure 2-14: PCB structure of an open-circuited stub configuration with 5 elements.

The proposed structure employs a uniform stub width (w) and a uniform transmission line section width (w_t). These widths may be selected to lie within the minimum and the maximum values calculated for the LPF design. For example, for the 5 elements design given in Table 2.2, the width for a stub can be selected between 0.28 mm and 11.27 mm, while the width for a transmission line section can be selected to be around 1 mm. As is the case in stepped impedance design, choosing particular widths uniformly for all stubs and for all transmission line sections will affect the cutoff frequency and the return loss of the filter. However, in this case, cutoff frequency and return loss are not the primary concerns.

2.2 Results and Discussions

Both conventional and proposed PCB configurations were simulated using *ANSYS HFSS* [19] to calculate the far-end crosstalk (*i.e.* S_{41}) over a sweep of frequency from 0 to 6 GHz. A comparison of the calculated results is presented below. First, the crosstalk between uniform adjacent PCB traces (Figure 2-1) using a conventional guard trace (Figure 2-2) and a guard trace with vias (Figure 2-3) was calculated. The results, plotted in Figure 2-15, show that the guard trace alone does not provide any significant improvement in the crosstalk reduction. Similarly, using the guard trace with via fences shows a slight but insignificant improvement in crosstalk reduction.

Next, the performance of the stepped impedance configuration (Figure 2-5) employing 3 mm long elements and the performance of the proposed open-circuited stub configuration (Figure 2-14) with w =4.4 mm stub width, w_t =0.6 mm transmission line

sections width, and l=5.8 mm element (*i.e.* Stubs and TL sections) lengths were investigated.

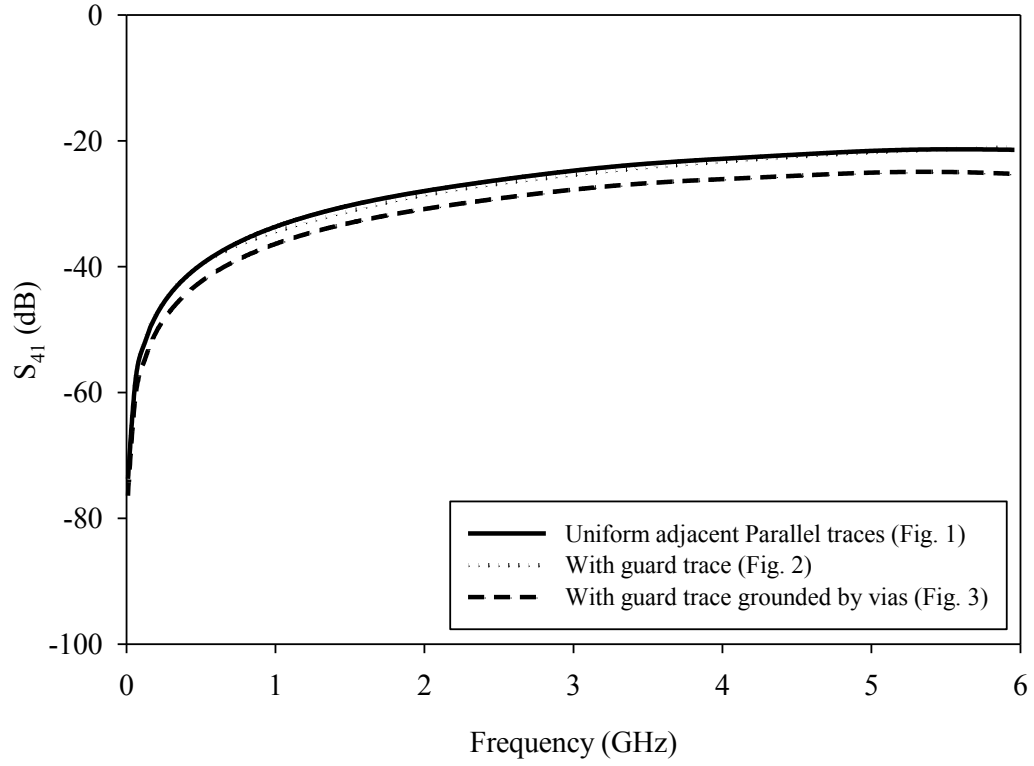

Figure 2-15: Comparison of far-end crosstalk in adjacent PCB traces using a guard trace and a guard trace grounded with vias.

As can be seen in Figure 2-16, the proposed design with open-circuited stubs provides significant reduction in crosstalk when compared to the performance of the guard trace configurations in Figure 2-15 as well as compared to the stepped impedance configuration. It is observed that the steepest crosstalk reduction (*i.e.* around 4 GHz) occur according to the location of the cutoff frequency of the victim trace. Moreover, it can be observed that the crosstalk can be further reduced by increasing the number of elements in both the stepped impedance and the open-circuited stub configurations.

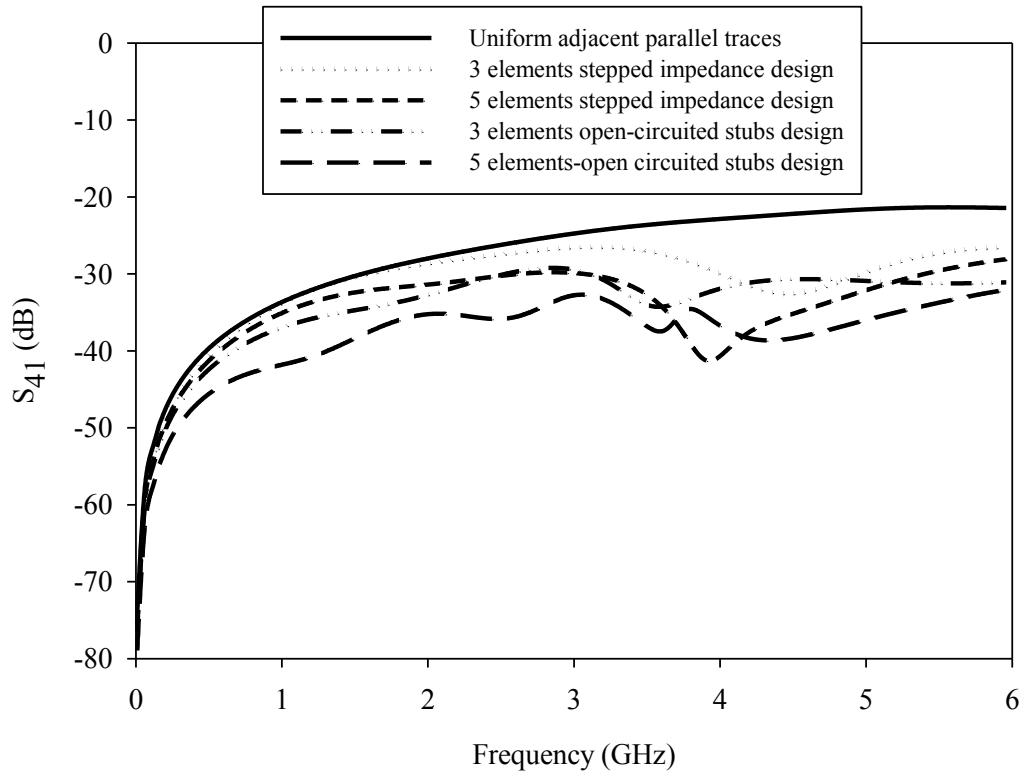

Figure 2-16: Far-end crosstalk in PCB traces using the proposed configurations.

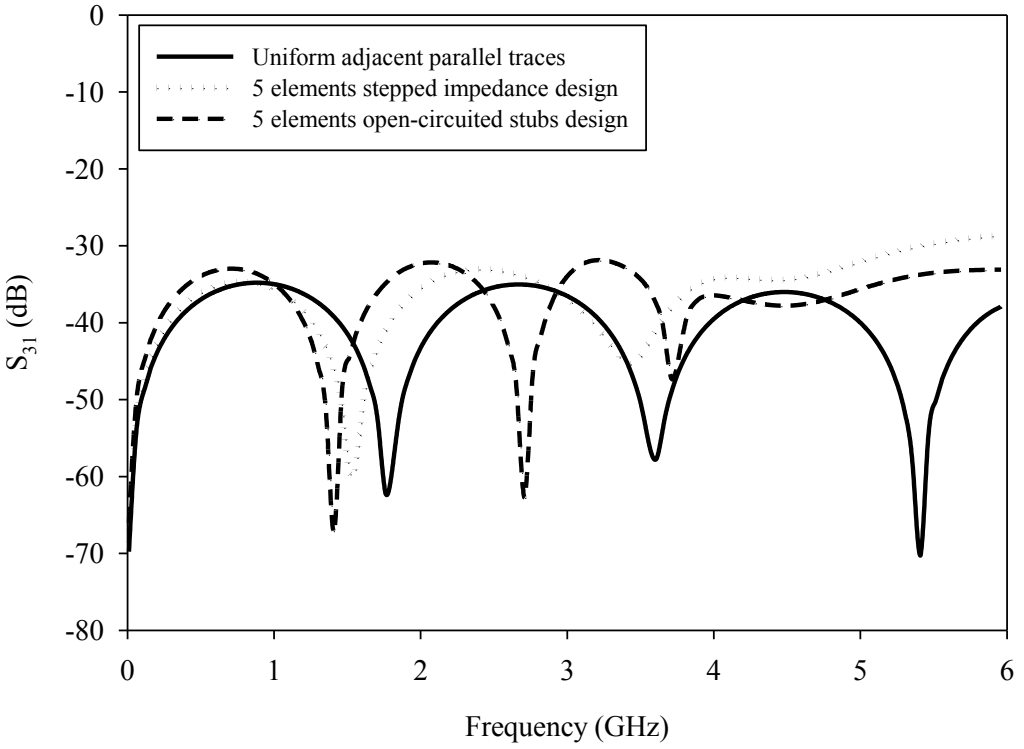

Figure 2-17: Comparison between the proposed configurations and the uniform trace configuration for the near-end crosstalk.

A comparison of the near-end coupling, as plotted in Figure 2-17, shows that the proposed configurations provide no improvement as compared to the reference configuration (*i.e.* uniform adjacent parallel traces).

Figure 2-18 shows that the performance of the proposed configurations has a LPF frequency characteristic, and the performance is relatively similar for both designs in terms of the return loss (S_{33}) and the transmission coefficient (S_{43}). Moreover, the return loss levels are acceptable for the proposed configurations.

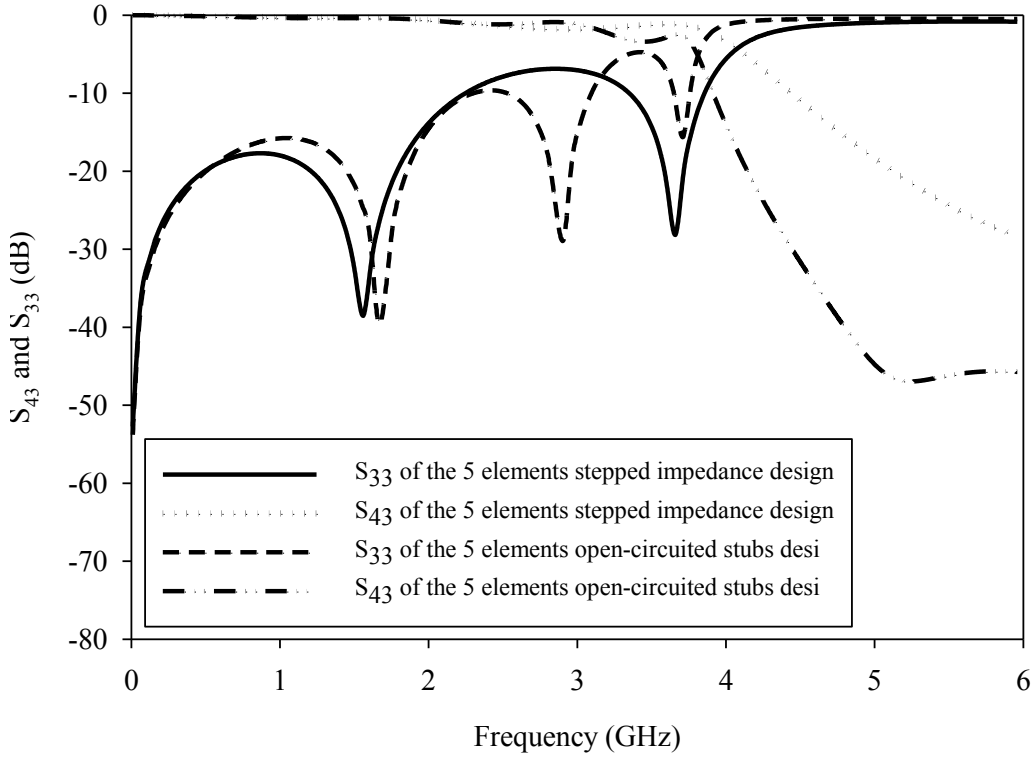

Figure 2-18: LPF frequency characteristics for both proposed configurations.

Figure 2-19 illustrates the radiated emissions from the proposed PCB configurations (Figure 2-5 and Figure 2-14) as well as the reference configuration (Figure 2-1). With the aid of *HFSS*, the magnitude of the electric field $|E|_{max}$ radiated by the PCB structures without the dielectric material was calculated on a hemispherical surface with

radius equal to 1 m. The PCB structure is located at the centre of the hemisphere and a 1 V voltage source is used to excite the aggressor trace, (*i.e.* at port 1) which connects between the uniform trace and an infinite ground plane [20]. Figure 2-19 shows that by varying the source frequency from 0.1 to 6 GHz, the 5 elements stepped impedance design has relatively similar radiated emission impact as compared to the uniform parallel trace design, while the 5 elements open-circuited stubs design has relatively high radiation emissions.

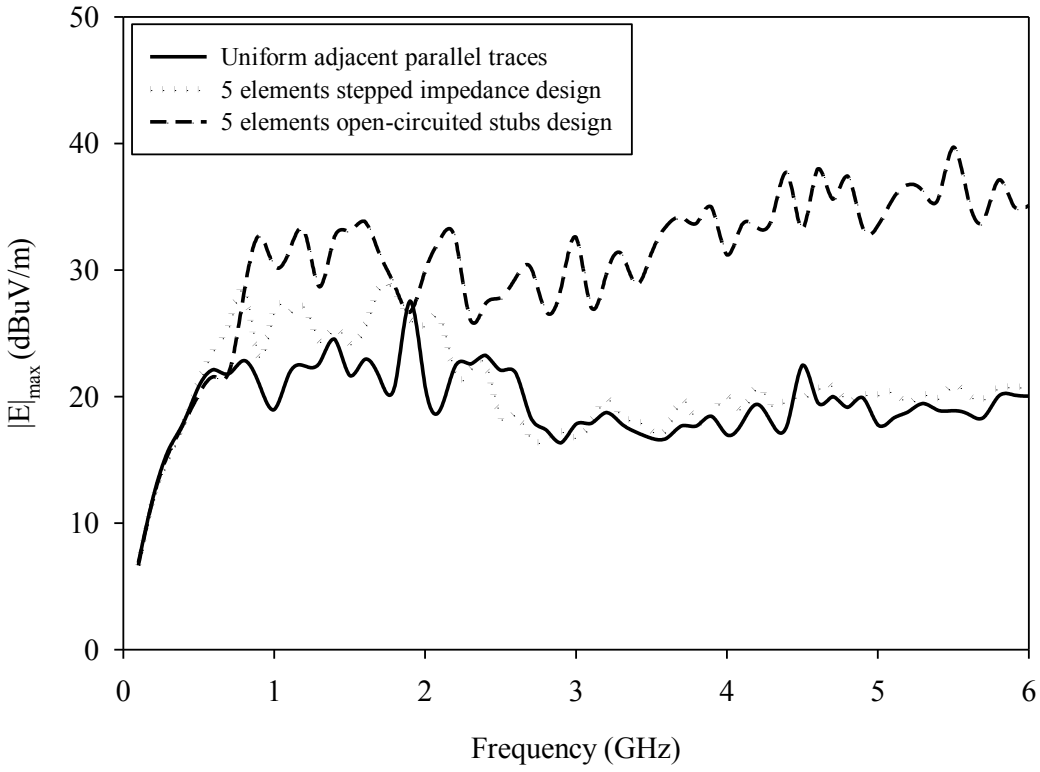

Figure 2-19: Magnitude of radiated electric field from the proposed PCB configurations.

2.3 Conclusions

In this chapter, two novel EMC trace (*i.e.* stepped impedance and open-circuited stub) configurations employing uniform elements were investigated for reduced far-end crosstalk in adjacent PCB traces. Moreover, the proposed approaches are easier to implement in the EMC prototype testing and provide better crosstalk reduction when compared with the conventional techniques. The performance of the proposed designs was found to be comparable to the LPF design. Both configurations provide an improved far-end crosstalk reduction; however, the open-circuited stub design exhibits better performance, more compactness, and better handling of high current densities when compared to the stepped impedance design. One drawback is that the open-circuited stub design has higher radiated emissions as compared to the stepped impedance design.

Chapter 3

Multilayered Multiband-Notched UWB Antenna Design

Recently, there has been increasing demand in designing UWB systems, and more particularly so after the release of the frequency band 3.1-10.6 GHz by the Federal Communications Commission (FCC) [21]. The main objective of UWB is the handling of high data-rates in the presence of wireless communication standards, which cause EM interference with UWB systems, such as the worldwide interoperability for microwave access (WiMAX) system operating at 3.3-3.7 GHz, satellite communication systems such as the Indian national satellite (INSAT) system operating at 4.5-4.8 GHz, and wireless local area network (WLAN) system operating at 5.15-5.35 GHz and 5.725-5.825 GHz. Generally, UWB antennas should have sufficient impedance matching for broad operating bandwidth and high-gain radiation in desired directions. Since antennas are essential components for a host system application, it is desirable to design UWB antennas that contain narrow band-notches within the UWB frequency range. The early works on frequency band-rejected UWB antennas were realized by utilizing small strip bars [22-24], open-loop resonators [25], U-shaped slots [26-28], Ω-shaped slots [29], half-mode substrate integrated waveguide cavities [30], and pentagonal radiating patch with two bent slots [31].

In [22-29], however, the elements were constructed on the same layer within the antenna radiator or on the back side of the same layer for generating single and/or dual frequency band-notched antennas. Therefore, due to the space limitation, it is difficult to generate multiple band-notches and control the width of the band-notch. On the other hand, in [30], the antenna is attached to a single cavity below the feed line to provide multiple stopbands. This leads to an increase in the antenna size. Moreover, the antenna design in [30] has complicated structures leading to increased fabrication costs and difficulty in the integration with microwave integrated circuits. In [31], dual rejection bands of the antenna are obtained so that three operating bands are covered (*i.e.* WiMAX and upper/lower WLAN). Here, both upper and lower WLAN bands are covered using single rejection band. This leads to inefficient utilization of the available bandwidth.

The objective of this chapter was to develop a simple and compact realization with stable radiation performance of a quad band-notched planar antenna suitable for UWB applications. It will be shown that the proposed antenna in Figure 3-1 possesses the desirable feature of compactness, while achieving an acceptable impedance bandwidth performance. Ring resonators have been utilized because of their narrow bandwidth, compact size, and low radiation loss [32] essential to ensuring a relatively omnidirectional far-field radiation pattern (which is originally due to the actual rectangular slot patch monopole antenna). The monopole planar antenna type is commonly used due to its wide bandwidth, simple structure, and low cost.

The organization of the chapter is as follows. Section 3.1 describes the configuration of the proposed antenna. Section 3.2 presents measured and simulated results, and conclusions are given in Section 3.3.

3.1 Antenna Configuration

In monopole UWB antenna illustrated in Figure 3-1, the top side of layer 3 is realized using a rectangular slot patch with a 50 Ω Microstrip feed-line. Broadening the bandwidth of this antenna is achieved by increasing the width of the monopole or the rectangular patch [33] and the suitable choice of feeding technique. Alternatively, one may increase bandwidth by increasing the substrate thickness or by decreasing the relative permittivity of a substrate [34]. Impedance bandwidth is inversely proportional to the Q of the antenna. Q of a resonator is the ratio of the stored energy to the dissipated energy in a resonator.

Four band-notches within the UWB frequency range are achieved by vertically aligning four ring resonators (with their centers aligned along an axis) on multilayered planes. Here, each ring is responsible for creating a frequency band-notch.

The antenna is printed on four-layers of Rogers substrate (RO4003) [35] with a dielectric constant of 3.55 and a loss tangent of 0.0027. The thicknesses of the layers have been arbitrarily selected; the thickness of layer 1, 2, and 3 is set to be 0.508 mm and the top layer (layer 4) is set to be 0.8128 mm as illustrated in Figure 3-1(c). The antenna is connected to a 3.5mm SubMiniature version A (SMA) connector between a 50 Ω feed-line on top side of layer 3 and the ground plane on bottom side of layer 1. The length of layer 4 (L_s) is implemented to be much shorter than the overall antenna length (L) as depicted in Figure 3-1(a) to make the connection through SMA connectors possible and to allow integration of RF front-ends. SMA connectors are usually preferred for planar components because of their excellent broadband performance between DC and 18 GHz.

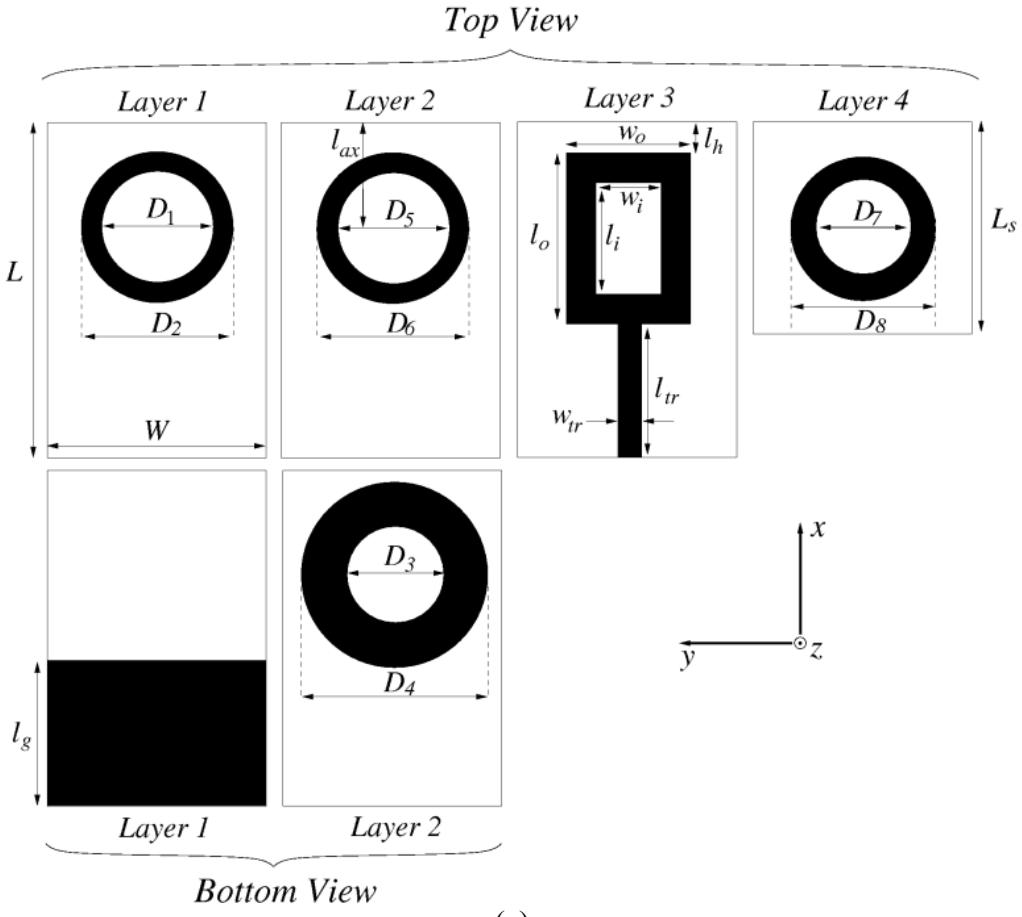

(a)

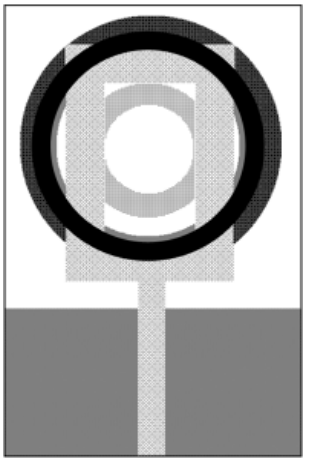

(b)

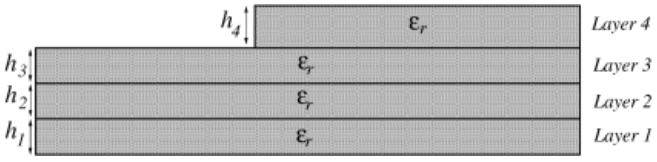

(c)

Figure 3-1: Structure of the proposed quad band-notched UWB antenna in four layers configuration (a) 2D double-sided view of each layer; (b) top view; and (c) side view.

Full-wave EM simulations are performed using *ANSYS HFSS* leading to the following optimal dimensions of the proposed antenna as listed in Table 3.1.

Table 3.1: Dimensions of the Proposed Quad Band-Notched UWB Antenna.

Symbol	Value (mm)	Symbol	Value (mm)
L	33.5	l_h	2.5
W	30	l_{ax}	9.2
L_s	19.7	D_1	10.2
l_g	12.1	D_2	13
l_{tr}	14	D_3	4.8
w_{tr}	3.5	D_4	13.6
l_o	17	D_5	8
w_o	11.2	D_6	10.8
l_i	10.6	D_7	11.2
w_i	4.8	D_8	17.6

In this design, the fundamental stopband center frequency f_o corresponding to each ring is approximately given by

$$2\pi r = \lambda_g \,. \tag{3.1a}$$

Therefore,

$$f_o = \frac{c}{\pi D \sqrt{\varepsilon_{reff}}} \,, \tag{3.1b}$$

where D is the mean diameter of the ring, λ_g is the guided wavelength, c is the speed of light in free space, and ε_{reff} is the effective relative dielectric constant. The arrangement of the ring resonators could be either above and/or below the actual monopole antenna radiator. Each resonator in the structure resonates at different resonant frequencies by varying the mean diameter. The ring on top of layer 1 is responsible for generating the rejection-band for the INSAT. Rings on the top and bottom sides of layer 2

are responsible for generating the rejection-bands for lower and upper WLAN standards respectively, while the ring on top of layer 4 is responsible for generating the rejection-band for the WiMAX standard.

3.2 Results and Discussions

In this section, parametric studies have been carried out using *ANSYS HFSS* for providing a better understanding of the antenna operation. Also, measured impedance bandwidth and radiation pattern are discussed. For convenience, results in Figure 3-2, Figure 3-3, and Figure 3-4 are obtained using one ring resonator located on the top side of layer 4, with the other resonators removed.

Figure 3-2 shows the variation of the Voltage Standing Wave Ratio (VSWR) with frequency for different mean diameters of the top ring resonator. VSWR measures the ratio between the amplitudes of the maximum standing wave to the minimum standing wave and can be calculated using the following equation

$$VSWR = \frac{1+|\Gamma|}{1-|\Gamma|} \tag{3.2}$$

where $|\Gamma|$ is the magnitude of the reflection coefficient which is the ratio of the reflected wave magnitude to the incident wave magnitude at a transmission line load. If the impedance of the feed-line and the antenna input impedance are not identical then there will be a mismatch and some of the incident signal will be reflected back to the source. In Figure 3-2, increasing the mean diameter of the ring resonator leads to a negative shift in the resonant frequency.

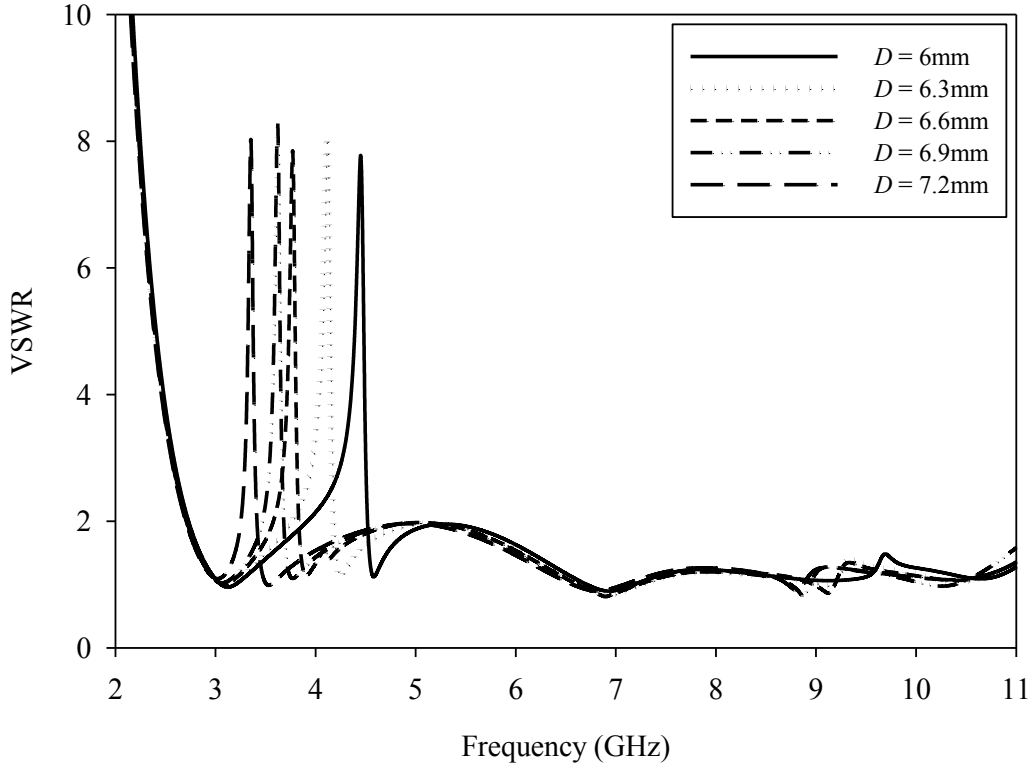

Figure 3-2: Simulated VSWR versus frequency by varying mean diameter (D) of the top ring resonator on layer 4.

From Figure 3-3, it can be seen that for a given rejected center frequency, the bandwidth is a function of the axial position along the x-axis as well as the mean diameter (D) and the ring width (w_r).

By fixing the axial position (l_{ax}) and applying the above analysis, the optimized dimensions for each of the ring resonators (D and w_r) were found using *ANSYS HFSS* after calculating the mean diameter using (3.1b). Each ring is optimized to cover a specific wireless standard as listed in Table 3.2.

Table 3.2: Calculated and Optimized Ring Resonator's Parameters Corresponding to the Rejected Center Frequency and the Required Bandwidth.

Wireless Standard	f_o (GHz)	Required BW (GHz)	D Calculated (mm)	D Optimized (mm)	W_r (mm)
WiMAX	3.5	0.4	15	14.4	6.4
INSAT	4.65	0.3	11.3	11.6	2.8
Lower WLAN	5.25	0.2	9.1	9.2	8.8
Upper WLAN	5.775	0.1	10	9.4	2.8

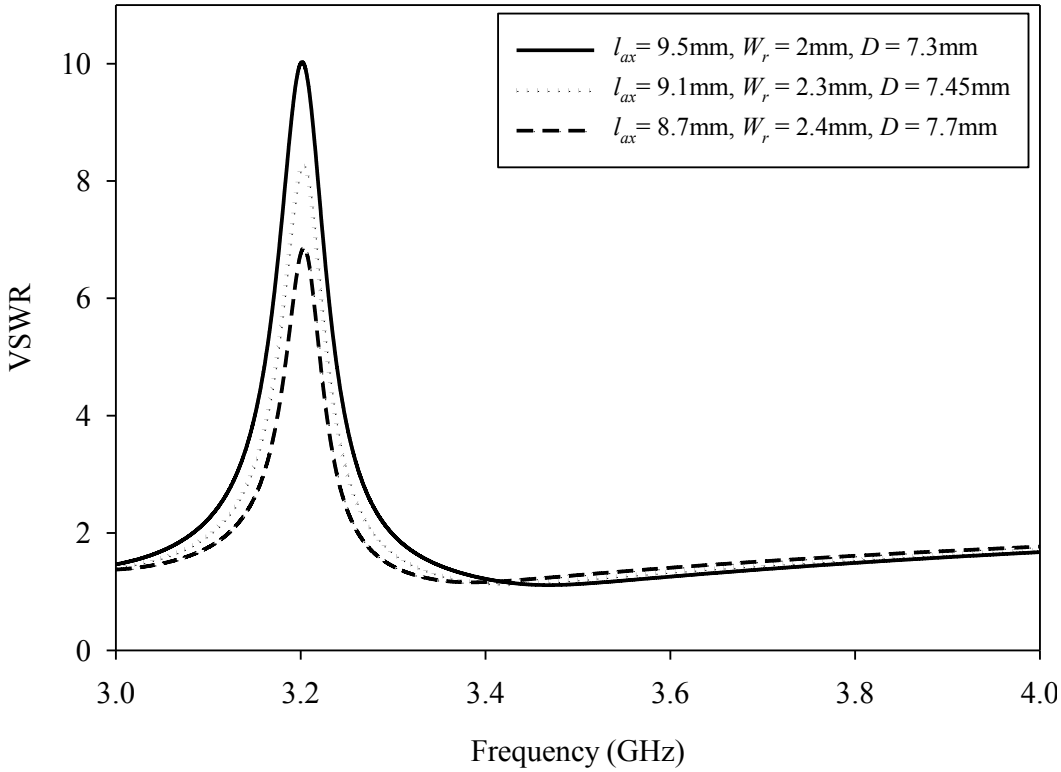

Figure 3-3: Simulated VSWR by varying the axial position along the x-direction and adjusting both width and mean diameter of the top ring resonator.

Figure 3-4 depicts the simulated current distributions at the notch frequency (*i.e.* 3.2 GHz). As illustrated in Figure 3-4(a), the direction of the current flow on the antenna radiator is opposite to those on the ring resonator.

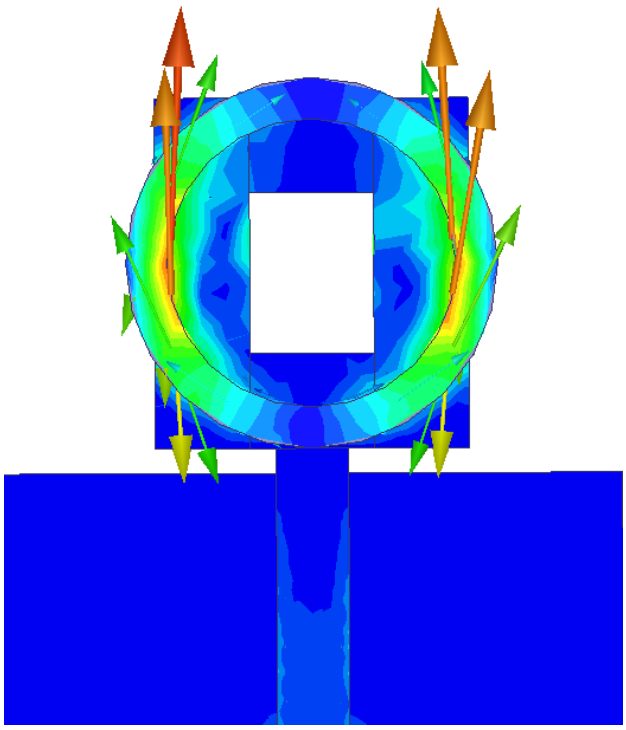

(a)

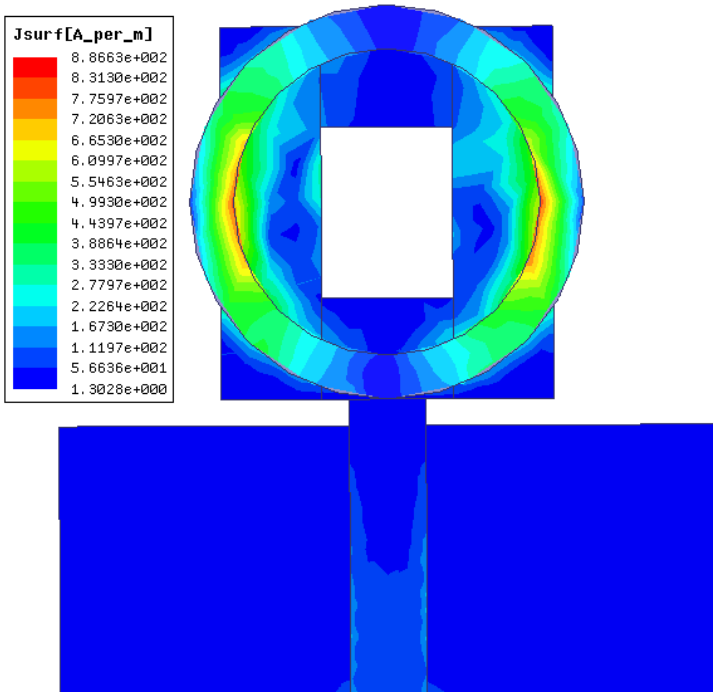

(b)

Figure 3-4: Simulated current distributions at the notch frequency: (a) vector surface currents; (b) surface current magnitudes.

In addition, Figure 3-4(b) shows that the coupling is stronger where both the ring resonator and the antenna radiator are closer to each other (*i.e.* left and right sides of the antenna radiator). In other words, the ring resonator has a significant effect on the antenna performance which is described by the frequency rejection band.

Figure 3-5 shows both measured and full-wave EM simulated VSWR characteristics of the proposed antenna. The frequency performance of the antenna demonstrates four rejection-bands with VSWR > 2 covering all of WiMAX, INSAT, and lower/upper WLAN applications, while maintaining VSWR < 2 at out of the rejection-bands. A very good agreement between measured and simulated results is observed. Slight discrepancies could be attributed to the effects of the SMA connector which is not considered in the simulation.

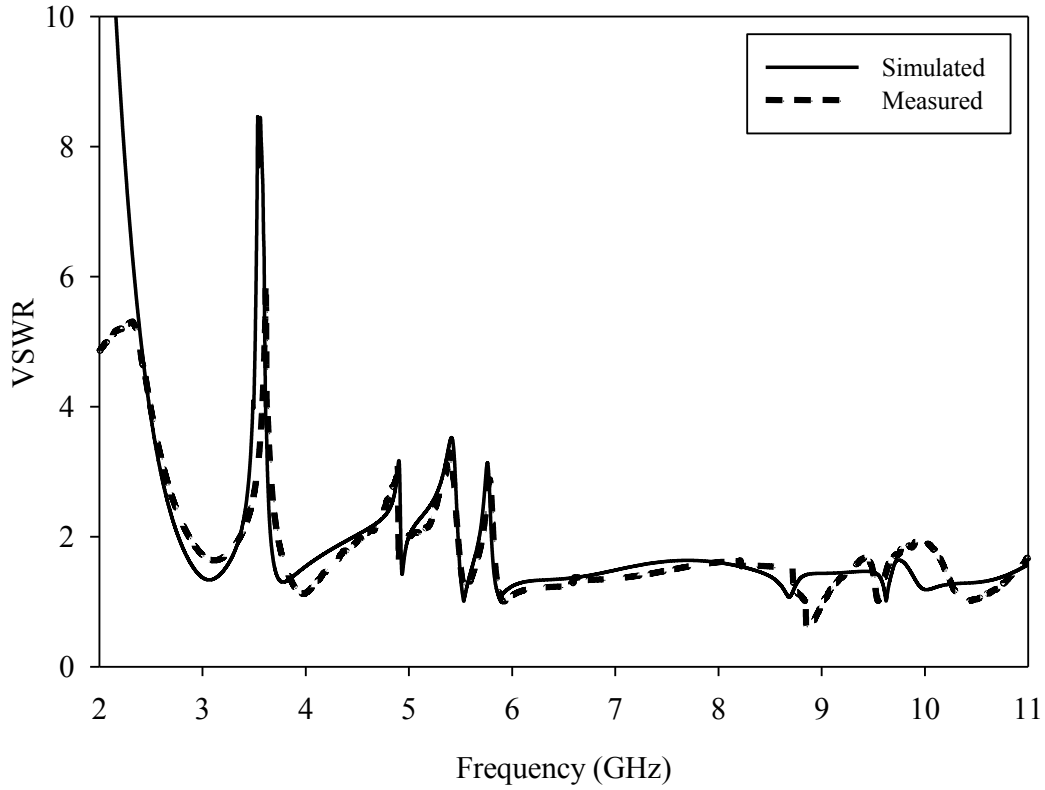

Figure 3-5: Measured and simulated VSWR characteristics of the proposed antenna.

Measurements are carried out for the far-field radiation pattern on the proposed antenna in a custom built anechoic chamber with a quad ridged horn antenna as a reference at *Wrtest Labs* [36]. The quad ridged antenna was selected because it is a well-known standard for wideband applications operating between 1 to 18 GHz with both vertical and horizontal polarization and an average gain of approximately 10 dB.

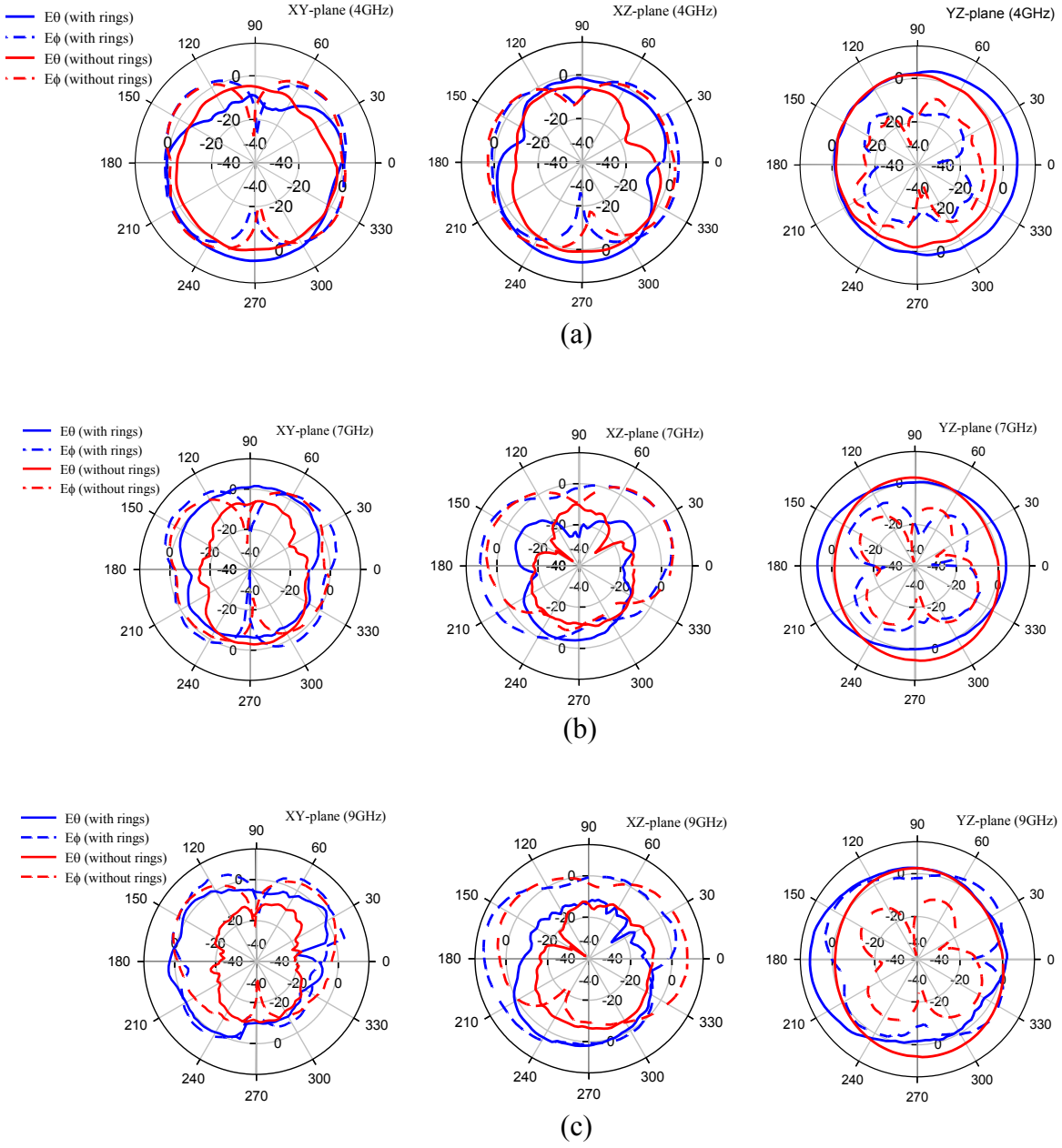

Figure 3-6: Measured far-field radiation pattern of the proposed antenna with/without ring resonators at a) 4 GHz; b) 7 GHz; and c) 9 GHz.

Figure 3-6 depicts the measured radiation patterns of the proposed antenna with and without ring resonators along xy, xz and yz planes at 4, 7, and 9 GHz, respectively. The H-plane (*i.e.* yz-plane) patterns are almost omnidirectional for the three frequencies, in a manner similar to the conventional dipole antenna. Omni-directional radiation pattern implies that the waves passing through an antenna have the ability to travel in all directions. This allows user mobility and freedom in the transmitter or receiver position. On the other hand, the E-plane (*i.e.* xy-plane) patterns are relatively similar to those of a monopole.

A photograph of the implemented quad band-notched UWB antenna connected with the 50 Ω SMA mounted on a ferrite material around the feed cable is displayed in Figure 3-7. The antenna was fabricated at Hughes Circuit, Inc. [37]. Ferrite material has been placed to avoid any concerns arising from RF currents running down the feed cable [38].

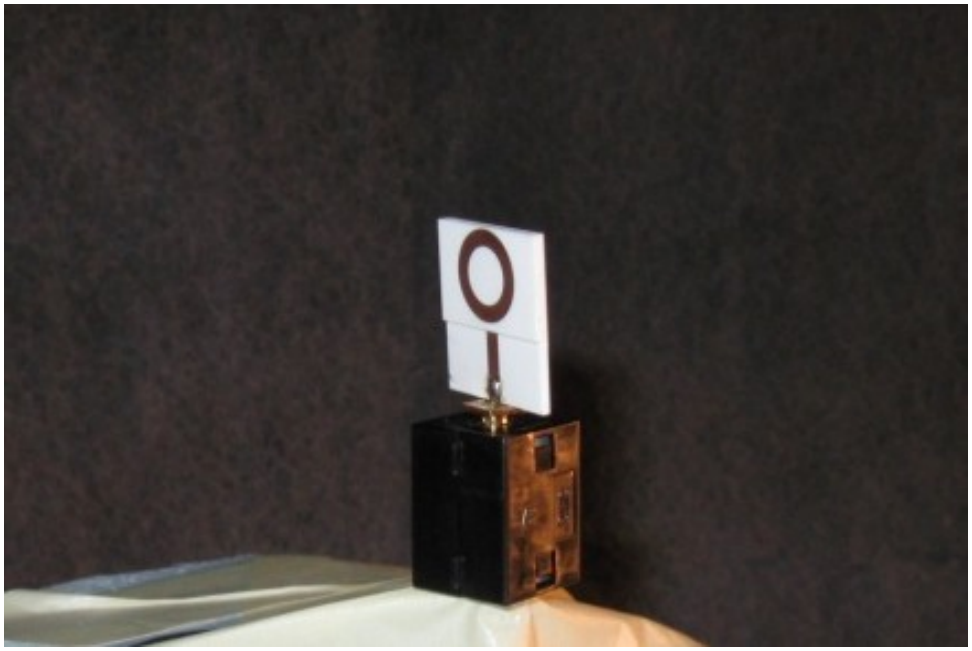

Figure 3-7: A photograph of the fabricated antenna.

Figure 3-8 shows a plot of the simulated radiation efficiency versus frequency. Antenna radiation efficiency is the ratio of the radiated power to the input power of an antenna and is given using the following relation:

$$Antenna Efficiency\ (\eta) = \frac{P_{Rad}}{P_{Input}} \tag{3.3}$$

where P_{Rad} is the antenna radiated power and P_{Input} is the antenna input power.

The radiation efficiency data in Figure 3-7 illustrates high attenuations at the antenna quad-band notches and excellent radiation efficiency at out of the band notches. Generally, conductor and dielectric losses should be minimized in order to maximize radiation efficiency.

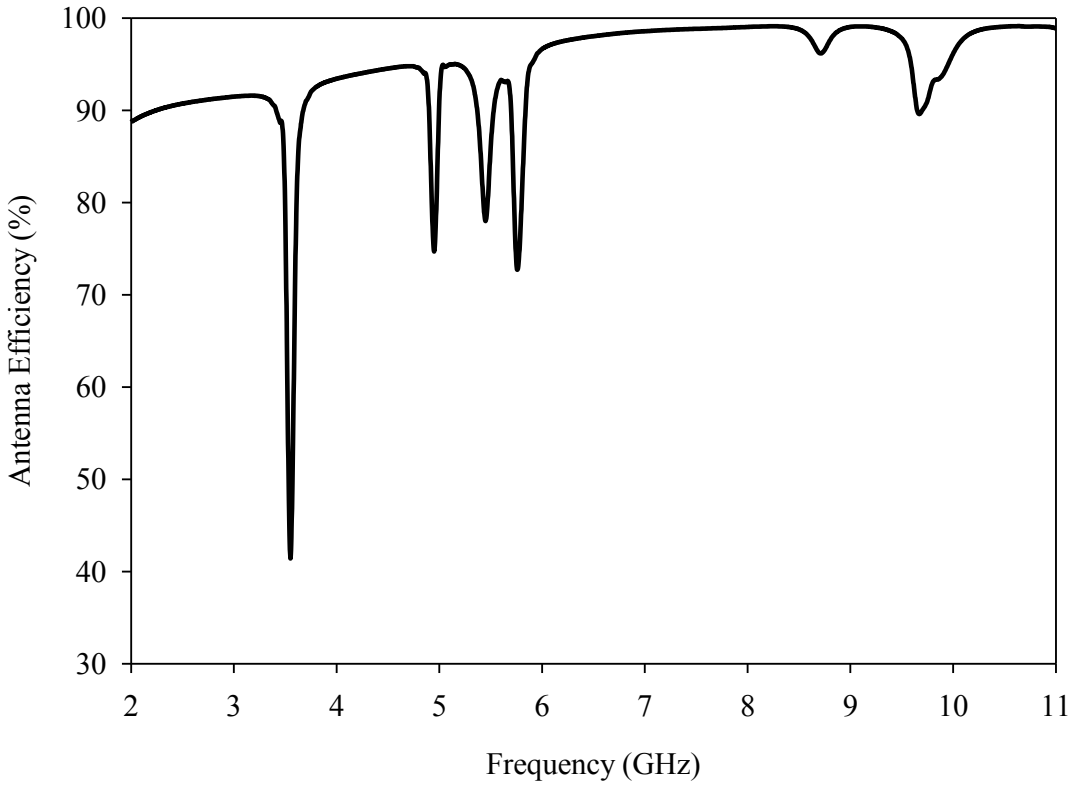

Figure 3-8: Simulated antenna efficiency versus frequency.

Figure 3-9 shows the tested antenna gain with an average gain equal to 3.5 dB. The gain was measured at the broadside direction as shown in Figure 3-9, where two identical antennas are separated by a distance *d* of 0.98 m. The transmission coefficient S_{21} was measured after a full two-port calibration was carried out to a Rhode & Schwarz ZVB20 vector network analyzer (VNA) and used to calculate the gain of the antenna using the following formula [39]:

$$|S_{21}|^2 = \frac{P_R}{P_T} = G_T \times G_R \times \left(\frac{\lambda}{4\pi d}\right)^2 \tag{3.4}$$

where G_T, G_R are, respectively, the transmitter and receiver gain, and are equal in this case. P_T, P_R are the transmitted and received powers, and λ is free space wavelength in meters. It is clearly evident that at the notch bands, the antenna gain drops sharply.

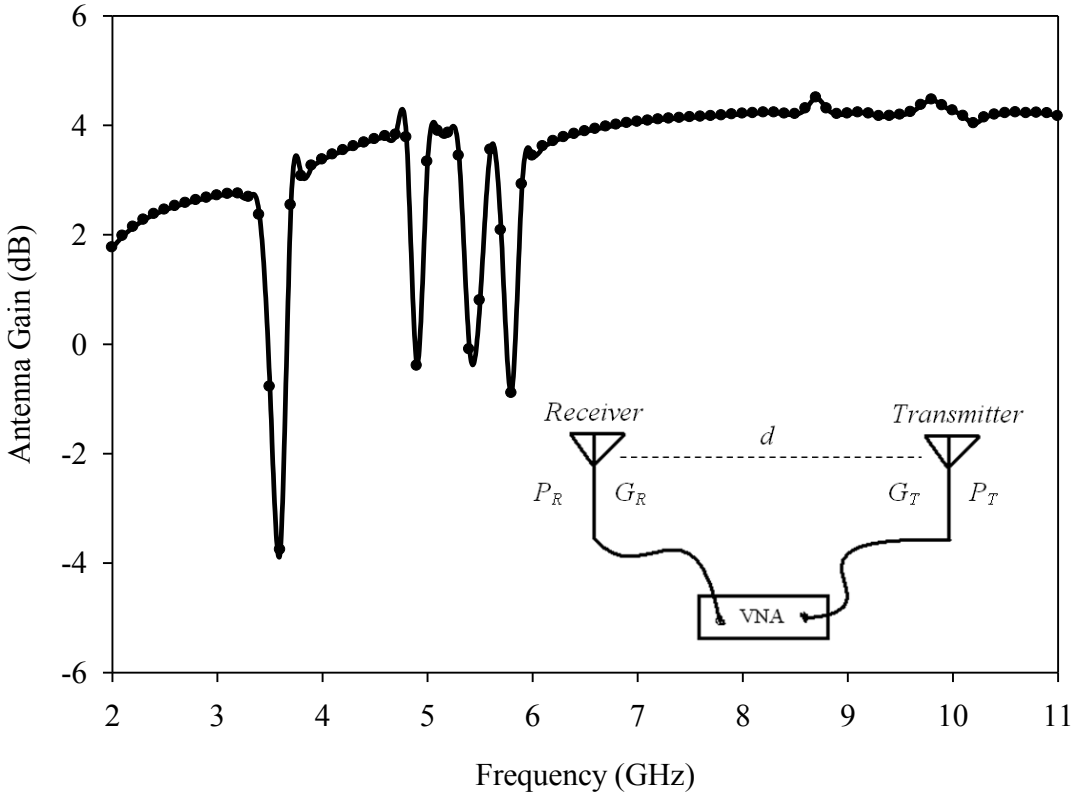

Figure 3-9: Measured gain of the proposed antenna versus frequency.

3.3 Conclusions

A compact and simple multilayered quad band-notched UWB antenna for WiMAX, INSAT, and lower/upper WLAN applications has been proposed. The overall antenna size is 33.5mm × 30 mm × 2.34 mm which is more compact when compared with the recently published multiple-band notched antenna in [30] with antenna size of (108mm × 50mm × 1.136mm). The proposed antenna radiator design is comprised of a rectangular slot patch fed with a 50Ω Microstrip line. Quad band-notched frequencies are realized by adding four ring resonators sharing the same vertical axis and implemented on multiple layers. Having the same vertical axis and allowing the possibility to arrange the ring resonators above and/or below the actual antenna led to straightforward fabrication when compared to the existing UWB antennas with band-notches.

The antenna has been fabricated and tested for the purpose of validating the design. The antenna exhibits good impedance matching and radiation performance. Finally, the antenna is advantageous in modern multilayered circuits such as monolithic microwave integrated circuits (MMICs) and low temperature co-fired ceramic (LTCC) technologies.

Chapter 4

Dual-Mode In-Line SIW Filters with Advanced Frequency Characteristics

The development of SIW technology has opened new perspectives for circuits and systems in the microwave and millimeter-wave frequency range. Based on a synthesized waveguide in a planar dielectric substrate with two rows of metallic vias [40], this low cost realization of the traditional waveguide circuit inherits the merits from both the Microstrip for easy integration and the waveguide for low radiation loss. Among the different classes of SIW components proposed in the literature, SIW filters have received particular attention, due to the possibility of achieving high quality-factor and better selectivity when compared to classical planar filters in Microstrip and coplanar waveguide (CW) technology.

Most efforts have been focused on implementing SIW filters to operate in the dominant transverse electric (TE_{10}) mode since it has the lowest attenuation of all modes, [41, 42] and few works are concerned about SIW dual-mode filters. Dual-mode filters have been widely used in satellite communications due to their reduced mass and volume. In dual-mode bandpass filters, the number of resonators required for a given filter can be reduced by half, resulting in a more compact filter configuration [43-45].

Moreover, SIW dual-mode bandpass filters exhibit high skirt selectivity and symmetric transmission zeros [46]. The early works on SIW dual-mode filters are focused on realizing dual-mode frequency characteristics in single and multi-layer configurations [47-49]. However, SIW dual-mode filters suffer from limited upper stopband attenuation and thus will need to be cascaded by a lowpass cleanup filter [50]. The filter presented in [50] is cascaded by a lowpass cleanup filter which is realized outside the SIW cavities nearby the input/output feed-line. This leads to inefficient utilization of the filter's area.

To this end, the novelty of this work is in implementing the cleanup LPF with wide stopband using DGS within the dual-mode SIW cavity area. This can be realized by etching off a defected pattern from the backside metallic ground plane with periodic structures. DGS provides rejection of certain harmonics and allows the realization of compact size components [51-54]. In addition, for the first time, advanced transfer characteristic has been achieved by realizing a dual-band frequency response using dual-mode SIW cavities.

The objective of this chapter is to present SIW dual-mode filters with an improved upper stopband performance and a dual-band frequency characteristic. It will be shown that the proposed filters possess the desirable feature of compactness while achieving excellent electrical performance.

The organization of this chapter is as follows. Section 4.1 describes the configuration of the proposed dual-mode filters with DGS as well as the simulated results of two different filter's orders; Section 4.2 discusses the realization of a dual-band dual-mode filter; while conclusions are given in Section 4.3.

4.1 Dual-Mode SIW Filter with an Improved Upper Stopband

Figure 4-1 depicts the coupling scheme of the DGS dual-mode SIW filter which consists of the two orthogonal resonant modes (TE_{102} and TE_{201}) in an SIW cavity (node 1 and node 2), and the cascaded LPF with wide stopband generated using DGS (node 3). It will be shown that the DGS occupies the area of the SIW cavity; hence, compact realization is achieved.

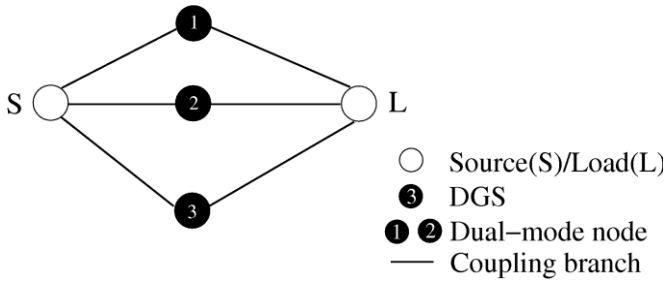

Figure 4-1: Coupling topology of the proposed filter.

A conventional waveguide has one conductor which confines the wave energy within its cavity and supports either TE or transverse magnetic (TM) modes. Waveguides can support an infinite number of modes and each has their own cut-off frequency. In conventional rectangular waveguide, the cutoff frequency f_{c10} of a TE_{10} mode waveguide resonator is computed from [18, 55]

$$f_{cmn} = \frac{c/\sqrt{\varepsilon_r}}{2}\sqrt{\left(\frac{m}{W}\right)^2 + \left(\frac{n}{H}\right)^2}\ , \tag{4.1}$$

by setting $m = 1$ and $n = 0$ leading to

$$f_{c10} = \frac{c/\sqrt{\varepsilon_r}}{2W}\ . \tag{4.2}$$

In (4.1), c is the speed of light in free space, ε_r is the dielectric constant of the material

filling the cavity, m and n are the mode numbers representing the number of half waves across the waveguide width and height respectively, W is the width of the resonator, and H is the height of the cavity. From (4.2), we can conclude that the lower the mode numbers, the lower the cutoff frequency.

The fundamental resonant frequency of a rectangular TE_{10} mode resonator is evaluated from

$$f_{rmnp} = \frac{c/\sqrt{\varepsilon_r}}{2}\sqrt{\left(\frac{m}{W}\right)^2 + \left(\frac{n}{H}\right)^2 + \left(\frac{p}{L}\right)^2} \tag{4.3}$$

by setting $m = 1$, $n = 0$ and $p = 1$ leading to

$$f_{r101} = \frac{c/\sqrt{\varepsilon_r}}{2}\sqrt{\left(\frac{1}{W}\right)^2 + \left(\frac{1}{L}\right)^2} \tag{4.4}$$

In (4.3), L is the length of the cavity and p is the number of half wavelengths along the cavity. The length of a waveguide resonator can then be determined upon solving (4.4) to give

$$L = \frac{1}{\sqrt{\left(\frac{4\varepsilon_r}{c^2}\right){f_{r101}}^2 - \left(\frac{1}{W}\right)^2}} \tag{4.5}$$

The first spurious passband of such a conventional waveguide filter is obtained by setting $p = 2$ for $m = 1$ and $n = 0$ in (4.3) leading to

$$f_{r102} = \frac{c/\sqrt{\varepsilon_r}}{2}\sqrt{\left(\frac{1}{W}\right)^2 + \left(\frac{2}{L}\right)^2} \tag{4.6}$$

In order to map from conventional waveguide dimensions into SIW demotions the following expression is used [56]:

$$SIW_{\_Dim} = WG_{\_Dim}\sqrt{\frac{\varepsilon_{r\_WG}}{\varepsilon_{r\_SIW}}} \tag{4.7}$$

where $WG_{\_Dim}$ is any dimension in the waveguide design, ε_{r_WG} is the permittivity inside the waveguide, and ε_{r_SIW} is the permittivity for the SIW substrate.

In dual-mode resonator, the condition that both modes resonate at the same frequency [57] in a rectangular cavity with *a*, *b*, and *l* sides is given by

$$(\frac{m\pi}{W})^2 + (\frac{n\pi}{L})^2 - (\frac{p\pi}{W})^2 - (\frac{q\pi}{L})^2 = 0 \tag{4.8}$$

Consequently, the initial dimension ratio between the length (*L*) and the width (*W*) of the resonator can be calculated using the following equation

$$\frac{W}{L} = \sqrt{\frac{m^2 - p^2}{q^2 - n^2}} \tag{4.9}$$

where (*m*, *n*) and (*p*, *q*) refer to the first and second mode respectively. It is assumed that the dimension *H* (*i.e.* cavity height) is equal to zero, since the proposed filters are realized using planar SIW technology.

The prototype response in Figure 4-2 operates as if it is comprised of a bandpass filter in cascade with a lowpass filter. This results in a bandpass response with an improved upper stopband performance as explained in the prototype response of Figure 4-2(c), where Figure 4-2(a) is a bandpass response with a fundamental passband centered at f_1 and a stopband that is limited to f_2 cascaded with a wide stopband lowpass response generated using DGS and covers the center frequency (f_1) as in Figure 4-2(b).

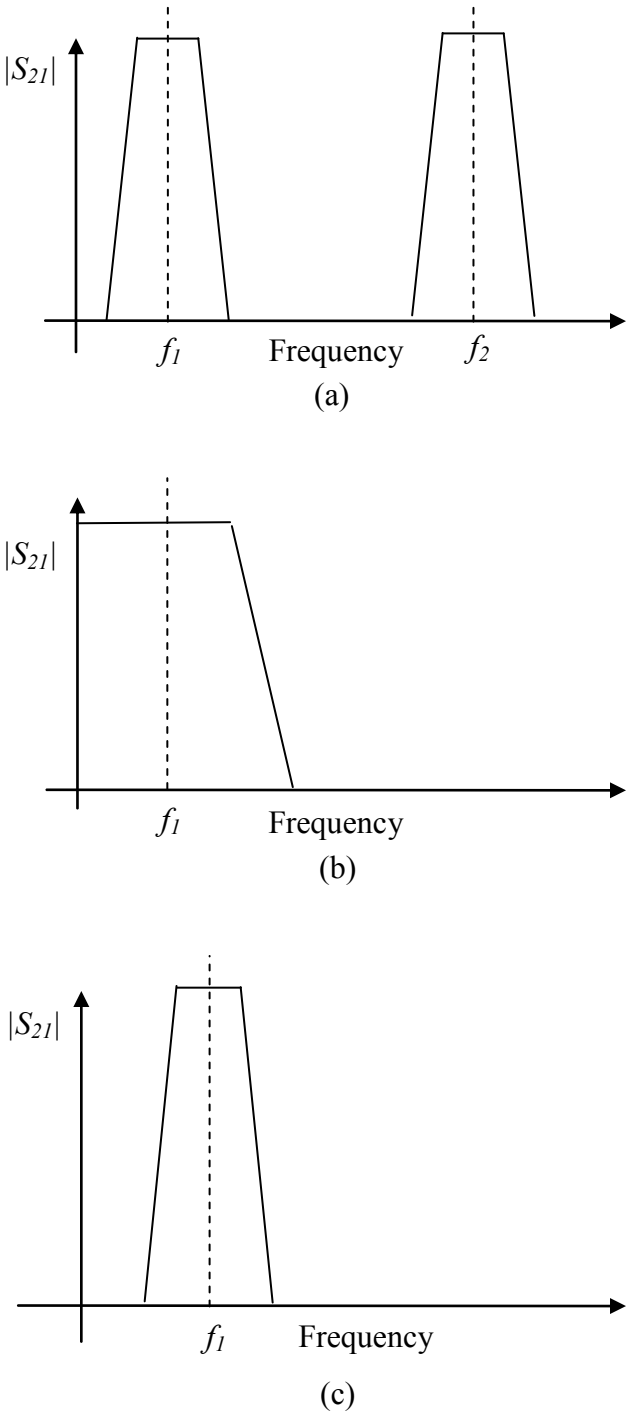

Figure 4-2 Bandpass prototype response cascaded with a LPF.

To excite the SIW ports, different possible topologies for coupling between a Microstrip transmission line and an SIW cavity can be used as illustrated in Figure 4-3.

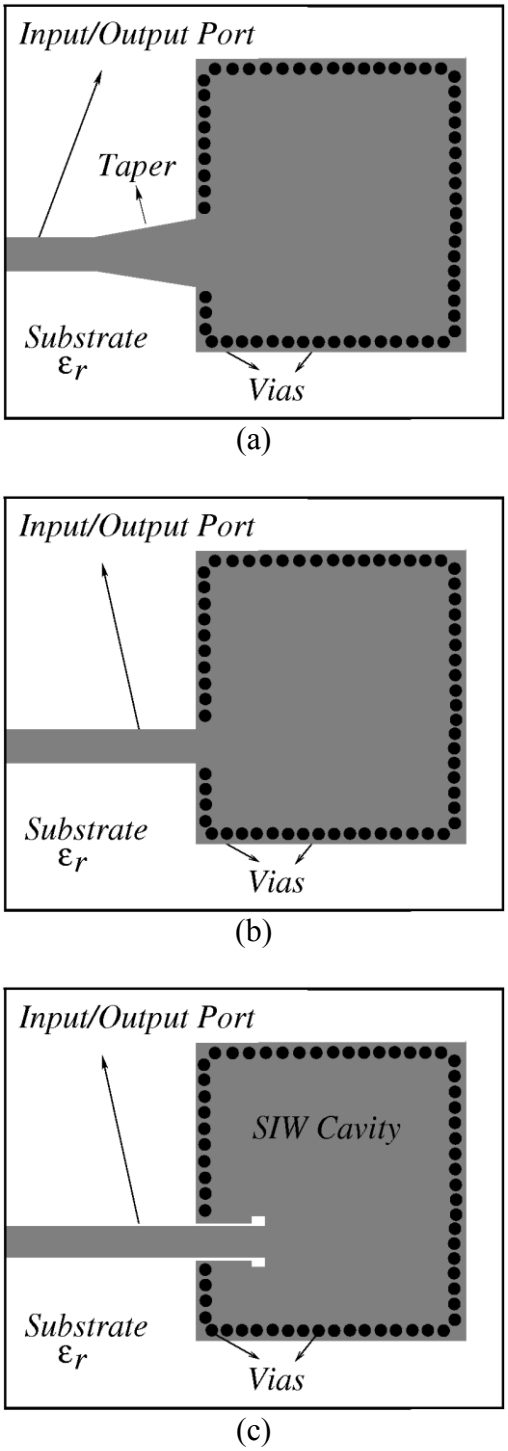

Figure 4-3 Input/output coupling configurations: (a) Linear tapered transition; (b) Direct coupling; (c) Slot-line coupling.

In Figure 4-3(a), a linear taper transition is used for coupling between the 50 Ω transmission line and the SIW cavity. However, this transition will add additional in-band loss. In Figure 4-3(b), direct coupling causes more energy transmission by higher order modes and thus results in a degrading the stopband performance, while in Figure 4-3(c) slot coupling has better stopband performance since less energy can be transferred by the higher order modes [58], however, the radiation caused by the slot coupling may reduce the unloaded quality factor.

Two different order filters with DGS will now be illustrated as in the following sections.

4.1.1 Single-Cavity Dual-Mode SIW Filter

Figure 4-4 illustrates the physical structure of a single-cavity dual-mode SIW filter with DGS. The structure is supported by a 0.508 mm thick Rogers RT/duroid 5880 substrate with a dielectric constant of 2.2 and a loss tangent of 0.0009. In SIW, the conditions where SIW is equivalent to a conventional rectangular waveguide and has a negligible leakage lossless [59, 60] is defined by

$$d > Via\,Diameter \tag{4.10}$$

and

$$\frac{d}{\lambda_c} < 0.25 \tag{4.11}$$

where d is the spacing between any two vias and λ_c is the cutoff wavelength.

Full-wave EM simulations were performed using *ANSYS HFSS* leading to the following optimal dimensions of the proposed filter as listed in Table 4.1. As depicted in Figure 4-4, slot coupling is used for the input/output feed-lines.

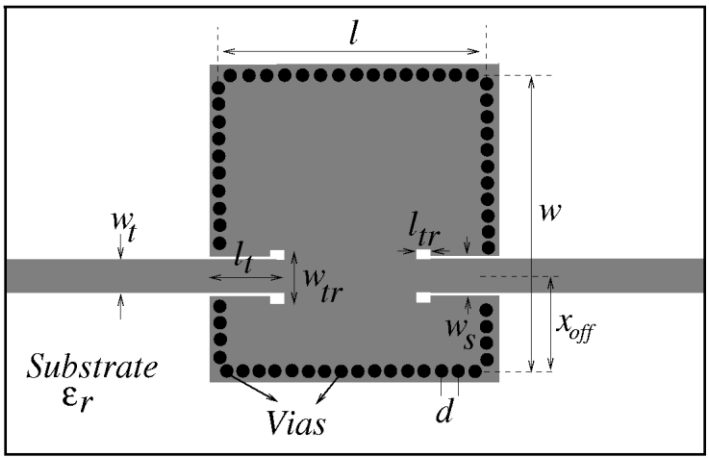

(a)

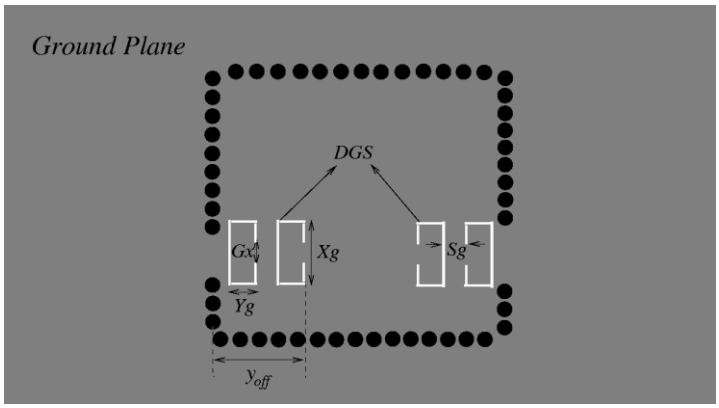

(b)

Figure 4-4: The physical structure of a single-cavity dual-mode bandpass filter with DGS: (a) top view; and (b) bottom view.

Table 4.1: Dimensions of the Single-Cavity Dual-Mode SIW Filter with Via Diameter = 0.5 mm and Spacing.

Symbol	Value (mm)
l	21.1
l_t	4.5
l_{tr}	0.6
w	19.8
w_t	1.6
w_s	1.8
w_{tr}	2.8
X_{off}	6.5
d	2
G_x	0.7
Y_g	2.1
X_g	2.7
S_g	0.3
Y_{off}	3.8

The source and load couplings as well as the inter-resonator couplings were adjusted for best electrical performance resulting in the simulated electrical performances shown in Figure 4-5(a) without DGS and Figure 4-5(b) with DGS and improved upper stopband. Both plots have a passband center frequency at 11 GHz with a transmission zero located on the passband's upper side.

A well-tuned microwave filter must have the number of dips (*i.e.* filter's poles) in the S_{11} response equal to the filter's order as in Figure 4-5. The electrical performance of the filter in Figure 4-5 shows a second order filter since two poles appear in the S_{11} response.

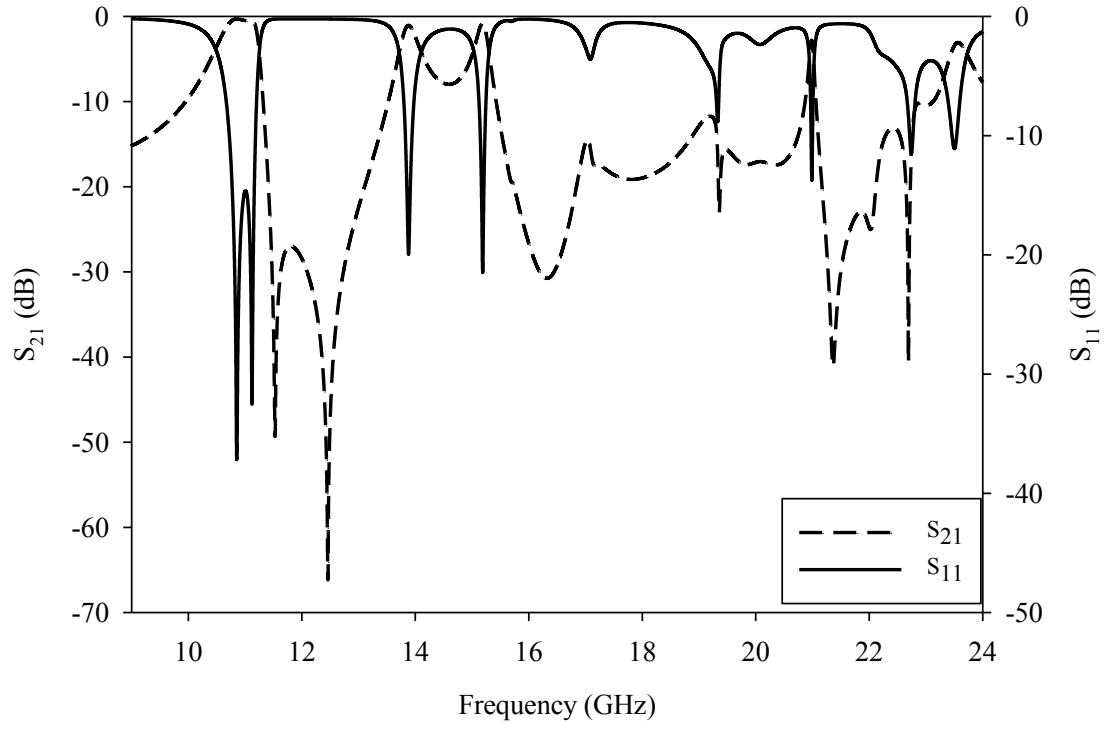

(a)

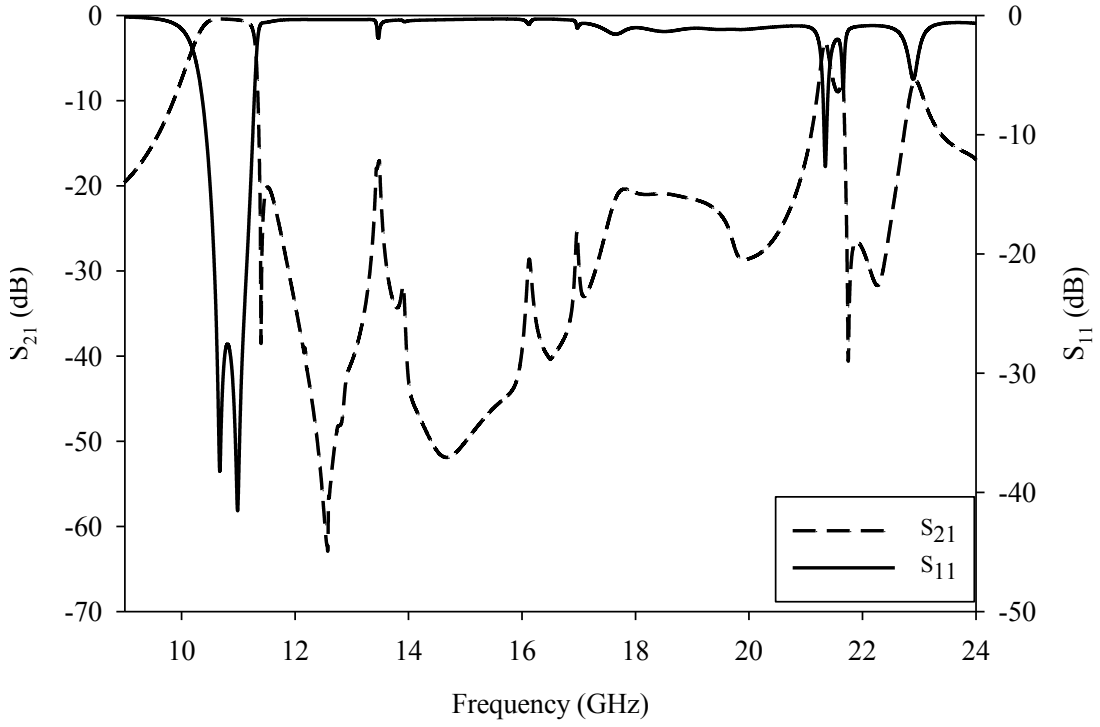

(b)

Figure 4-5: Simulated frequency response of the single-cavity SIW bandpass filter: (a) without DGS; and (b) with DGS.

4.1.2 Double-Cavity Dual-Mode SIW Filter

An attempt to improve the skirt selectivity led to the implementation of a double-cavity dual-mode SIW filter with DGS whose configuration is shown in Figure 4-6.

Full-wave EM simulations were performed leading to the following optimal dimensions as listed in Table 4.2.

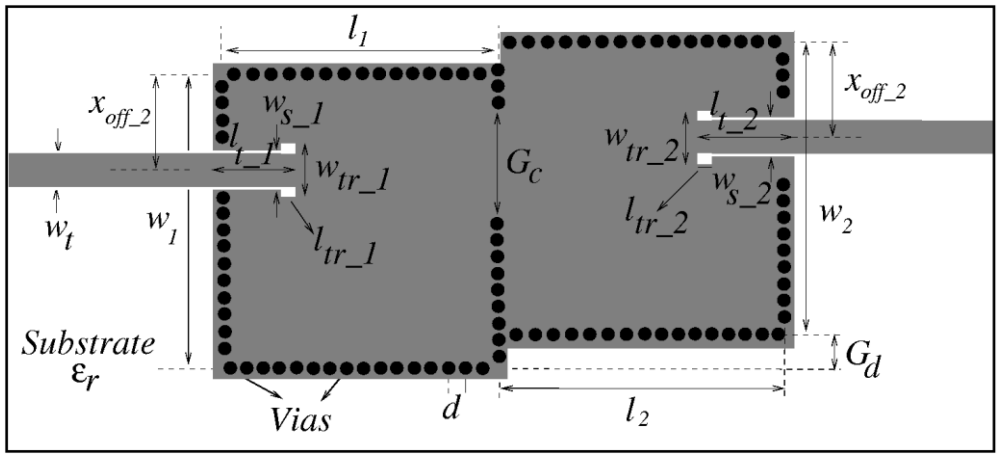

(a)

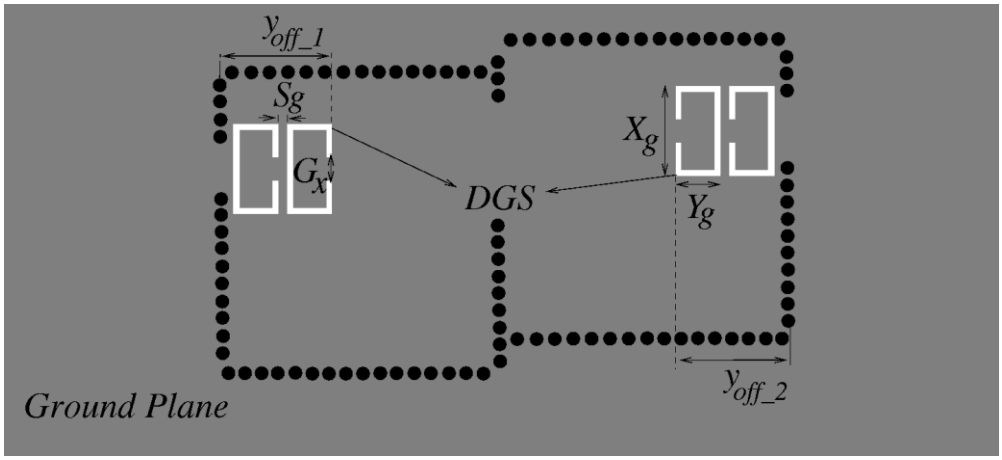

(b)

Figure 4-6: The physical structure of a double-cavity dual-mode SIW bandpass filter with DGS: (a) top view; and (b) bottom view.

Table 4.2: Dimensions of the Double-Cavity Dual-Mode SIW Filter with Via Diameter = 0.5 mm and Spacing.

Symbol	Value (mm)	Symbol	Value (mm)
l_1	20.5	$l_{tr\ 2}$	1.2
l_2	19.8	$w_{tr\ 1}$	3.7
w_1	20.3	$w_{tr\ 2}$	3.7
w_2	22.25	$x_{off\ 1}$	5.9
w_t	1.6	$x_{off\ 2}$	7.9
G_c	5.6	d	2
G_d	0.7	G_x	0.7
$w_{s\ 1}$	1.8	Y_g	2.1
$w_{s\ 1}$	1.9	X_g	2.7
$l_{t\ 1}$	4.7	S_g	0.3
$l_{t\ 1}$	5.7	$Y_{off\ 1}$	3.8
$l_{tr\ 1}$	1.2	$Y_{off\ 2}$	3.8

Based on the successful implementation of the single-cavity filter, a double-cavity filter was then simulated following similar steps as seen in Figure 4-7. The simulated performance shown in Figure 4-7(b) clearly exhibits an improved upper stopband performance and further proves the validity of the proposed approach. Both plots have passband center frequency at 11 GHz with two transmission zeros located on the passband's lower and upper side.

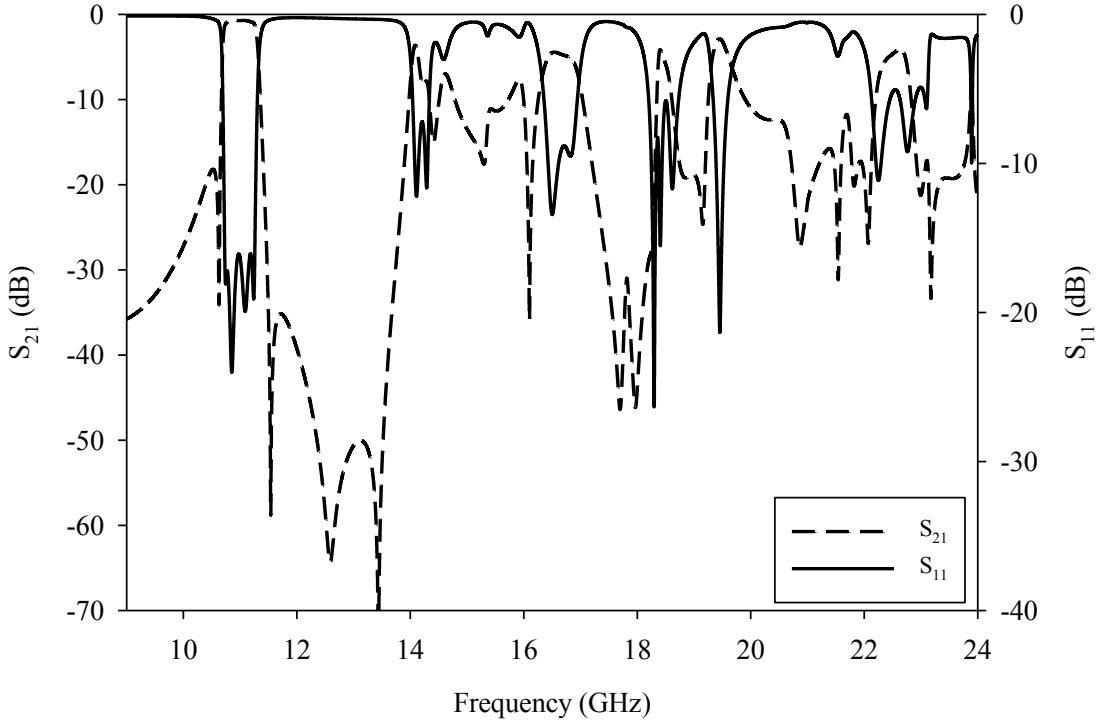

(a)

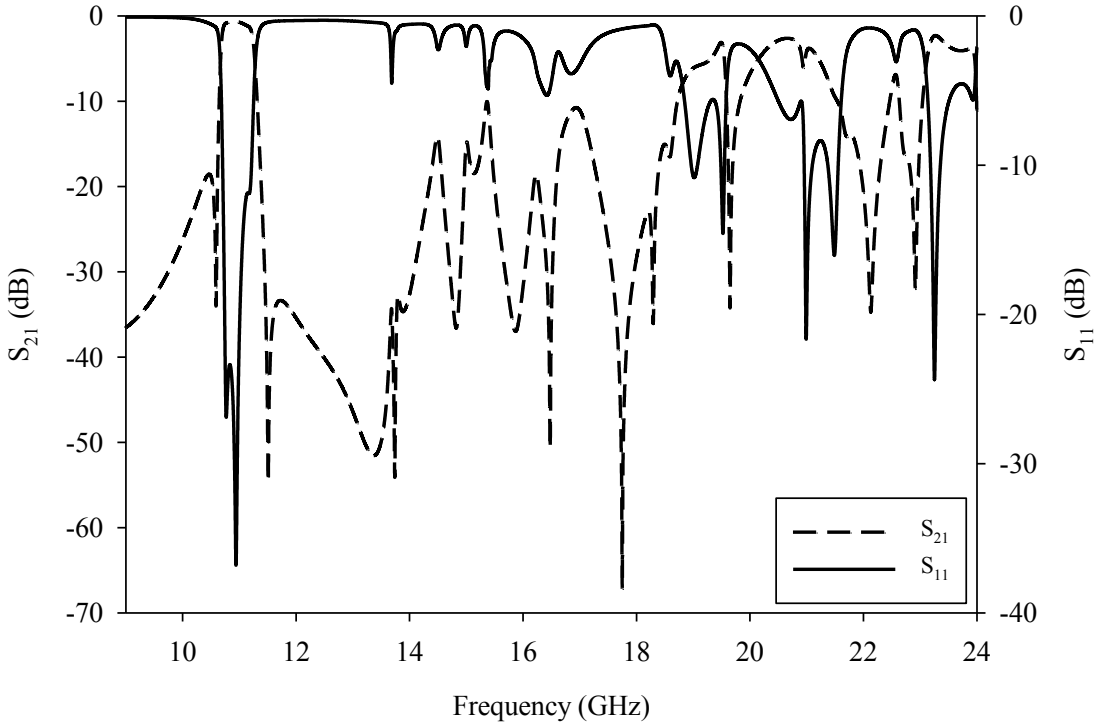

(b)

Figure 4-7: Simulated frequency response of the double-cavity SIW bandpass filter: (a) without DGS; and (b) with DGS.

4.2 Dual-Band Dual-Mode SIW Filters

Figure 4-8 depicts the coupling scheme of the dual-mode SIW filter which consists of two orthogonal resonant modes (TE_{102} and TE_{201}) in an SIW cavity (node 1 and node 2). The electric field distributions of the orthogonal modes in a cavity are shown in Figure 4-9.

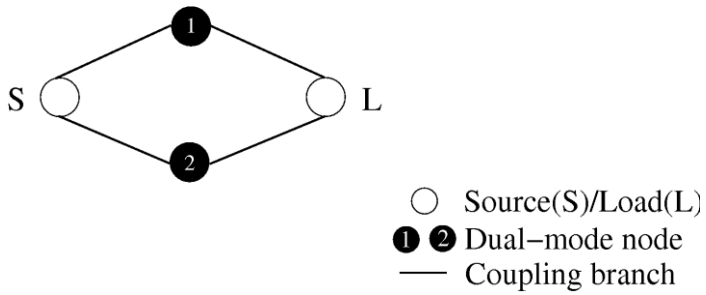

Figure 4-8: Coupling topology of a dual-mode SIW cavity.

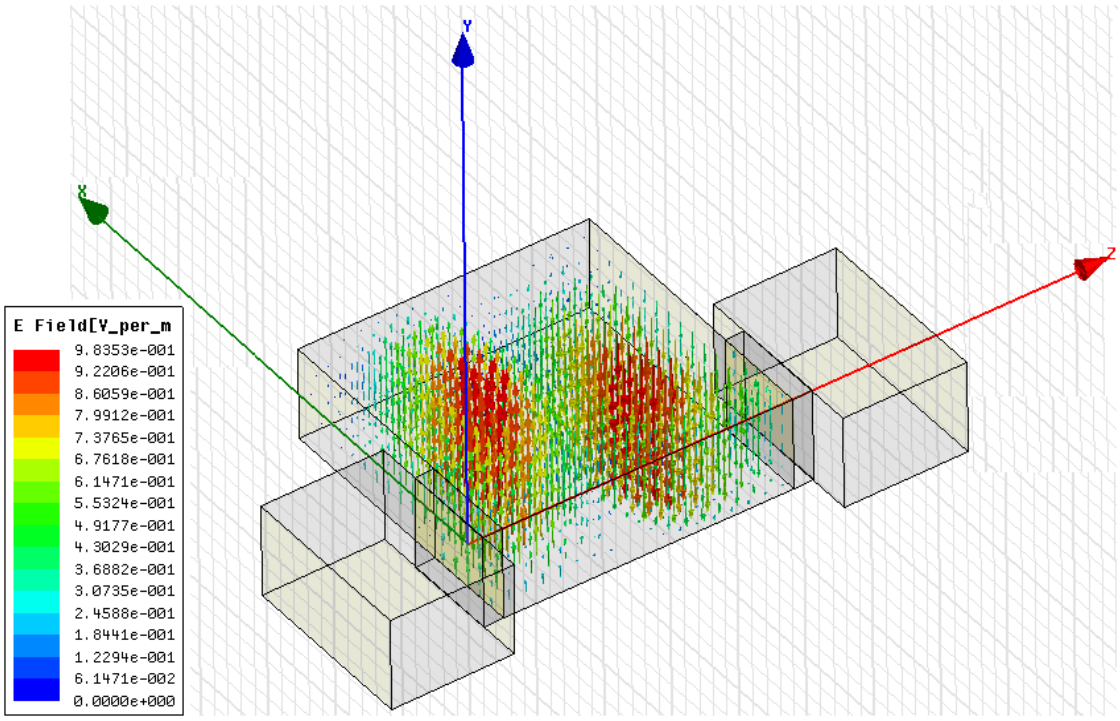

(a)

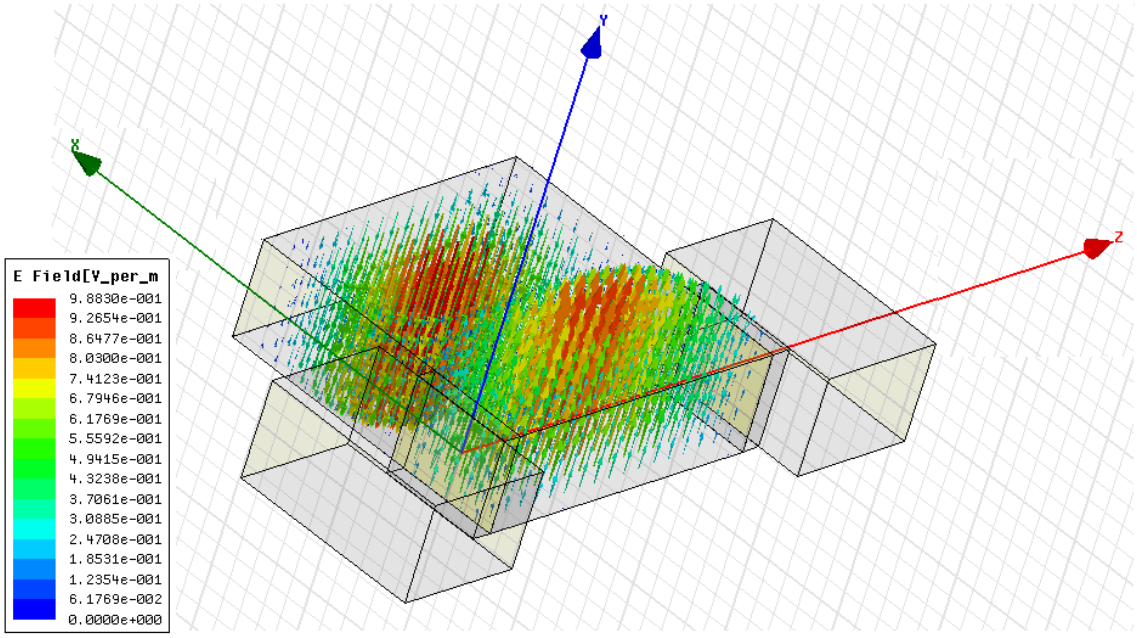

(b)

Figure 4-9: (a) Electric field distribution of TE_{102} mode and (b) Electric field distribution of TE_{201} mode.

4.2.1 Three-Cavity Bandpass Dual-Mode SIW Filter

Figure 4-10(a) illustrates the physical structure of a three-cavity bandpass dual-mode SIW filter with 50 Ω Microstrip feed-lines. As depicted, a linear taper for transition between the 50 Ω Microstrip line and the SIW is used for the input/output feed-lines [40]. The structure is supported by a 0.508 mm thick Rogers RT/duroid 5880 substrate with a dielectric constant of 2.2 and a loss tangent of 0.0009.

Full-wave EM simulations were performed using *ANSYS HFSS* leading to the optimal dimensions (Table 4.3) of the dual-mode bandpass filter. The source and load couplings, as well as the inter-resonator couplings, were adjusted to achieve the best electrical performance resulting in the simulated electrical performances shown in Figure 4-10(b). The evaluated response has a passband center frequency at 11 GHz with a 10%

fractional bandwidth. Fractional bandwidth is the ratio between the absolute bandwidth to the center frequency and is given by

$$FractionalBandwidth(\%) = \frac{f_H - f_L}{f_C} \times 100\% \tag{4.12}$$

where f_H is the upper cutoff frequency, f_L is the lower cutoff frequency, and f_C is the passband center frequency.

Three transmission zeros are introduced. Two transmission zeros are located on the passband's lower side at 9.9 GHz and 10.2 GHz, while the third transmission zero is located on the upper side at 11.8 GHz.

Each dual-mode cavity is responsible for generating two transmission poles and one transmission zero due to the different phase shifting between the two orthogonal modes in the cavity.

Note that the position of the transmission zeros can be moved to the passband's left- or right-side by changing the cavity's length-to-width ratio [57].

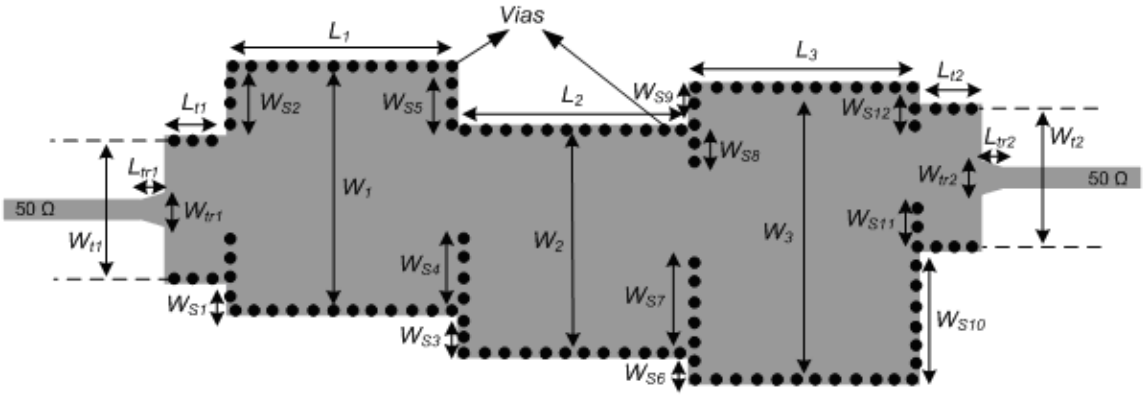

(a)

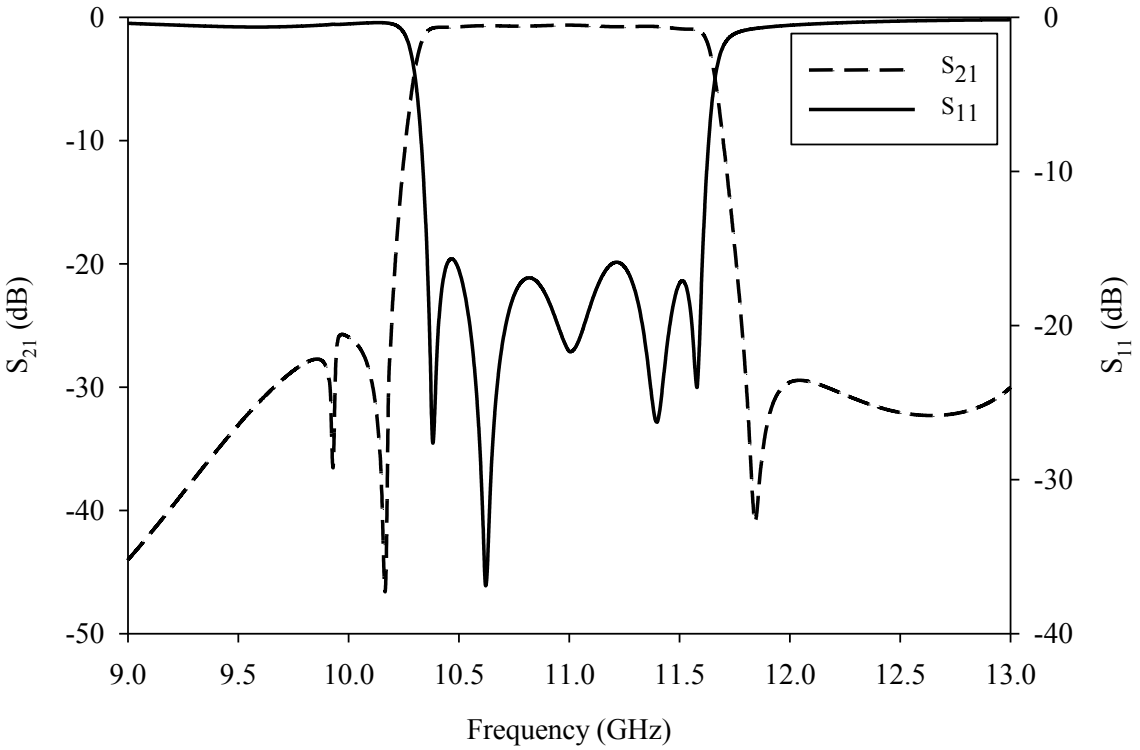

(b)

Figure 4-10: (a) Top view configuration of the three-cavity bandpass dual-mode SIW filter and (b) its simulated frequency characteristics.

Table 4.3: Dimensions of the Bandpass Dual-Mode SIW Filter with Via Diameter = 0.5 mm and Spacing between Adjacent Vias = 1.5 mm.

Symbol	Value (mm)	Symbol	Value (mm)
L_1	17.5	W_{tr2}	1.8
L_2	18	W_{S1}	3.7
L_3	18.6	W_{S2}	8.4
L_{t1}	6	W_{S3}	1.7
L_{tr1}	2.8	W_{S4}	8.6
L_{t2}	6	W_{S5}	8
L_{tr2}	2.8	W_{S6}	0.75
W_1	25.2	W_{S7}	10
W_2	18.8	W_{S8}	3.6
W_3	22.6	W_{S9}	2.7
W_{t1}	13.6	W_{S10}	8.9
W_{tr1}	1.8	W_{S11}	3
W_{t2}	13.2	W_{S12}	2.8

4.2.2 Three-Cavity Dual-Band Dual-Mode SIW Filter

Based on the successful implementation of the three-cavity bandpass filter, a three-cavity dual-band filter was implemented following similar steps. Here, the position of the transmission zero responsible for creating the dual-band characteristics has been adjusted by changing the offset in the input and the output couplings.

The physical structure of the proposed dual-band dual-mode SIW filter is shown in Figure 4-11(a). Full-wave EM simulations were performed leading to the optimal dimensions of the proposed filter as in Table 4.4.

The simulated frequency performance shown in Figure 4-11(b) clearly exhibits dual-band frequency characteristics and further establishes the validity of the proposed approach. The dual-band frequency response has a lower passband center frequency at 10.6 GHz with a 4% fractional bandwidth and an upper passband center frequency at 11.4 GHz with a 5% fractional bandwidth. Two symmetric transmission zeros are located on the passband's lower and upper sides, and the transmission zero that was located at 9.9 GHz in the previous design is now located at 11 GHz.

It is worth mentioning that the level and bandwidth of the in-band notch (*i.e.* transmission zero at 11 GHz) could be further improved by increasing the filter's order until it provides the desired isolation between the two adjacent bands.

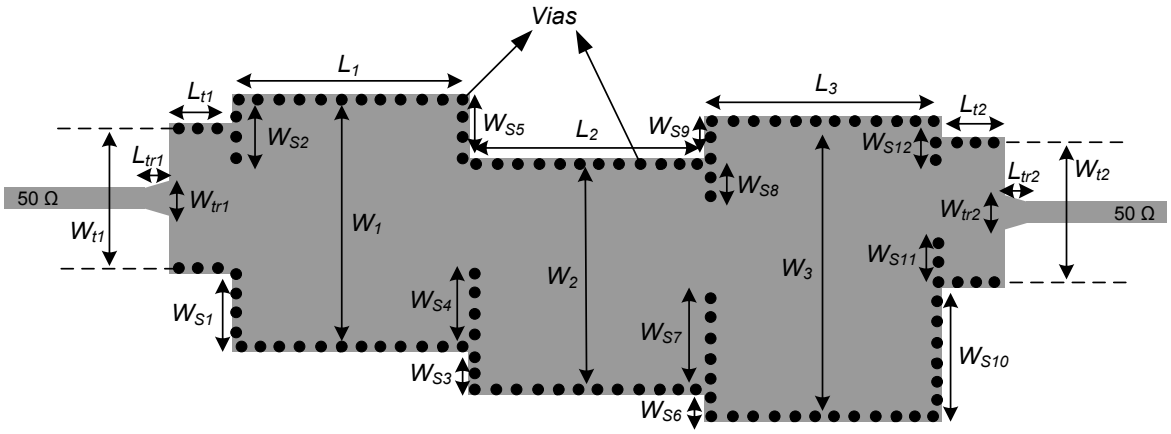

(a)

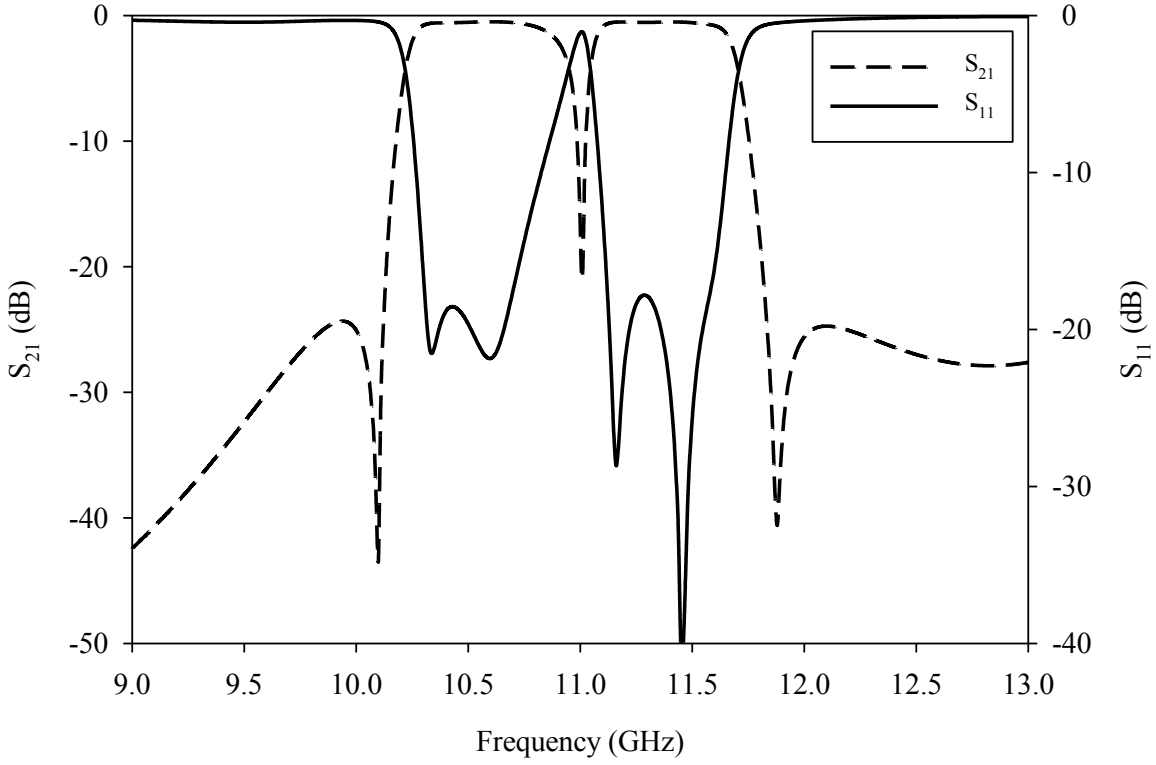

(b)

Figure 4-11: (a) Top view configuration of the proposed three-cavity dual-band dual-mode SIW filter and (b) its simulated frequency characteristics.

Table 4.4: Dimensions of the Proposed Dual-Band Dual-Mode SIW Filter with Via Diameter = 0.5 mm and Spacing between Adjacent Vias = 1.5 mm.

Symbol	Value (mm)	Symbol	Value (mm)
L_1	17.5	W_{tr2}	1.8
L_2	19.7	W_{S1}	4.8
L_3	17.9	W_{S2}	6.9
L_{t1}	5.75	W_{S3}	2.5
L_{tr1}	2.8	W_{S4}	8.1
L_{t2}	6	W_{S5}	4.8
L_{tr2}	2.8	W_{S6}	0.9
W_1	21.4	W_{S7}	8.6
W_2	19	W_{S8}	2.8
W_3	23.4	W_{S9}	2.9
W_{t1}	12.8	W_{S10}	8.6
W_{tr1}	1.8	W_{S11}	2.9
W_{t2}	12.8	W_{S12}	2.35

4.3 Conclusions

SIW dual-mode bandpass filters with an improved upper stopband performance are demonstrated. The filters are comprised of three SIW cavities with pairs of orthogonal modes while the inter-resonator couplings are realized by using simple inductive discontinuities. A lowpass cleanup filter generated using DGS pattern etched on the ground plane within the cavity area and the proposed filters show an excellent upper stopband improvement while the filter's compact size is maintained.

An SIW filter with dual-mode dual-band frequency characteristics and symmetric transmission zeros was successfully realized. A dual-band response can be easily achieved by moving one of the dual-mode bandpass filter transmission zeros toward its passband. SIW technology is used for better device and system integration.

Chapter 5

Reconfigurable Bandpass SIW Filters

Reconfigurable bandpass filters have become a crucial component in emerging broadband microwave and millimeter-wave communication systems, especially in front-end receivers. Recently, to meet the stringent requirements of modern multi-band systems, reconfigurable filters with low insertion loss and compact size have become desirable. This has led to the development of sophisticated implementations of tunable cavity resonators based filters [61-63]. Therefore, tunable SIW filters using simple tuning techniques are highly desirable. In literature, tunable microwave circuits fall into the following types: mechanically [64], magnetically [65], ferroelectrically [66], electrically [67], and optically [68] tunable circuits. In this work, ferrite material is employed in SIW filters, which provides the possibility of new and simple tuning methods. Design principle of the ferrite SIW filter is based upon the synthesis approach of microwave circulators/isolators. First publication about microwave ferrite devices using SIW technology such as circulators and isolators was presented in 2004 by D'Orazio et al [69]. For emerging high volume applications, related efforts focused on the integration of SIW circulators [70], advance frequency characteristics [71], and notch filter incorporating junction circulators [72]. However, none has reported the use of circulators as tunable

bandpass filters. In many cases, this is an advantageous to use one front-end component which has two functions (*i.e.* circulation and filtering). Therefore, the objective of this chapter is to demonstrate that the design principle of waveguide ferrite circulators and isolators can be utilized for realizing a tunable filter response in a planar realization.

Section 5.1 investigates the implementation of single- and double-circulator tunable SIW filters as well as their simulated results, while conclusions are given in Section 5.2.

5.1 Filter Implementation

The configuration of circulators and isolators is essentially a multi-port network. Utilizing the simple structure of a three-port symmetric (*i.e.* all the port separation angles are equal to 120^{o}) waveguide circulator with one port terminated by its matched load (*i.e.* 50 Ω load) leads to the realization of an isolator or a two-port circulator which performs the same function as a section of transmission line. Moreover, ferrite resonators with any threefold symmetry shapes could be used (*i.e.* disk or triangle shape) [63, 74]. However, in this work, TT2-125 [75] ferrite disk made of nickel (Ni) was selected, which has better parameter flexibility. Ferrite disk can be designed to fall under one of the following geometries [76] as shown in Figure 5-1. Figure 5-1(a) depicts a half-wavelength long ferrite disk open-circuited at both ends and coupled in the middle of a waveguide junction. Figure 5-1(b) shows two quarter-wavelength ferrite disks, while Figure 5-1(c) shows a single quarter-wavelength ferrite disk. It is worth mentioning that the analysis and performance of all three geometries are similar, but the geometry in Figure 5-1(b) has

better parameter flexibility and enables the realization of a symmetrical structure which is preferred for efficient electromagnetic simulations and modeling.

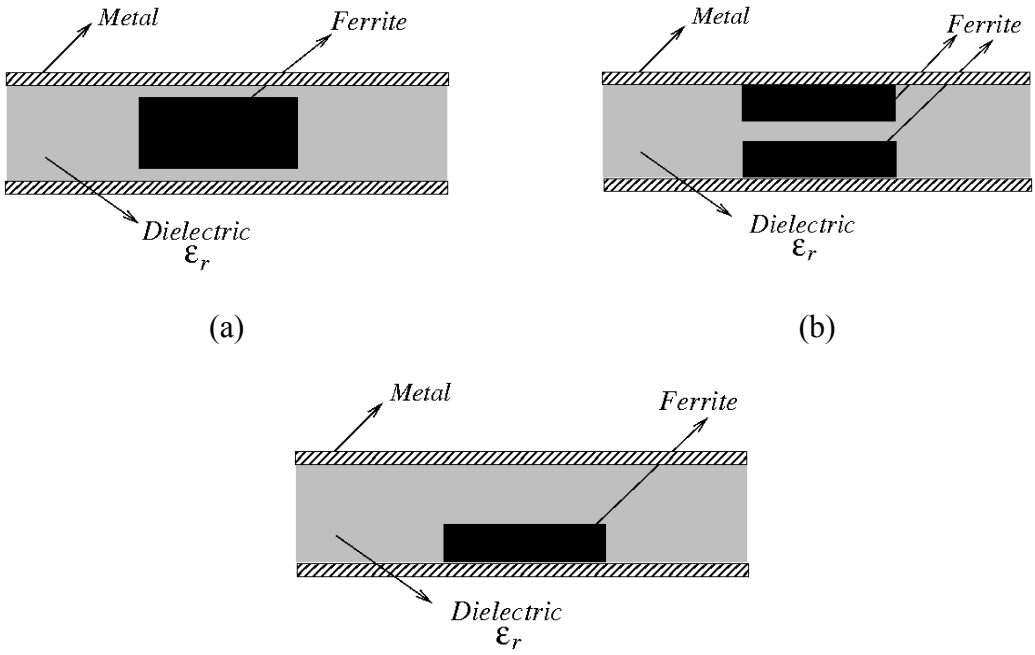

Figure 5-1: Side view of three different ferrite disk geometries.

Here, the ferrite magnet operates above-resonance in the saturation mode, since much higher magnetic fields are not a concern. To avoid low field loss as that for resonance and below resonance [76], the saturation magnetization should be selected such that the ferrite is fully biased. To meet this condition, we need

$$4\pi M_S < \frac{\omega}{\gamma_{eff}} - H_a \tag{5.1}$$

and

$$\gamma_{eff} = \frac{\omega}{H} \tag{5.2}$$

where $4\pi M_S$ is the ferrite saturation magnetization, ω is the RF radian frequency, γ_{eff} is the effective gyromagnetic ratio, H_a is the anisotropy field associated with the

particular material selected, and H is the applied magnetic field. Two examples will now be illustrated.

5.1.1 Single-Circulator Tunable Bandpass Filter

Figure 5-2 illustrates the physical structure of a single-circulator tunable bandpass filter. The structure is supported by a 1.575 mm thick FR4 substrate with a dielectric constant of 4.4 and a loss tangent of 0.02. Full-wave EM simulations were performed with the aid of *ANSYS HFSS* leading to the following optimal dimensions of the proposed filter as listed in Table 5.1. Here, HFSS based on FEM method is preferred for the closed space problems such as cavities because it does not have high performance absorbing boundary in comparison to other commercial EM solvers based on the finite difference time domain (FDTD) methods.

Table 5.1: Dimensions of the Proposed Single-Circulator Tunable Filter with Via Diameter = 0.5 mm and Spacing between Adjacent Vias = 1.5 mm.

Symbol	Value (mm)
l_1	6.98
l_2	6.98
l_3	8.51
d	1
D	13.1
h_f	0.3
W_1	11.68
W_2	11.68
W_3	11.68

As depicted in Figure 5-2, two ferrite disks are coupled in the middle of the waveguide junction. Figure 5-3 shows the frequency performance of the configuration in Figure 5-2 with the minimum internal bias (*i.e.* 2100 Gauss) required for saturating the

ferrite magnet. The plot has a passband center frequency at 10.45 GHz with an insertion loss of 1 dB.

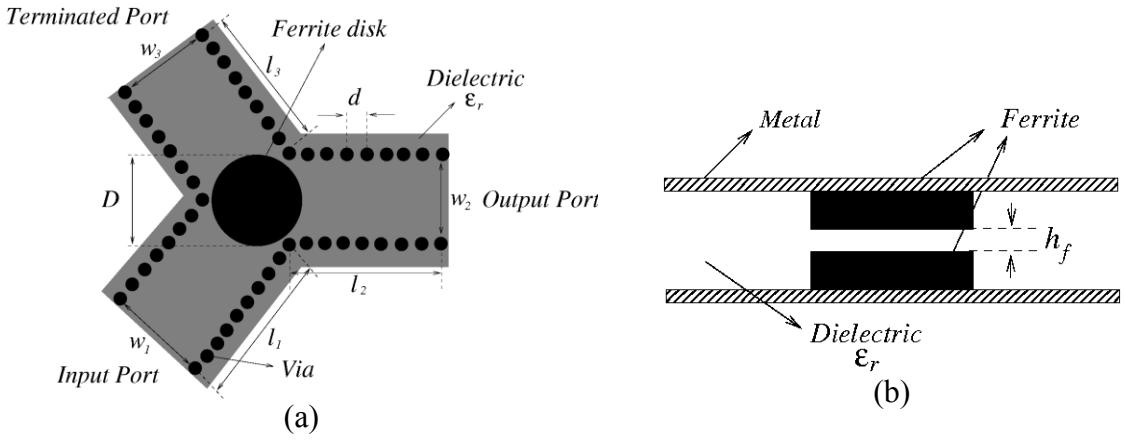

Figure 5-2: The physical structure of a single-circulator tunable bandpass filter: (a) top view; and (b) side view.

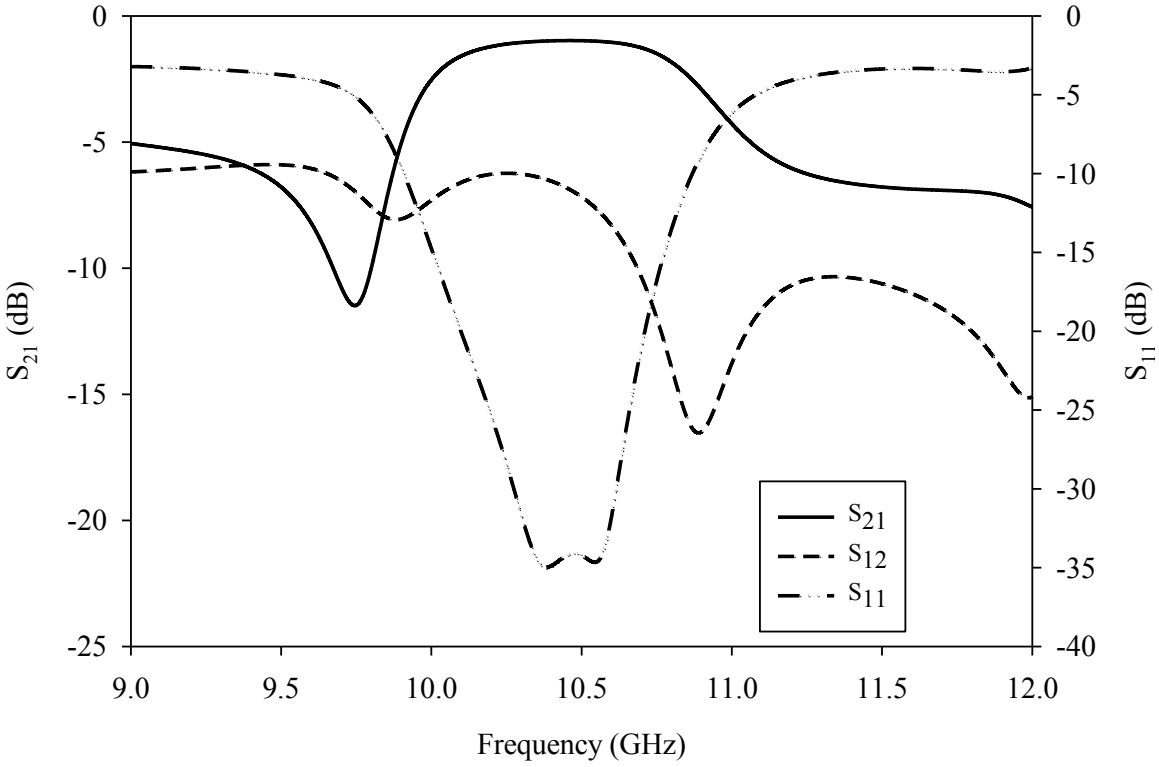

Figure 5-3: The simulated frequency response of a single-circulator bandpass filter.

Figure 5-4 shows that for a given passband center frequency, increasing the diameter of the ferrite disk leads to a decrease in the bandwidth. Figure 5-5 illustrates the simulated S-parameter results when tuned from 10.45 to 11.3 GHz by vertically applying different internal dc-magnetic bias intensities, while the insertion loss and the fractional bandwidth variation are given in Figure 5-6.

It is also found that the bandwidth has experienced certain variation as the passband's center frequency is tuned.

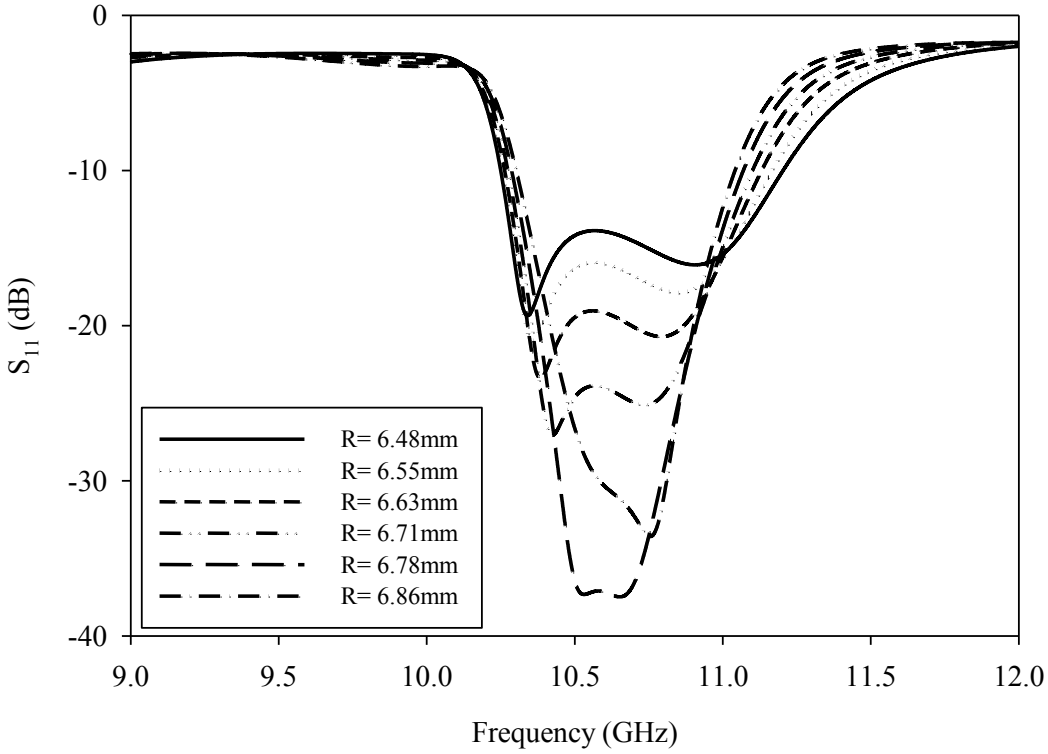

Figure 5-4: The simulated frequency characteristics of a single-circulator filter with bandwidth control.

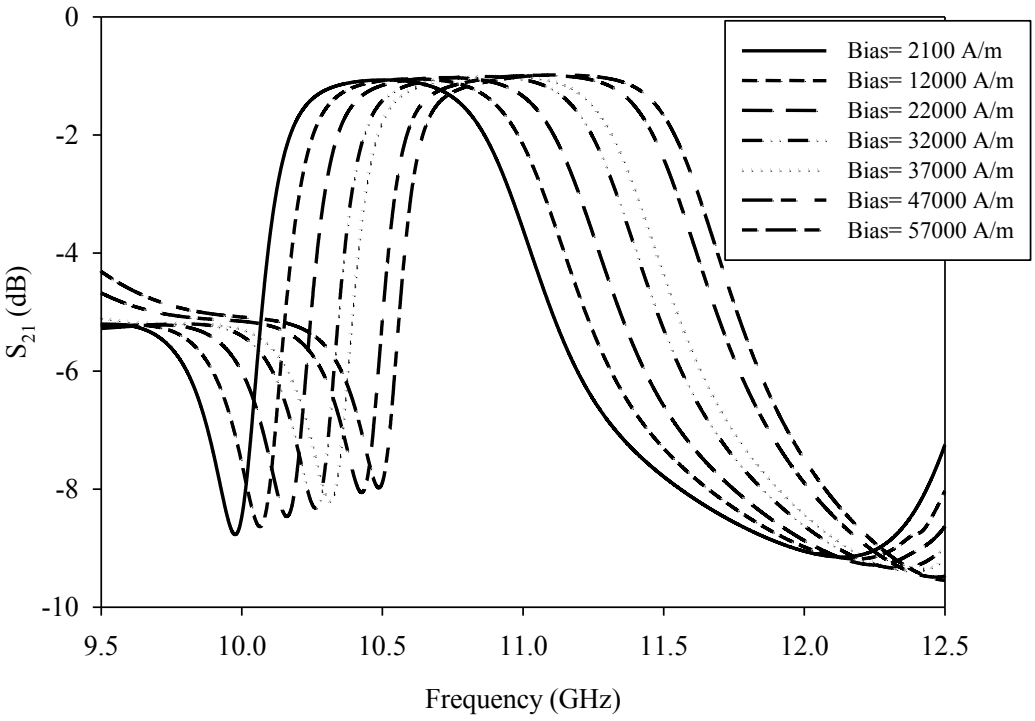

(a)

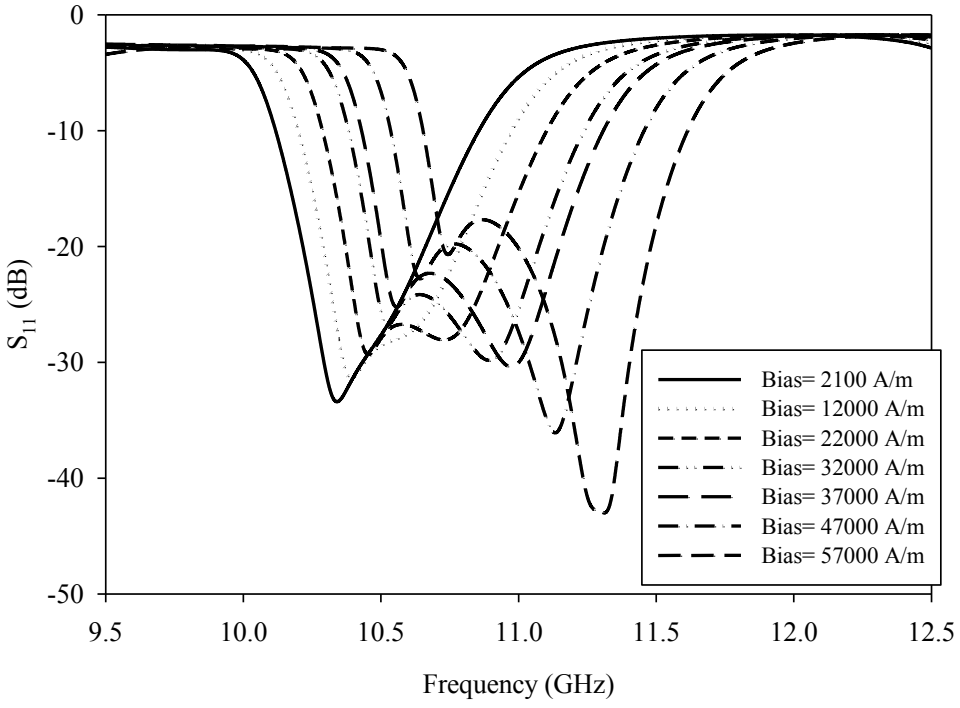

(b)

Figure 5-5: Variation of the passband center frequency with the applied magnetization field of the single–circulator tunable bandpass filter: (a) S_{21} response; and (b) S_{11} response.

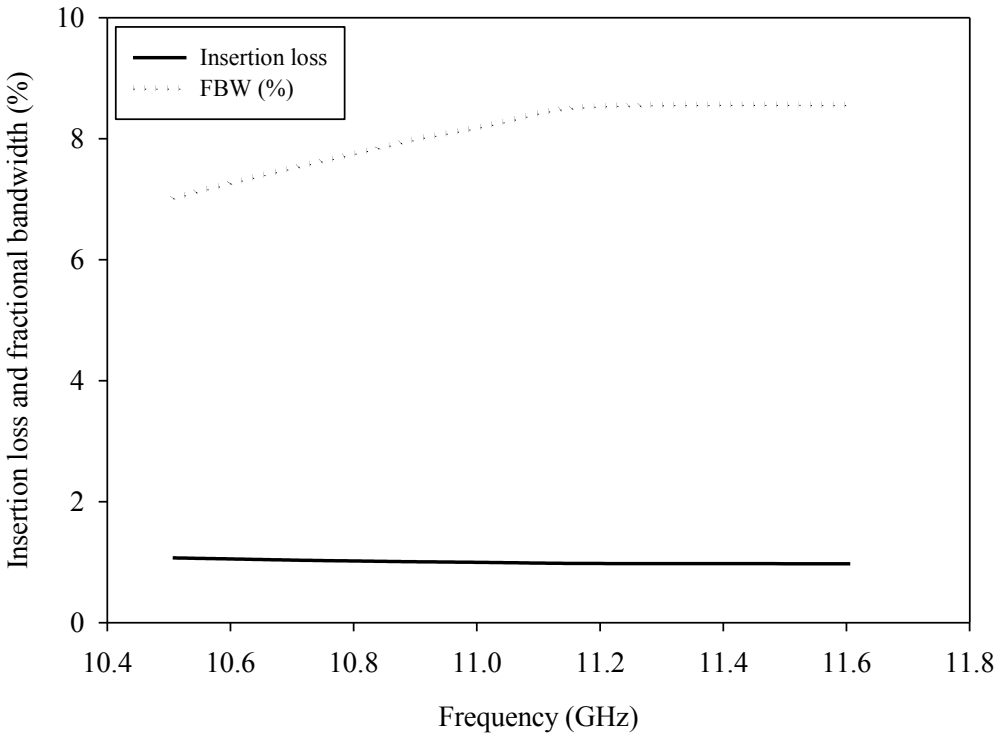

Figure 5-6: Simulated insertion loss and fractional bandwidth.

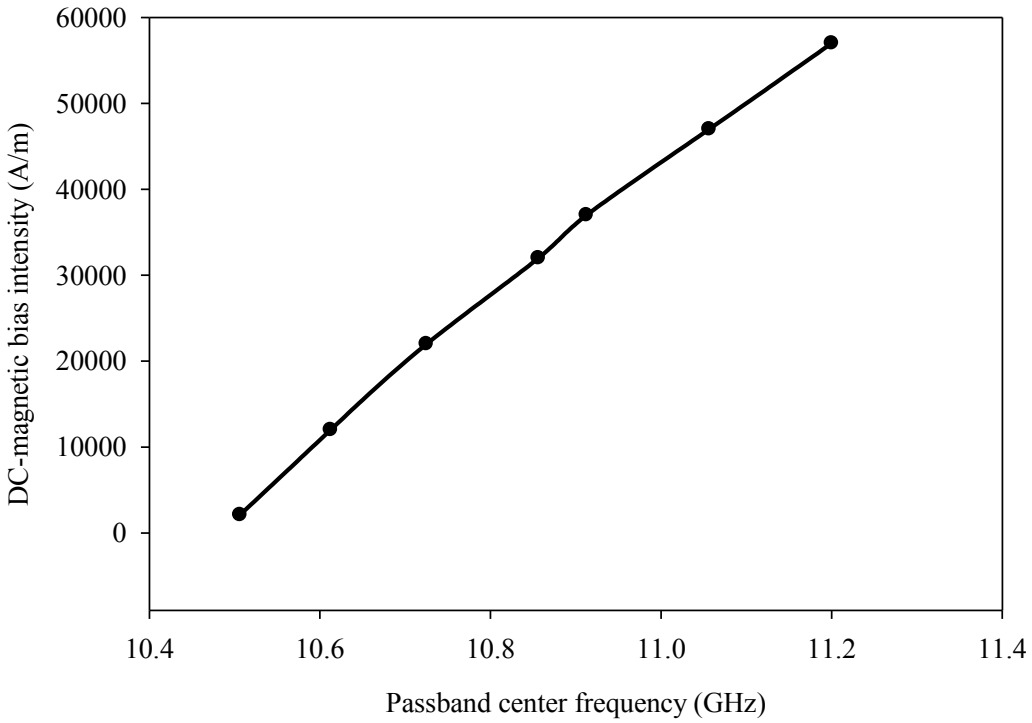

Figure 5-7: DC-magnetic bias intensity versus passband center frequency.

Figure 5-7 shows the linear relationship between the applied magnetic field and the tuning range of the passband center frequency. This is advantageous since a specific frequency characteristic can be easily anticipated.

5.1.2 Double-Circulator Tunable Bandpass Filter

After the successful implementation of the single-circulator filter, a double-circulator filter was implemented. The physical structure of the double-circulator bandpass filter (Figure 5-8) was simulated using *ANSYS HFSS* following the same guidelines presented in the single-circulator filter leading to the following optimized dimensions presented in Table 5.2.

Table 5.2: Dimensions of the Proposed Double-Circulator Tunable Filter with ferrite-gap = 0.1 mm, Via Diameter = 0.5 mm, and Spacing between Adjacent Vias = 1.5 mm.

Symbol	Value (mm)
l_1	5.1
l_2	12.45
l_3	5.8
l_4	5.1
l_5	5.8
d	1
D_1	13.36
D_2	13.36
W_1	11.68
W_2	10.9
W_3	11.68
W_4	11.68
W_5	11.68

This was mainly to prove the validity of the underlying design principle and to improve the selectivity of the proposed filter. Figure 5-9 shows the simulated S-

parameter frequency performance that is tuned from 10.45 to 11.3 GHz. As depicted, Figure 5-9(a) clearly exhibits an improved stopband attenuation compared to the results in Figure 5-5(a). A good return loss (S_{11}) within the passband bandwidth is achieved as shown in Figure 5-9(b).

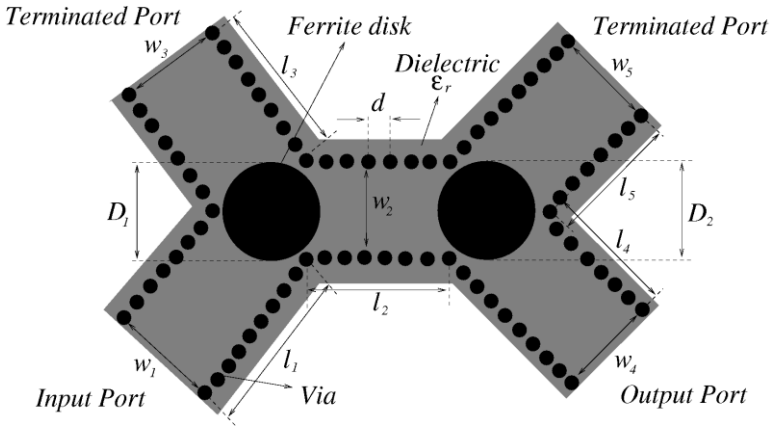

Figure 5-8: Top view of the physical structure of a double-circulator tunable bandpass filter.

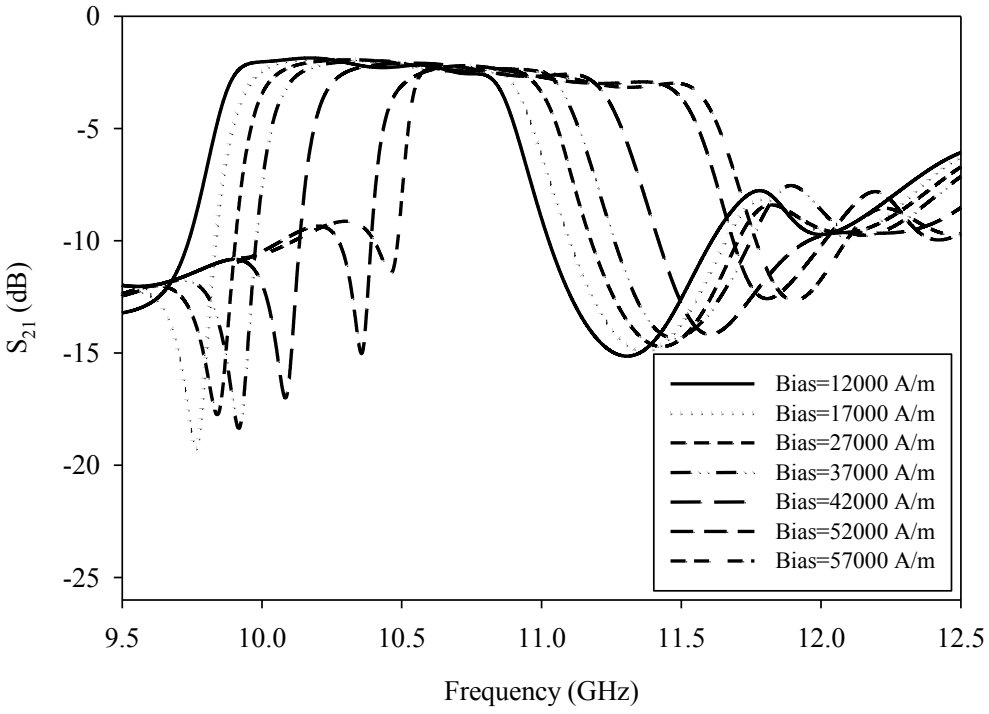

(a)

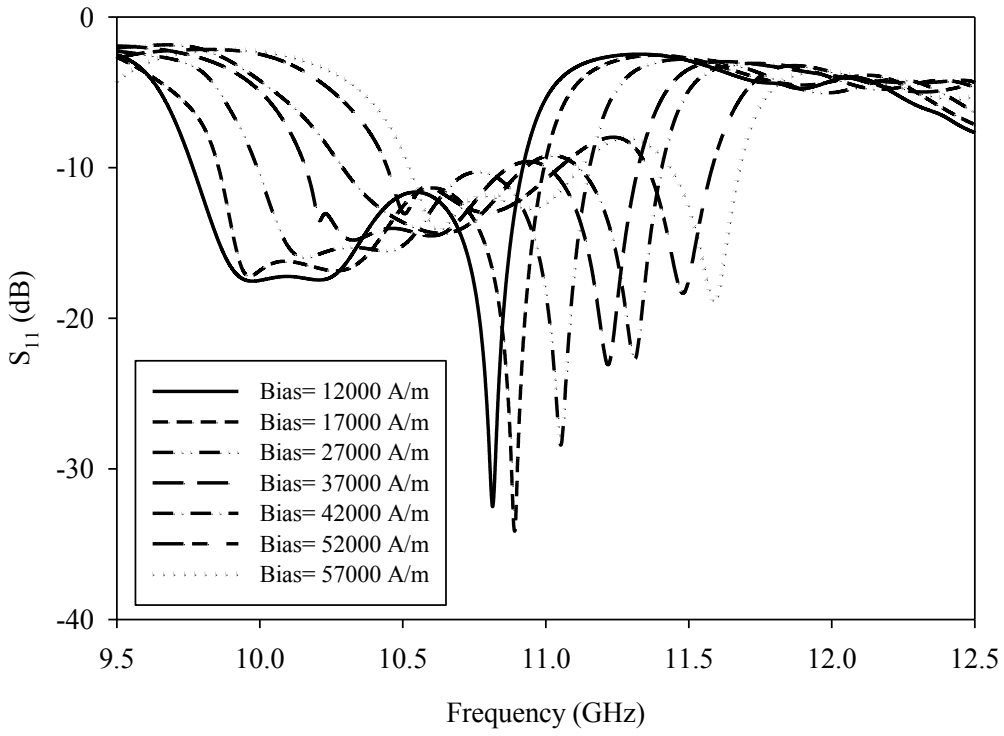

(b)

Figure 5-9: Variation of the passband center frequency with the applied magnetization field of the double–circulator tunable bandpass filter: (a) S_{21} response; and (b) S_{11} response.

5.2 Conclusions

This work introduced a new class of SIW bandpass filters with robust and simple tuning ability. The passband of the proposed filters can be reconfigured by adjusting the dc-magnetic bias applied to a pair of ferrite disks located at the edge of an SIW cavity. The applied magnetic field dynamically controls the passband center frequency of the SIW filter, while dramatically reducing the complexity compared to traditional electronic control methodologies. The proposed filters maintain nearly constant bandwidth and passband shape as the filter is tuned. The presented examples show single- and double-

circulator filters, however, the same principle may be applied for more than two circulators forming a filter.

It is foreseen that this type of filter will find numerous applications in advanced RF front-ends where simple and stable tunability is of the essence.

Chapter 6

In-line Evanescent-Mode SIW Bandpass Filter with N-1 Transmission Zeros

In 1950 Jaynes [77] and Edson [78] proposed that waveguide resonators operating at cutoff may be used in filter design. These filters are called evanescent-mode filters. Compact, low-loss filters are commonly designed utilizing the evanescent-mode response in situations where size and weight restrictions need to be met without sacrificing a filter's performance as in satellite communications or transponders. The literature holds many publications discussing several design approaches regarding the design of evanescent-mode waveguide filters [79-85]. The basic device consists of a section of rectangular waveguide with a number of spaced discontinuities distributed across the guide length. The novelty in the proposed design lies using the SIW technology in implementing an in-line (*i.e.* input and output ports are located across the filter length) bandpass filter to operate below the cutoff frequency (*i.e.* evanescent-mode), thus compact size planar filter is realized with capability of realizing N-1 transmission zeros where N is the filter's order. In-line structures are usually preferable, especially in integrating multiple components.

There are two major purposes for using an evanescent-mode in this design. The first purpose is for realizing compact filters. Operating in evanescent-mode makes the

realization of SIW filters which operate at low resonant frequencies more reasonable, since, as presented in equation (4.1), the cutoff characteristics in a conventional waveguide structure depend on the cross-sectional dimensions of the waveguide cavity. Here, evanescent-mode filters have a smaller cross-section than rectangular waveguide filters, and it is worth mentioning that as we move down in frequency, the waveguide dimensions increase and vice-versa. The second purpose is that SIW filters exhibit a poor stopband performance as demonstrated in equation (4.6). Thus, working in evanescent-mode far below the cutoff frequency leads to an improvement in the upper stopband performance.

The next section demonstrates the implementation of 3rd order evanescent-mode SIW bandpass filters with and without transmission zeros.

6.1 Filter Implementation

6.1.1 3rd Order Evanescent-Mode Bandpass Filter

The design concept is easily understood upon examining the 3rd order evanescent-mode circuit prototype shown in Figure 6-1. The circuit is comprised of three bandpass resonators (*i.e.* (L_1,C_1) and (L_2,C_2)). As depicted, the inter-resonator couplings are inductive couplings (*i.e.* L_{12} and L_{21}).

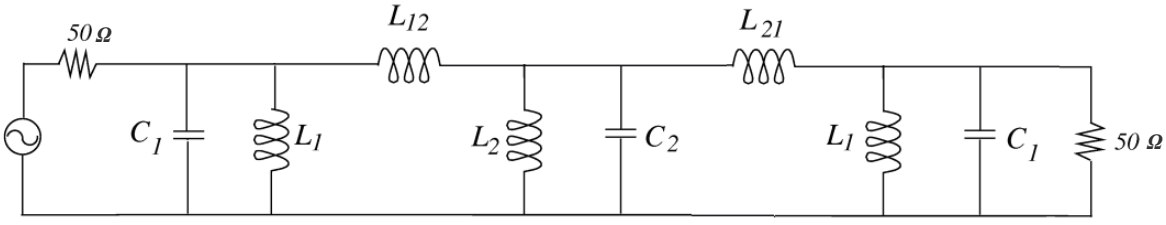

Figure 6-1: 3rd order circuit prototype of an evanescent-mode bandpass filter in a 50 Ω system.

A symmetrical implementation for the evanescent-mode SIW filter of Figure 6-1 is shown in Figure 6-2, which depicts two substrate layers; a main substrate layer with a relative dielectric constant of 3.55, a loss tangent of 0.0027 with 1.524 mm thickness and a thin dielectric layer (*i.e.* lid layer) positioned above the main layer with a relative dielectric constant of 3.55, a loss tangent of 0.0027 with 0.2032 mm thickness. The lid layer works as distributed capacitors for the three resonators on the main layer and also is one of the four waveguide cavity walls. The SIW section shown in Figure 6-2 is an evanescent-mode guide which is an inductive element. In evanescent-mode, the transfer of power below the cutoff frequency is a result of the multiple reflections between the waveguide section and its own shunt capacitive obstacles, which are represented by Combline resonators [1, 86, 87]. Both shunt capacitive and inductive elements are needed to construct the evanescent-mode bandpass filter characteristics. In Figure 6-2, each Combline resonator has a length of 1.524 mm (*i.e.* main substrate thickness) and is mounted with an equally distributed capacitance hat. The illustrated filter has a symmetrical structure with an impedance difference between the middle and both of the I/O Comblines. These impedance differences are accomplished by varying the radius of the circular vias (R_1, R_2) as shown in Figure 6-2. Structure dimensions are listed in Table 6.1.

Equation 6.1 is a parallel plate capacitor formula which represents the shunt capacitors (C_1 and C_2) in Figure 6-1, where in our design d is the lid layer thickness, A is the circular area mounted above the Comblines, and ε is the dielectric permittivity.

$$C = \frac{\varepsilon A}{d} \tag{6.1}$$

It is worth mentioning that as the capacitance value decreases, the passband resonances shift up in frequency and vice-versa.

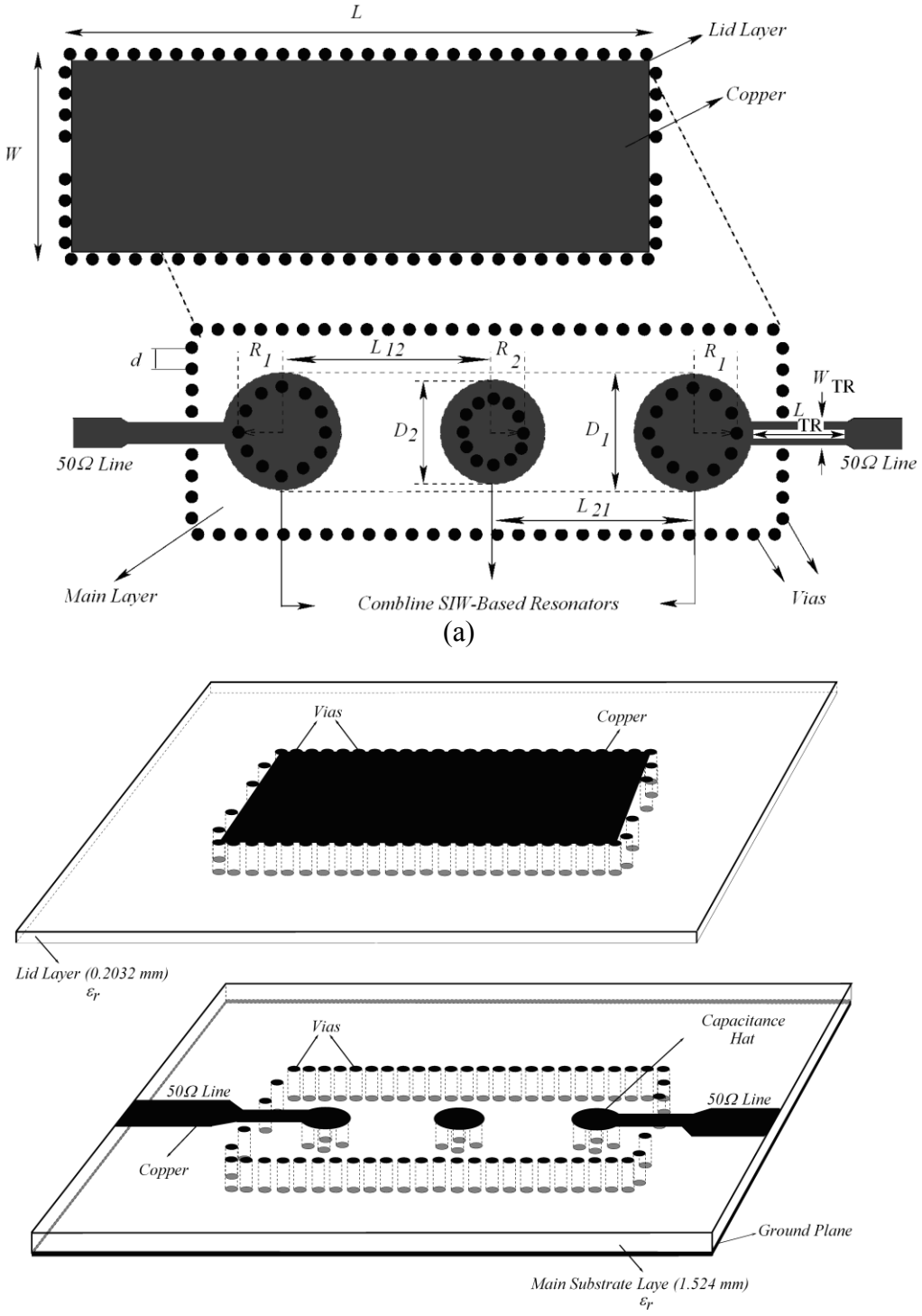

Figure 6-2: The proposed 3rd order evanescent-mode SIW bandpass filter: (a) 2D top view; (b) 3D side view.

Table 6.1 Dimension values of the 3rd order evanescent-mode SIW bandpass filter as depicted in Figure 6-2.

Symbol	Value (mm)
d	2
W	19.4
L_{TR}	7.9
W_{TR}	2.7
L	58
$L_{12}= L_{21}$	18.7
D_1	12.4
D_2	12.2
R_1	3.2
R_2	3.3
Via radius	0.35

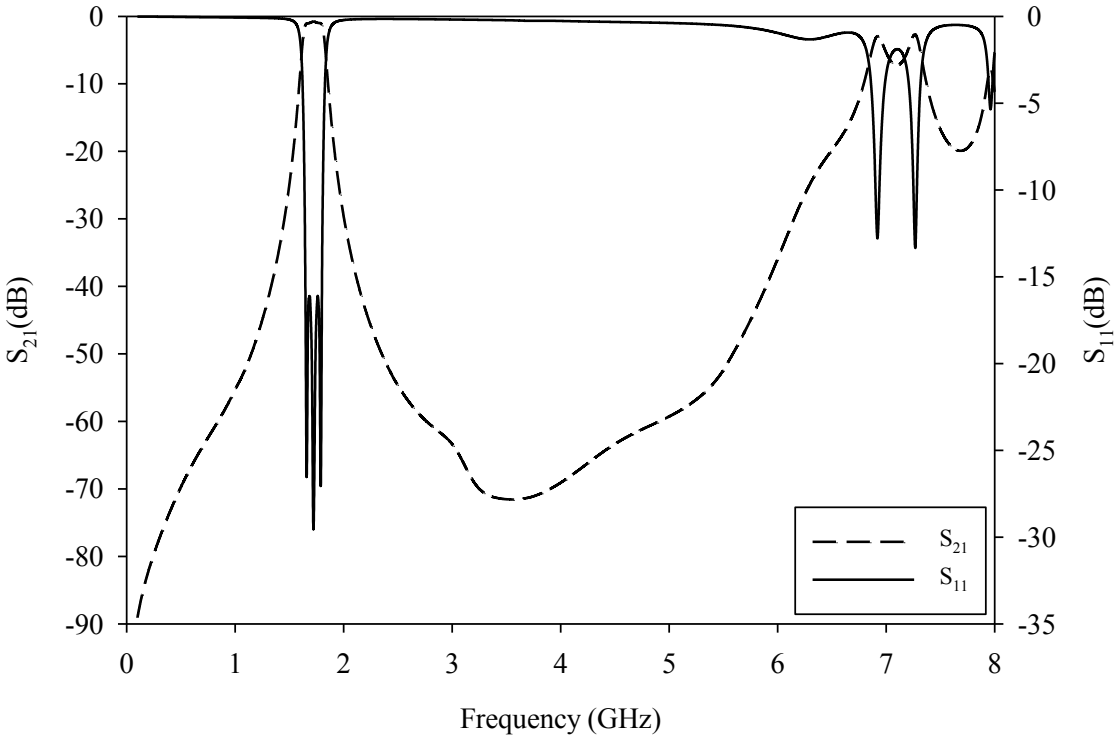

Figure 6-3: Simulated frequency response of a 3rd order evanescent-mode SIW bandpass filter.

The passband resonant frequency can be given by

$$\omega = \frac{1}{\sqrt{LC}} \tag{6.2}$$

where L represents the shunt inductor in Figure 6-1.

Figure 6-3 shows the simulated frequency characteristics of the 3rd order filter with a center frequency of 1.75 GHz and 8.7% fractional bandwidth. As illustrated, the frequency response shows an excellent stopband performance.

6.1.2 3rd Order Filter with N-1 Transmission Zeros

In order to improve a filter selectivity, finite frequency transmission zeros are required and must be located around the filter's passband edge. Here, the transmission zeros are generated by mixing the inter-resonator couplings (*i.e.* inductive/capacitive coupling) represented by the series inductors and capacitors between any two resonators (see Figure 6-4). Each mixed-coupling branch (*i.e.* (C_{12}, L_{12}) and (C_{21}, L_{21}) in Figure 6-4) is responsible for generating one transmission zero or a bandstop element. Here, the inductive coupling is due to the electric coupling between the adjacent Comblines while the capacitive coupling can be achieved by placing a lumped element capacitor as shown in Figure 6-4.

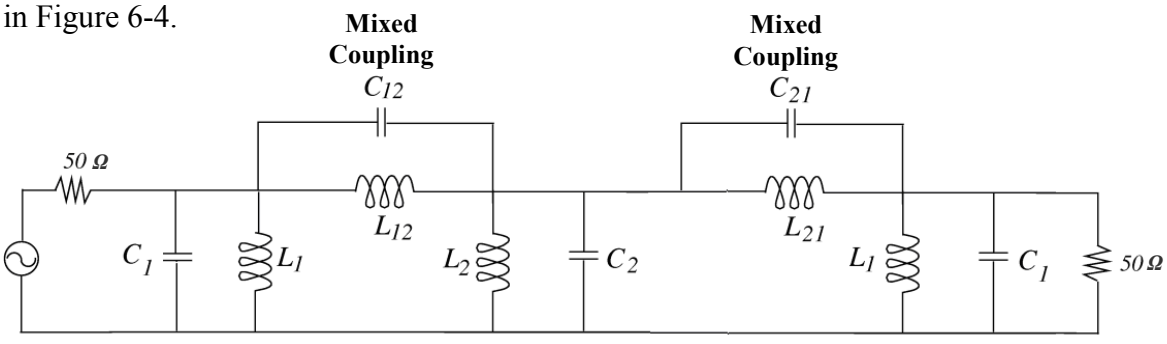

Figure 6-4: 3rd order circuit prototype realizing Two finite transmission zeros in a 50 Ω system.

The physical structure of the 3rd order evanescent-mode SIW filter (see Figure 6-5) with transmission zeros was simulated using *ANSYS HFSS* following the same guidelines presented in the previous SIW example leading to the following optimized dimensions presented in Table 6.2.

As depicted in Figure 6-5, lumped element capacitors are used to form the capacitive couplings needed to mix the couplings between the Comblines. Lumped element capacitors are usually preferred in testing since they can be easily replaced for filter tuning purposes. Another way to realize the series capacitors is by using inter-digital capacitors [88]. This type of distributed capacitor has higher Q in comparison with lumped element capacitors; however, no further adjustment can be made while testing. Tuning is a common process in microwave filters to accommodate fabrication tolerances.

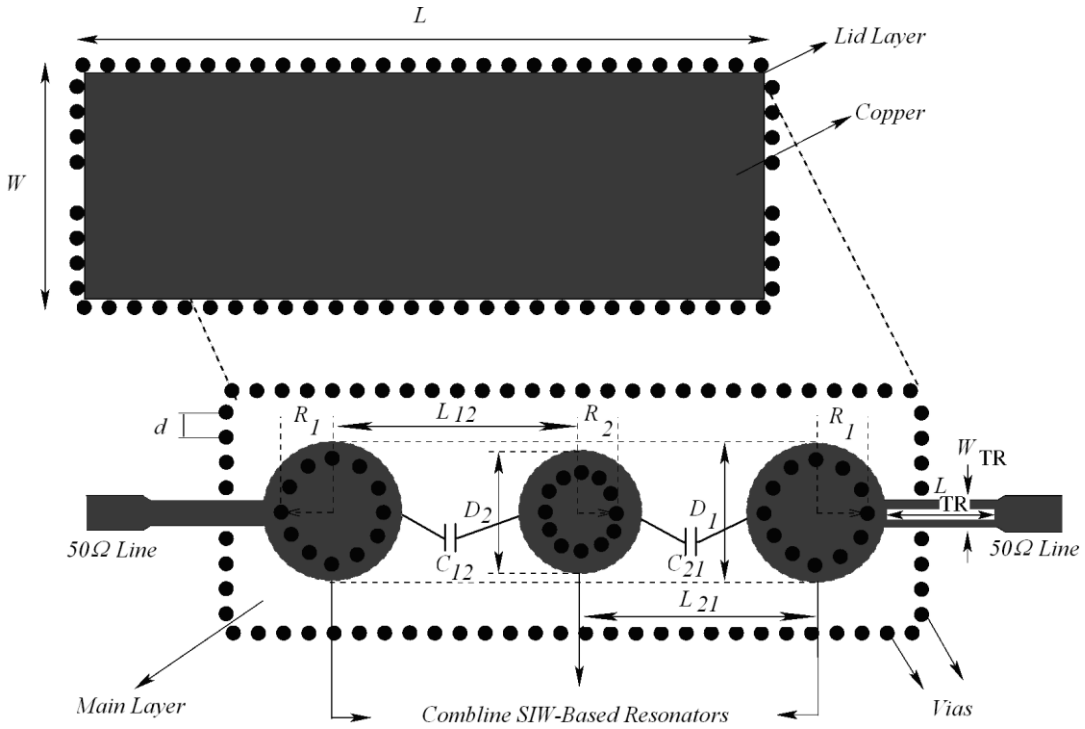

Figure 6-5: A 2D top view of the proposed 3rd order evanescent-mode SIW bandpass filter with two finite transmission zeros.

Table 6.2 Dimension values of the 3rd order evanescent-mode SIW bandpass filter with two transmission zeros as depicted in Figure 6-5.

Symbol	Value (mm)
d	2
W	19.8
L_{TR}	7.9
W_{TR}	2.7
L	58
L_{12}= L_{21}	19
C_{21}	2.2
C_{12}	1.4
D_1	11.8
D_2	11.6
R_1	3.0
R_2	3.7
Via radius	0.35

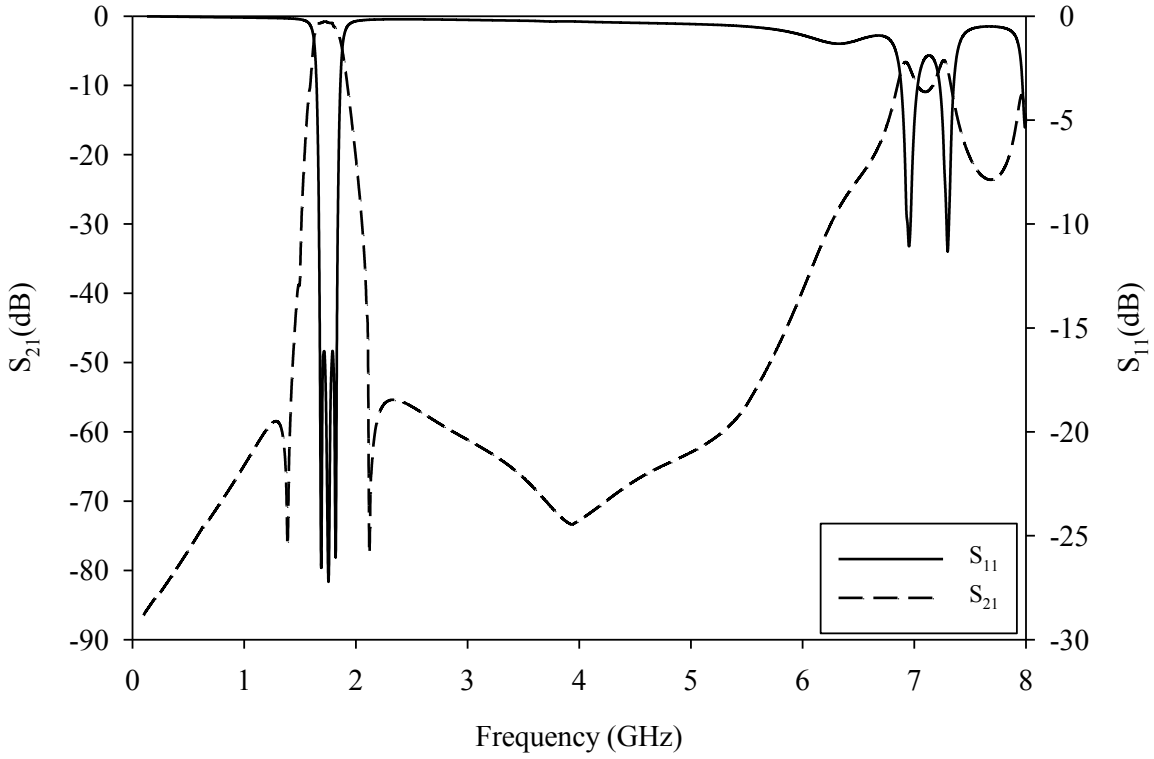

Figure 6-6: Simulated frequency response of a 3rd order evanescent-mode SIW bandpass filter with two transmission zeros.

Figure 6-6 shows the simulated frequency response of the 3rd order filter with a passband center frequency of 1.75 GHz and 8.7% fractional bandwidth. In addition, two transmission zeros are located at the passband's lower side at 1.38 GHz and at the passband's upper side at 2.12 GHz.

As illustrated, the frequency response shows an excellent stopband performance with high filter selectivity, and this is due to the placement of the transmission zeros.

6.2 Conclusions

In this chapter, a novel implementation approach based on SIW technology of evanescent-mode bandpass filters with and without transmission zeros has been presented. Both proposed filters exhibit wide stopband responses and excellent selectivity. In addition, the implemented filters are compact in size, especially at low operating frequencies, when compared with the conventional waveguide filters. A 3rd order SIW filter with symmetric transmission zeros was implemented for better filter selectivity as compared to the SIW filter without transmission zeros.

The proposed filters are promising and have potential applications in emerging RF frontends.

Chapter 7

Conclusions and Future Work

7.1 Summary of Research

In this dissertation, microwave front-ends with novel design concepts and implementation techniques have been introduced. The proposed front-end components were realized using planar technologies (*i.e.* SIW and Microstrips). Full-wave EM simulations were performed with the aide of *ANSYS HFSS* to prove the validity of the underlying design principles. Novel implementations of front-ends such as packaging, antennas, and filters in the microwave frequency range have been discussed.

In packaging, the problem of crosstalk reduction becomes one of the most important internal EMC problems especially in developing high-speed and high-density digital electronic equipment and very-large-scale integration (VLSI) applications. For this reason, both stepped impedance and open-circuited stub configurations employing uniform elements were developed for reduced far-end crosstalk in adjacent PCB traces. Such configurations are easier to implement in EMC prototype testing and have better crosstalk reduction compared to the conventional schemes. One drawback of using the stepped impedance design is the narrow width of the high impedance sections. This could be an issue for the flow of high current densities. The open-circuited stub design is more compact and more applicable for handling high current densities; however, the open-

circuited stub design has relatively higher radiated emissions when compared to the stepped impedance design. It is worth mentioning that the conventional techniques allow transmission over a wide range of frequencies and since the proposed traces act as a LPF, the frequency of operation is limited up to their cutoff frequencies.

In antennas, a novel and simple multilayered quad band-notched UWB antenna which covers all of WiMAX, INSAT, and lower/upper WLAN applications was designed, fabricated, and tested. Quad band-notched frequencies are realized by adding four ring resonators sharing the same vertical axis and implemented on multiple layers with possibility to arrange the ring resonators above and/or below the actual antenna radiator. This has lead to a robust and a straightforward fabrication. Moreover, since planar antennas have quantified Q-factor, designing multiple-band notched antenna is not an easy task. Q-factor of an antenna with rejection bands is responsible for generating a significant rejection band. In other words, as the number of rejection bands increases, the significance of the rejection bands decreases. For this reason ring resonators were utilized for generating the band notches in the proposed antenna. Ring resonator has low radiation losses and thus best utilization of the available Q-factor is achieved. Due to the low emission levels allowed by FCC, the proposed UWB antenna is beneficial for short-range and indoors applications. Such antenna will find potential military and industrial applications as in precision radar imaging technology, precision locating and tracking, and personal area networks.

Next, SIW dual-mode bandpass filters with excellent improvement in the upper stopband performance were implemented. The improvement in the upper stopband performance was achieved by cascading by a low-pass cleanup filter. The lowpass

cleanup filter is generated using DGS pattern within the SIW cavity area and hence, compact realization is maintained. Such filter has potential applications where light weight and compact size filter is desirable as in vehicular, airborne, and handheld wireless receivers.

As well, an SIW filter with dual-mode dual-band frequency characteristics and symmetric transmission zeros was successfully implemented. This work shows the capability of realizing dual-band response by moving one of the dual-mode bandpass filter transmission zeros toward its passband. Dual-band filters are essential component in wireless radio applications (*e.g.* GSM and GPS) which have dual co-operating bands for transmitting and receiving wireless signals.

Modern multi-band systems require multiple filters operating at different bands of frequencies. However, multiple filters occupy a large surface area, thus tunable filters; become an interesting solution to these problems. Therefore, an SIW bandpass filter with robust tuning ability was introduced. The filters can be reconfigured by adjusting a dc-magnetic bias applied to a pair of ferrite disks located at the edge of an SIW cavity. The applied magnetic field dramatically reduces the complexity compared to traditional electronic control methodologies.

Furthermore, there is always demand for narrowband filters with symmetrical transmission zeros placed close by the filter's passband as is the case with diplexers or multiplexers. Novel implementation approach of evanescent-mode SIW bandpass filters with and without transmission zeros was presented. The implemented filters are compact in size, especially at low operating frequencies and have wide stopband performance when compared with the conventional waveguide filters.

Finally, various parameters are defined and discussed when considering integration of different RF/microwave components within a system. The overall performance of a system can be evaluated by two important parameters, noise figure and power gain.

7.2 Future Work

Several research opportunities exist as a direct result of this work in designing high performance front-ends for passives. The following discussion shows the possible areas for future work

The proposed front-ends can be realized using high temperature superconductive (HTS) materials instead of copper. This will reduce the insertion losses and will provide more isolation at the rejection bands. The low surface resistance of superconducting materials allows the building of planar resonators with high unloaded quality factors.

Electromagnetic band-gap (EBG) structures principles can be applied on the proposed front-ends to reduce losses, especially at millimeter-wave and terahertz applications. Band-gap structures are dielectric materials with periodic arrangement that result in the formation of stop-bands at certain frequencies. Such structure helps in preventing traveling waves from scattering by external sources and consequently high-Q front-ends can be realized.

Several RF components require optimization, especially microwave filters. Different artificial intelligence techniques such as artificial neural networks (ANNs) algorithms and genetic algorithms (GAs) can be applied for optimizing. The selection of a specific algorithm is based on the output behavior of a device/component.

Periodic DGS with different shapes can be studied not only for enhancing the stopband isolation but also for high-Q and high performance structures.

Last but not least, investigating different active tuning elements (*i.e.* transistors or varactor diodes) in integrated tunable UWB antennas is highly desirable, especially for controlling the location of the frequency band-notches.

References

1. Levy R., Richard R. V., and Matthaei G., "Design of microwave filters," *IEEE Transactions on Microwave Theory & Techniques*, Vol. 50, No. 3, pp. 783-793, Mar. 2002.
2. Hunter I. C.*, Theory and Design of Microwave Filters, IEE,* 2001.
3. Matthaei G. L., "Comb-line bandpass filters of narrow or moderate bandwidth," *Microwave Journal*, pp. 82–91, Jan. 1963.
4. Hu K., Weng H., Beetner D., Pommerenke D., Drewniak J., Lavery K., and Whiles J., "Application of chip-level EMC in automotive product design," *IEEE EMC Int. Symp.*, Portland, OR, Aug. 2006, vol. 3, pp. 842-848.
5. Lee K., Lee H.-B., Jung H.-K., Sim J.-Y., and Park H.-J., "A serpentine guard trace to reduce the far-end crosstalk voltage and the crosstalk induced timing jitter of parallel microstrip lines," *IEEE Trans. Advanced Packaging,* vol. 31, no. 4, pp. 809-817, Nov. 2008.
6. Eged B., Mernyei F., Novak I., and Bajor P., "Reduction of far-end crosstalk on coupled microstrip PCB interconnects," *Proc. IEEE Instrumentation and Measurement Tech.,* Hamamatsu, Japan, May 1994, vol. 1, pp. 287-290.
7. Park S. W., Xiao F., Park D. C., and Kami Y., "Crosstalk analysis for two bent lines using circuit model," *IEICE Trans. Communications,* vol. E90, no. 2, pp. 323-330, Feb. 2007.

8. Huang W.-T., Lu C.-H., and Lin D.-B., "The optimal number and location of ground vias to reduce crosstalk," *PIER, Progress in Electromagnetics Research,* vol. 95, pp. 241-266, 2009.
9. Suntives A., Khajooeizadeh A., and Abhari R., "Using via fences for crosstalk reduction in PCB circuits," *IEEE EMC-S Int. Symp.*, Portland, OR, Aug. 2006, vol. 1, pp. 34-37.
10. Zhi L., Qiang W., and Changsheng S., "Application of guard traces with vias in the RF PCB layout," *Proc.* 3rd *Int. Symp. Electromagnetic Compatibility,* Beijing, China, May 21-24, 2002, pp. 771-774.
11. Cheng Y. S., Guo W. D., Shine G. H., Cheng H. H., and Wang C. C., "Fewest vias design for microstrip guard trace by using overlying dielectric," *IEEE Electrical Performance of Electronic Packaging*, San Jose, CA, Oct. 2008, pp. 321-324.
12. Brooks D., *Signal Integrity Issues and Printed Circuit Board Design*, Upper Saddle River, New Jersey: Prentice Hall, 2003.
13. Novak I., Eged B., and Hatvani L., "Measurement and simulation of crosstalk reduction by discrete discontinuities along coupled PCB traces," *IEEE Trans. on Instrumentation and Measurement,* vol. 43, no. 2, pp. 170-175, Apr. 1994.
14. Novak I., Eged B., and Hatvani L., "Measurement by vector network analyzer and simulation of crosstalk reduction on printed circuit board with additional center traces," *IEEE Institute of technology Conf.,* Irvine, CA, May 1993, pp. 269-274.
15. Djordjevic A. R., Sarkar T. K., and Harrington R. F., "Time-domain response of multiconductor transmission lines," *proc. IEEE*, vol. 75, pp. 743-764, June 1987.
16. Pozar D., *Microwave Engineering*, 3rd ed. New York: Wiley, 2005, pp. 412-416.

17. Almalkawi M., Khan Z., Devabhaktuni V., and Bunting C., "Far-end crosstalk reduction in adjacent PCB traces employing high/low-Z configurations," *IEEE EMC-S Int. Symp.*, Fort Lauderdale, FL, July 2010, pp. 760-763.
18. Matthaei G., Young L., and Jones E. M., *Microwave Filters Impedance-Matching Networks, and Coupling Structures*, Artech House, 1980s.
19. *ANSYS* high frequency structure simulator (*HFSS*), ver. 12.0, Ansys Inc., 2009.
20. MacCormick G., Khan Z., Devabhaktuni V., Alam M., and Wood A., "Estimated radiated emissions from printed circuit boards and cables inside EMC chambers," *IEEE EMC-S Int. Symp.*, Fort Lauderdale, FL, July 2010, pp. 36-39.
21. Federal Communications Commission, *Revision of Part 15 of the Commission's Rules Regarding Ultra-Wideband Transmission Systems*, First Report and Order, FCC 02.V48, April 2002.
22. Liu H.-W., Ku C.-H., Wang T.-S., and Yang C.-F., "Compact monopole antenna with band-notched characteristic for UWB applications," *IEEE Antennas Wireless Prop. Lett.,* vol. 9, pp. 397-400, 2010.
23. Ryu K. S. and Kishk A. A., "UWB antenna with single or dual band-notches for lower WLAN band and upper WLAN band," *IEEE Trans. Antennas Prop.*, vol. 57, no. 12, pp. 3942-3950, Dec. 2009.
24. Kim K. H. and Park S. O., "Analysis of the small band-rejected antenna with the parasitic strip for UWB," *IEEE Trans. Antennas Prop.*, vol. 54, no. 6, pp. 1688-1692, June 2006.

25. Wu S.-J., Kang C.-H., Chen K.-H., and Tarng J. H., "Study of an ultrawideband monopole antenna with a band-notched open-looped resonator," *IEEE Trans. Antennas Prop.*, vol. 58, no. 6, pp. 1890-1897, June 2010.
26. Lee W.-S., Lim W.-G., and Yu J.-W., "Multiple band-notched planar monopole antenna for multiband wireless systems," *IEEE Microw. Wireless and Comp. Lett.,* vol. 15, no. 9, pp. 576-578, Sept. 2005.
27. Chung K., Kim J., and Choi J., "Wideband microstrip-fed monopole antenna having frequency band-notch function," *IEEE Microw. Wireless and Comp. Lett.*, vol. 15, no. 11, pp. 766-768, Nov. 2005.
28. Zhou H.-J., Sun B.-H., Liu Q.-Z., and Deng J. Y., "Implementation and investigation of U-shaped aperture UWB antenna with dual band-notched characteristics," *Electron. Lett.*, vol. 44, pp. 1387-1388, Nov. 2008.
29. Li W. T., Shi X. W., and Hei Y. Q., "Novel planar UWB antenna with triple band-notched characteristics," *IEEE Antennas Wireless Prop. Lett.,* vol. 8, pp. 1094-1098, 2009.
30. Dong Y. D., Hong W., Kuai Z. Q., Yu C., Zhang Y., Zhou J. Y., and Chen J.-X., "Development of ultrawideband antenna with multiple band-notched characteristics using half mode substrate integrated waveguide cavity technology," *IEEE Trans. Antennas Prop.*, vol. 56, no. 9, pp. 2894-2902, Sept. 2008.
31. Liu H.-W., Ku C.-H., and Yang C.-F., "Novel CPW-fed planar monopole antenna for WiMAX/WLAN applications," *IEEE Antennas Wireless Prop. Lett.,* vol. 9, pp. 240-243, 2010.

32. Hsieh L.-H. and Chang K., "Equivalent lumped element G, L, C and unloaded Q's of closed- and open-loop ring resonators," *IEEE Trans. Microwave Theory Tech.*, vol. 50, no. 2, pp. 453-450, Feb. 2002.
33. Balanis C.A., *Antenna Theory and Analysis,* 2nd ed., Wiley, New York, 1997.
34. Garg R., Bhartia P., Bahl I., and Ittipiboon A., *Microstrip Antenna Design Handbook,* Artech House, Norwood, MA, 2001.
35. Rogers Corporation, http://www.rogerscorporation.com.
36. Willow Run Test Labs, http://www.wrtest.com.
37. Hughes Circuits, Inc., http://www.hughescircuits.com.
38. Snelling E. C., *Soft Ferrites: Properties and Applications*, Iliffe & Sons, Ltd., London, 1969.
39. Glimm J., Harms R., Munter K., Spitzer M., and Pape R., "A single-antenna method for traceable antenna gain measurement," *IEEE Trans. on Electromagnetic Compatibility*, vol. 41, no. 4, pp. 436-439, Nov. 1999.
40. Deslandes D. and Wu K., "Integrated microstrip and rectangular waveguide in planar form," *IEEE Microw. Wireless Compon. Lett.,* vol. 11, no. 2, pp. 68-70, Feb. 2001.
41. Hao Z. C., Hong W., Chen X. P., Chen J. X., Wu K., and Cui T. J., "Multilayered substrate integrated waveguide (MSIW) elliptic filter," *IEEE Microwave Wireless Compon. Lett.,* vol. 15, no. 2, pp. 95-97, Feb. 2005.
42. Chen X. P., Wu K., and Li Z. L., "Dual-band and triple-band substrate integrated waveguide filters with chebyshev and quasi-elliptic responses," *IEEE Trans. Microwave Theory Tech.,* vol. 55, no. 12, pp. 2569-2578, Dec. 2007.

43. Atia A. E. and Williams A. E., "New types of bandpass filters for satellite transponders," *COMSAT Tech. Rev.*, vol. 1, no. 1, pp. 21-43, 1971.

44. Atia A. E., Williams A. E., and Newcomb R., "Narrow-band multiple-coupled cavity synthesis," *IEEE Trans. Circuits Syst.*, vol. 21, no. 5, pp. 649-655, Sept. 1974.

45. Atia A. E. and Williams A. E., "Narrow-bandpass waveguide filters," *IEEE Trans. Microwave theory Tech.*, vol. 20, no. 4, pp. 258-265, Apr. 1972.

46. Hong J. S. and Lancaster M. J., "Bandpass characteristics of new dual-mode microstrip square loop resonators," *IEE Electron lett.* vol. 31, pp. 891-892, May 1995.

47. Chen X., Hong W., Cui T., and Wu K., "Substrate integrated waveguide (SIW) asymmetric dual-mode filter and diplexer," *Int. Journal of Electronics*, vol. 92, no. 12, pp. 743-753, Dec. 2005.

48. Wei Q. F., Li Z. F., and Shen H. G., "Dual-mode filters based on substrate integrated waveguide by multilayer LTCC technology," *Microwave and Optical Technology Lett*., vol. 50, no. 11, pp. 2788-2790, Nov. 2008.

49. Chang C.-Y., and Hsu W.-C., "Novel planar, square shaped, dielectric-waveguide, single-, and dual-mode filters," *IEEE Trans. Microwave Theory Tech.*, vol. 50, no. 11, pp. 2527-2536, Nov. 2002.

50. Yun T. S., Nam H., Kim J. Y., Lee B., Choi J. J., Kim K. B., Ha T. J., and Lee J. C., "Harmonics suppressed substrate-integrated waveguide filter with integration of low-pass filter," *Microwave and Optical Technology Lett.*, vol. 50, no. 2, pp. 447-450, Feb. 2008.

51. Chen H. J., Huang T. H., Chang C. S., Chen L. S., Horng J. H., Wang Y. H., and Houng M. P., "A compact bandpass filter with enhanced stopband characteristics by an asymmetric cross-shaped defected ground structure," *IEEE Trans. On Ultrasinics, Ferroelectrics, and Frequency Control*, vol. 53, no. 11, pp. 2183-2187, Nov. 2006.
52. Zhang Y. L., Hong W., Wu K., Chen J. X., and Tang H. J., "Novel substrate integrated waveguide cavity filter with defected ground structure," *IEEE Trans. Microwave Theory Tech.*, vol. 53, no. 4, pp. 1280-1287, April 2005.
53. Ahn D., Park J. S., Kim C. S., Qian Y., and Itoh T., "A design of the low-pass filter using the novel microstrip defected ground structure," *IEEE Trans. Microwave Theory Tech.*, vol. 49, no. 1, pp. 86-93, Jan. 2001.
54. Lee J. K. and Kim Y. S., "Ultra-wideband bandpass filter with improved upper stopband performance using defected ground structure," *IEEE Microwave and Wireless Component Lett.*, vol. 20, no. 6, pp. 316-318, June 2010.
55. J. S. Hong and M. J. Lancaster, *Microstrip Filters for RF/Microwave Applications,* Wiley-Interscience 2001.
56. Diaz E., Esteban H., Belenguer A., Boria V., Morro J., and Cascon J., "Efficient design of substrate integrated waveguide filters using a hybrid MoM/MM analysis method and efficient rectangular waveguide design tools," *IEEE International Conference on Electromagnetics in Advanced Applications*, 2011.
57. Guglielmi M., Jarry P., Kerherve E., Roquebrun O., and Schmitt D., "A new family of all-inductive dual-mode filters," *IEEE Trans. Microwave Theory Tech.*, vol. 49, no. 10, pp. 1764-1769, Oct. 2001.

58. Chen X. P., Wu K., and Drolet D., "Substrate integrated waveguide filter with improved stopband performance for satellite ground terminal," *IEEE Trans. Microwave Theory Tech.*, vol. 57, no. 3, pp. 674-683, March 2009.

59. Deslandes D. and Wu K., "Accurate modeling, wave mechanism, and design consideration of a substrate integrated waveguide," *IEEE Trans. Microwave Theory Tech.,* vol. 54, no. 6, pp. 2516-2526, June 2006.

60. Bozzi M., Perregrini L., and Wu K., "Modeling of conductor, dielectric, and radiation losses in substrate integrated waveguide by the boundary integral-resonant mode expansion method," *IEEE Trans. Microwave Theory Tech.*, vol. 56, no. 12, pp. 3153-3161, Dec. 2008.

61. Joshi H., Sigmarsson H. H., Moon S., Peroulis D., and Chappell W., "High-Q fully reconfigurable tunable bandpass filters," *IEEE Trans. Microwave Theory Tech.*, vol. 57, pp. 3525-3533, Dec. 2009.

62. Bohorquez J. C., Potelon B., Person C., Rius E., Quendo C., Tanne G., and Fourn E., "Reconfigurable planar SIW cavity resonator and filter," *Digest of Microwave Symposium, IEEE MTT-S International*, San Francisco, CA, pp. 947-950, June 2006.

63. Krupka J., Abramowicz A., and Derzakowski K., "Magnetically tunable filters for cellular communication terminals," *IEEE Trans. Microwave Theory Tech.*, vol. 54, pp. 2329-2335, June 2006.

64. Shen T., Zaki K. A., Wang C., and Deriso J., "Tunable dielectric resonators with dielectric tuning disks in cylindrical enclosures," *IEEE MTT-S Int. Symp. Dig.,* Boston, MA, pp. 1441-1444, June 2000.

65. Uher J., Bornemann J., and Arndt F., "Magnetically tunable rectangular E-plane integrated circuit filters," *IEEE Trans. Microwave Theory Tech.*, vol. 36, pp. 1014-1022, June 1988.

66. Miranda F. A., Subramanyam G., Keuls F. W. V., Romanofsky R. R., Warner D., and Mueller C. H., "Design and development of ferroelectric tunable microwave components for Ku- and K-band satellite communication systems," *IEEE Trans. Microwave Theory Tech.*, vol. 48, pp. 1181-1189, July 2000.

67. Lucyszyn S. and Robertson, "Synthesis techniques for high performance octave bandwidth 180o analog phase shifters," *IEEE Trans. Microwave Theory Tech.*, vol. 40, pp. 731-740, Apr. 1992.

68. Lee S.-S., Udupa A. H., Erlig H., Zhang H., Chang Y., Chang D. H., Bhttacharya D., Tsap B., Steier W. H., Dalton L. R., and Fetterman H. R., "Demonstration of a photonically controlled RF phase shifter," *IEEE Microwave Guided Wave Lett*., vol. 9, pp. 357-359, Sept. 1999.

69. D'Orazio W., Wu K., and Helszajn J., "A substrate integrated waveguide degree-2 circulator," *IEEE Microwave Wireless Compon. Lett.*, vol. 14, pp. 207-209, May 2004.

70. D'Orazio W. and Wu K., "Substrate-integrated-waveguide circulators suitable for millimeter-wave integration," *IEEE Trans. Microwave Theory Tech.*, vol. 54, pp. 3675-3680, Oct. 2006.

71. Razavipour H., Safian R., Askari G., Fesharaki F., and Sadeghi H. M., "A new dual-band high power ferrite circulator," *Progress in Electromagnetics Research C*, vol. 10, pp. 15-24, 2009.

72. How H., Vittoria C., and Carosella C., "Novel filter design incorporating asymmetrical stripline Y-junction circulators," *IEEE Trans. Microwave Theory Tech.*, vol. 39, pp. 40-46, Jan. 1991.

73. Helszajn J. and Sharp J., "Verification of first circulation conditions of turnstile waveguide circulators using a finite-element solver," *IEEE Trans. Microwave Theory Tech.*, vol. 53, pp. 2309-2316, July 2005.

74. Tsankov M. A. and Milenova L. G., "Accurate design of partial-height ferrite resonators for waveguide circulators," *Journal of Magnetism and Magnetic Materials*, vol. 83, pp. 435-436, 1990.

75. Trans-Tech Inc., Ceramic and Advanced Materials, http://www.trans-techinc.com.

76. Linkhart D. K., *Microwave Circulator Design*, Artech House, Massachusetts, 1989.

77. Jaynes E. T., "Ghost modes in imperfect waveguides," *Proc. IRE,* vol. 46, pp. 416-418, Feb. 1958.

78. Edson W. **A.**, "Microwave filters using ghost-mode resonance, in *Proc. IRE Electron. Components Conf.,* vol. 19, pp. 2, 1961.

79. Synder R., "New application of evanescent mode waveguide to filters design," *IEEE Trans. Microwave Theory Tech.,* vol. 25, pp. 1013-1021, Dec. 1977.

80. Chang H.-C. and Zaki K. A., "Evanescent-mode coupling of dual-mode rectangular waveguide filters," *IEEE Trans. Microwave Theory Tech.*, vol. 39, no. 8, pp. 1307-1312, Aug. 1991.

81. Kirilenko A., Rud L., Trachenko V., and Kulik D., "Evanescent-mode ridged waveguide bandpass filters with improved performance," *IEEE Trans. Microwave Theory Tech.*, vol. 50, no. 5, pp. 1324-1327, May 2002.

82. Snyder R. V., "stepped-ferrite tunable evanescent filters," *IEEE Trans. Microwave Theory Tech.*, vol. 29, no. 4, pp. 364-371, April 1981.

83. Gong X., Margomenos A., Liu B., Hajela S., Katehi P. B., and Chappell W. J., "Precision fabrication techniques and analysis on high-Q evanescent-mode resonators and filters of different geometries," *IEEE Trans. Microwave Theory Tech.*, vol. 52, no. 11, pp. 2557-2566, Nov. 2004.

84. Skedd R. F. and Craven G. F., "New type of magnetically tunable multisection bandpass filter in ferrite-loaded evanescent waveguide," *IEEE Trans.Magnetics*, vol. 3, no. 3, pp. 396-401, Sept. 1967.

85. Snyder R. V., Niver E., Um K., and Shin S., "Suspended resonators for filters-reduced λg excitation of evanescent cavities using high dielectric constant feedlines," *IEEE Trans. Microwave Theory Tech.*, vol. 50, no. 12, pp. 2890-2895, Dec. 2002.

86. Levy R., Yao H. W., and Zaki K. A., "Transitional combline/evanescent mode microwave filters," *IEEE Trans. Microwave Theory Tech.*, vol. 45, pp. 2094–2099, Dec. 1997.

87. Yao H. W., Wang C., and Zaki K. A., "Quarter wavelength ceramic combline filters," *IEEE Trans. Microwave Theory Tech.*, vol. 44, pp. 2673–2679, Dec. 1996.

88. Zhu L. and Wu K., "Accurate circuit model of interdigital capacitor and its application to design of new quasi-lumped miniaturized filters with suppression of harmonic resonance," *IEEE Trans. Microwave Theory Tech.*, vol. 48, no. 3, pp. 347–356, Mar. 2000.